Schlüsseltechnologien / Key Technologies
Band / Volume 163
ISBN 978-3-95806-300-6

JÜLICH
Forschungszentrum

Mitglied der Helmholtz-Gemeinschaft

Schlüsseltechnologien
Key Technologies

Epitaxy of Si-Ge-Sn for heterostructure emitters

163

Nils von den Driesch

JÜLICH
Forschungszentrum

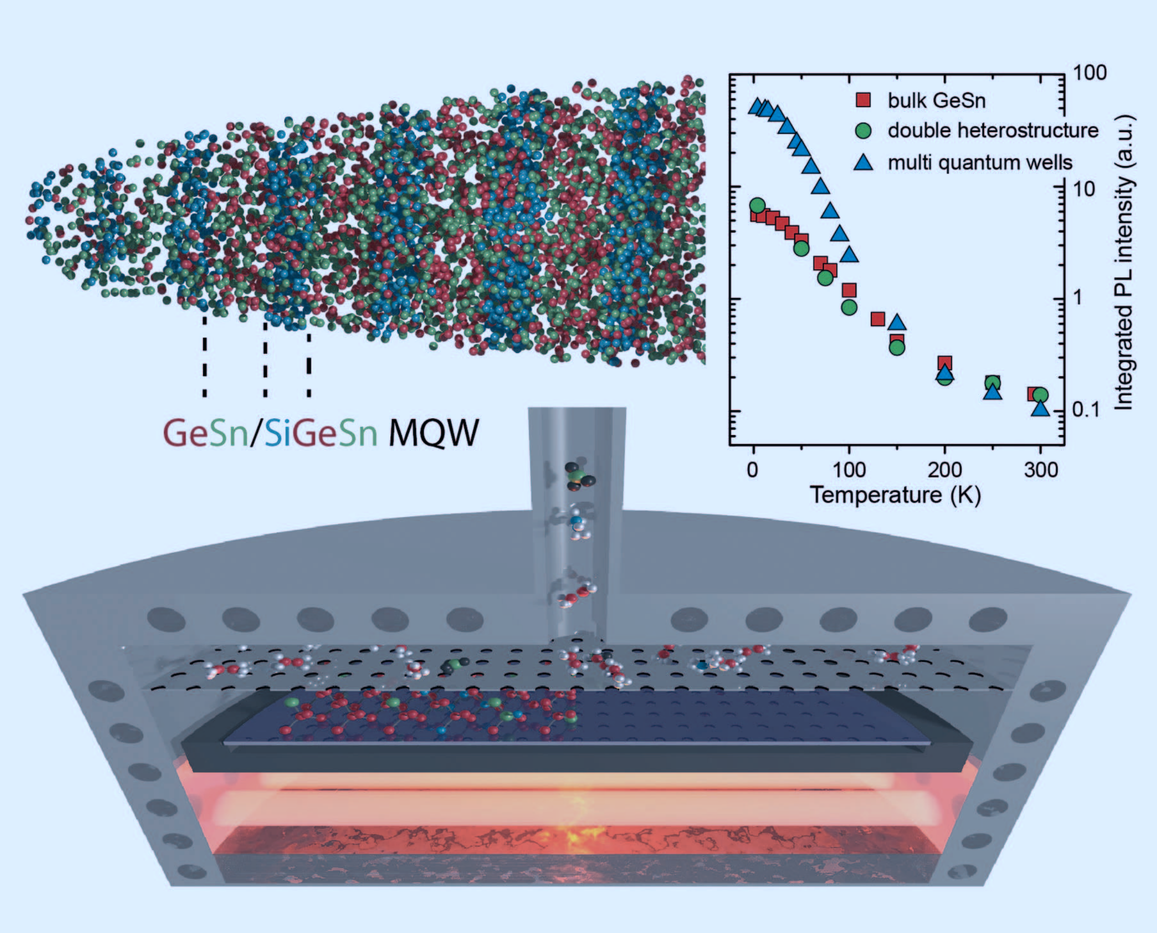

Epitaxy of group IV Si-Ge-Sn alloys for advanced heterostructure light emitters

Nils von den Driesch

Schlüsseltechnologien / Key Technologies
Band / Volume 163
ISBN 978-3-95806-300-6

Mitglied der Helmholtz-Gemeinschaft

JÜLICH
Forschungszentrum

Schriften des Forschungszentrums Jülich
Reihe Schlüsseltechnologien / Key Technologies Band / Volume 163

Forschungszentrum Jülich GmbH
Peter Grünberg Institut
Halbleiter-Nanoelektronik (PGI-9)

Epitaxy of group IV Si-Ge-Sn alloys for advanced heterostructure light emitters

Nils von den Driesch

Schriften des Forschungszentrums Jülich
Reihe Schlüsseltechnologien / Key Technologies Band / Volume 163

ISSN 1866-1807 ISBN 978-3-95806-300-6

Bibliografische Information der Deutschen Nationalbibliothek.
Die Deutsche Nationalbibliothek verzeichnet diese Publikation in der
Deutschen Nationalbibliografie; detaillierte Bibliografische Daten
sind im Internet über http://dnb.d-nb.de abrufbar.

Herausgeber und Vertrieb: Forschungszentrum Jülich GmbH
Zentralbibliothek, Verlag
52425 Jülich
Tel.: +49 2461 61-5368
Fax: +49 2461 61-6103
zb-publikation@fz-juelich.de
www.fz-juelich.de/zb

Umschlaggestaltung: Grafische Medien, Forschungszentrum Jülich GmbH

Druck: Grafische Medien, Forschungszentrum Jülich GmbH

Schriften des Forschungszentrums Jülich
Reihe Schlüsseltechnologien / Key Technologies, Band / Volume 163

D 82 (Diss., RWTH Aachen University, 2018)

ISSN 1866-1807
ISBN 978-3-95806-300-6

Abstract

Over the last decades, silicon-based integrated circuits underpinned information technology. To keep up with the demand for faster and, becoming increasingly more relevant nowadays, energy-efficient electronics, smart solutions targeting power consumption are required. Integration of photonic components, e.g. for replacing part of copper interconnects, could strongly reduce on-chip dissipation. Prerequisite for efficient active optoelectronic devices, however not available in group IV elements, is a direct bandgap. Only recently though, a truly silicon-compatible solution was demonstrated by tin-based group IV GeSn alloys, which offer a direct bandgap for a cubic lattice and Sn concentrations above 9 at.%. Nevertheless, when moving from an experimental direct bandgap demonstration towards readily integrated light emitters, plenty of challenges have to be overcome. In this work, some of the remaining key aspects are investigated.

Reduced-pressure chemical vapor deposition on 200 mm (Ge-buffered) Si wafers was used to form the investigated Si-Ge-Sn alloys. GeSn layers with subtitutionally incorporated Sn concentrations up to 14 at.%, considerably exceeding the solid solubility limit of 1 at.% Sn in Ge, were epitaxially grown to study growth kinetics. The necessary strain relieve in GeSn binaries was studied growing layers with thicknesses up to 1 µm, well above the critical thickness for strain relaxation. Influence of both, Sn incorporation and residual strain, on the optical properties was probed using temperature-dependent photoluminescence and reflection spectroscopy. Mid infrared light emission was found at wavelengths as long as 3.4 µm (0.37 eV) at room temperature. Overall, the investigated GeSn material system allows to cover a range up to about 2 µm (0.60 eV), making these binaries also interesting for a multitude of chemical and biological sensing applications.

Efficient light sources further require the confinement of carriers in heterostructures. Therefore, also epitaxy of SiGeSn ternaries, which previously have been identified as optimal larger bandgap claddings, was scrutinized. The additional degree of compositional freedom was demonstrated by bandgap engineering, individually using strain relaxation, Si and Sn composition.

Combining GeSn binaries and SiGeSn ternaries allowed formation of different diode structures. Light emitting diodes, both from GeSn homojunctions and multi quantum well heterojunctions, were epitaxially grown and studied for their emission characteristics. One drawback in these structures, however, is that they do not just yet feature a direct bandgap.

Finally, several (so far undoped) direct bandgap GeSn/SiGeSn double heterostructures and multi quantum wells were investigated. The importance of defect engineering, that is separation of unavoidable misfit defects and active device regions, is stressed and fathomed for both designs. Excellent structural properties of the grown layers were proven by advanced characterization techniques, such as atom probe tomography or dark-field electron holography. Photoluminescence measurements were carried out to probe the optical quality of those structures, revealing strongly enhanced light emission from MQW structures, compared to bulk GeSn layers.

Zusammenfassung

Seit mehreren Jahrzehnten bilden Silizium-basierte (Si) integrierte Schaltkreise die Grundlage der modernen Informationstechnologie. Die allerdings weiterhin ungebrochene Nachfrage nach immer schnellerer und, mittlerweile ebenfalls, energieeffizienter Elektronik verlangt nach neuen Lösungen im Hinblick auf eine geringe Leistungsaufnahme. Die Integration photonischer Bauelemente, beispielsweise um Teile der elektrischen Verbindungen aus Kupfer zu ersetzen, kann die Dissipation auf dem Computerchip stark verringern. Die grundlegende Voraussetzung für aktive optoelektronische Bauelemente, welche allerdings in den Elementen der vierten Hauptgruppe nicht vorhanden ist, ist eine direkte Bandlücke. Kürzlich jedoch ist mit Zinn-basierten Gruppe IV-Verbindungen – genauer Germanium-Zinn-Legierungen (GeSn) – eine vollständig Si-kompatible Lösung präsentiert worden. Es konnte gezeigt werden, dass kubisches GeSn mit Zinn-Konzentrationen oberhalb von etwa 9 at.% eine direkte Bandlücke besitzt. Die Demonstration einer direkten Bandlücke kann allerdings nur ein allererster Schritt auf dem Weg zu vollständig integrierten licht-emittierenden Bauelementen sein. Im Rahmen dieser Arbeit sollen einige der verbleibenden Hürden und Aspekte untersucht werden.

Die untersuchten Si-Ge-Sn Legierungen wurden mithilfe chemischer Gasphasenabscheidung bei reduzierten Druck hergestellt, wobei 200 mm Si-Wafer (teilweise mit Ge-Pufferschichten) als Substrate verwendet wurden. GeSn-Schichten mit substitutionell eingebauter Sn-Konzentration von bis zu 14 at.% – ein einphasiges Gemisch von Ge und Sn ist bis maximal 1 at.% Zinn thermodynamisch stabil – wurden epitaktisch gewachsen um die Wachstumskinetik näher zu beleuchten. Der notwendige Abbau der internen Verspannung des Materials konnte untersucht werden, indem bis zu 1 µm dicke Schichten hergestellt wurden, was deutlich oberhalb der kritischen Dicke für plastische Spannungsrelaxation liegt. Der Einfluss von Zinn-Konzentration und Verspannung des Materials auf die optischen Eigenschaf-

ten wurde mithilfe von temperaturabhängiger Photolumineszenz- und Absorptionsspektroskopie erforscht. Lichtemission im mittleren Infrarotbereich von bis zu 3.4 µm (0.37 eV) konnte bei Raumtemperatur beobachtet werden. Insgesamt erlaubt das untersuchte GeSn-Materialsystem einen breiten Infrarot-Bereich bis etwa 2 µm (0.6 eV) abzudecken, was es auch für eine Vielzahl chemischer oder biologischer Sensoren attraktiv macht.

Eine weitere wichtige Methode in der Herstellung effizienter Halbleiterlichtquellen ist es, die Ladungsträger mit Hilfe von Heterostrukturen in der aktiven Schicht einzuschließen. Aus diesem Grund wurde ebenfalls das Wachstum des ternären Silizium-Germanium-Zinn-Systems (SiGeSn) untersucht, welches aufgrund seiner größeren Bandlücke bereits in früheren Arbeiten als ideales System für die äußeren Schichten der Heterostruktur identifiziert wurde. Der zusätzliche sich ergebende kompositionelle Freiheitsgrad wurde genutzt, um eine Abstimmbarkeit der Bandlücke zu demonstrieren, individuell für Si-Gehalt, Sn-Gehalt, sowie die Verspannung des Materials.

Das Kombinieren von binären GeSn- und ternären SiGeSn-Schichten ermöglicht die Demonstration verschiedener Dioden. Verschiedene Typen von Leuchtdioden, einerseits aus GeSn-Homostrukturen, andererseits auch aus Mehrfach-Quantentopf-Heterostrukturen (MQW-Strukturen) bestehend, wurden epitaktisch gewachsen, bevor ihre Emissionseigenschaften untersucht wurden. Ein Nachteil der untersuchten LEDs ist allerdings, dass keine von denen eine klar direkte Bandlücke aufweist.

Schlussendlich wurden mehrere (jedoch undotierte) GeSn/SiGeSn Doppel-Heterostrukturen und MQW-Strukturen untersucht, welche allesamt eine direkte Bandlücke besitzen. Die essentielle Bedeutung von Kristalldefekten, bzw. deren Separation von der aktiven Schicht, ist in beiden Strukturen untersucht und herausgestellt worden. Die exzellenten strukturellen Eigenschaften der gewachsenen Schichten konnten mit komplexen Charakterisierungsmethoden, wie der Atomsonden Tomographie oder Elektronenholographie, gezeigt werden. Photolumineszenzmessungen, welche durchgeführt wurden um die optische Güte der Schichten zu bewerten, zeigten eine deutlich verstärkte Emission der MQW-Strukturen, verglichen mit einfachen GeSn-Schichten.

Contents

1 Introduction

Green information technology (Green IT) targets sustainability in the information and communication sector. An obvious goal is making integrated circuits (IC) more energy efficient. Merging state-of-the-art silicon *complementary metal-oxide-semiconductor* (Si-CMOS) technology on-chip with photonic components may one day yield monolithically *opto-electronic integrated circuits* (OEIC) that allow strongly reduced power consumption.[1] Replacing part of copper interconnects in ICs with optical ones, for example, may radically increase the available bandwidth and solve the interconnect bottleneck, already today limiting IC performance.[2,3] Bandwidth limitations will become an even more pressing issue in future, when the number of interconnected devices will strongly increase from the so-called *Internet of things* (IoT). For classification, the global internet traffic in 2021 will exceed the gigabyte equivalent of all movies ever made *every single minute*.[4]

Also regarding *deep learning* of *artificial neural networks*, huge amounts of data are required to optimize systems for object or speech recognition.[5] The necessary bandwidth can likely be provided by means of optical interconnects.

The fabrication of group IV-based OEICs yielded several key devices so far, however only passive components such as photodetectors[6,7] or electro-optical modulators.[8,9] Even the formation of complex group IV OEICs, such as optical interconnects,[10] has been demonstrated on a single chip, using hundreds of photonic components and 70 millions transistors.[11] Nevertheless, nowadays all OEICs need to rely on an external light source, which light is coupled into the chip, since the creation of a solely group IV light source remained an elusive goal for long time. The reason lies within the inability of bulk Si and Ge to efficiently generate light, originated in their indirect bandgap. In this regard, direct bandgap group IV alloys have the potential to revolutionize integrated circuits. Alternative approaches would be the heterointegration of externally fabricated III-V lasers,[12] or III-V lasers grown directly on Si substrates.[13–15] However, the latter procedures suffer from the chemical incompatibility and thermal mismatch of the different involved material classes.

Possible solutions within group IV materials facilitate tensile strained germanium (Ge), for example in microbridge geometries,[16,17] yet no optical gain, prerequisite for lasing, has been shown so far. A viable solution, gaining lots of attention recently, focusses on alloying Ge with tin (Sn). Optical gain,[18] as well as optically pumped lasing was demonstrated in several geometries within this pure group IV material system.[18–21]

Direct bandgap GeSn-based alloys may also be an interesting alternative regarding several different branches of future electronics. The considerably decreased effective mass of Γ carriers will strongly boost carrier mobility, once a considerable number of electrons occupy that valley.[22] This prospect makes it an ideal channel material in future *metal-oxide-semiconductor field-effect transistors* (MOSFETs), as it can avail the mature Si platform technology. Also strongly increased band-to-band tunneling (BTBT) rates, originating in the fundamental direct bandgap, may further help leveraging group IV tunneling-FETs.[23] Nowadays those are highly relevant, as an increasing desire for portable or IoT devices demands a large number of ultra-low power electronics.[24]

The proved direct bandgap in GeSn, which is located in the short-wave to mid infrared range between 2.5–3.5 µm (0.5–0.35 eV), depending on the exact stoichiometry, enables a multitude of other interdisciplinary applications such as chemical/biological sensors,[25,26] communication in a new 2 µm wavelength band[27] or night-vision imaging.[28]

Despite its manifold prospects, the Sn-based group IV system is still in an early stage of development. After previous works focussed on basic physical properties, such as the unambiguous direct bandgap proof,[29] the current thesis aims at the physics behind epitaxial growth of GeSn binaries and SiGeSn ternaries for building complex heterostructures for a variety of applications.

Following this brief introduction, a general overview of the benefits and growth challenges in the Si-Ge-Sn material system is given in **chapter 2**. The results of epitaxial growth investigations of GeSn binaries are presented in **chapter 3**. In there, GeSn layers grown on Si or Ge-buffered wafers are examined to probe the influence of different parameters, such as temperature and precursor gases, on growth kinetics. Strain relaxation in thick layers is monitored, carefully eyeing evolution of defects. The binaries' adequacy for different types of optical applications is discussed. In the following **chapter 4**, epitaxy of SiGeSn ternaries is investigated. As will be shown, the enhanced parameter set of Si and Sn composition makes ternaries very versatile, allowing sophisticated band engineering for different applications. The gained insights will be adapted in **chapter 5**, where epitaxial growth of several light emitting diode (LED) structures is discussed. Besides plain homojunction structures, different types of multi quantum well (MQW) LEDs are demonstrated. In the end, binaries and ternaries are combined to form efficient group IV direct bandgap heterostructures, which are suitable for diverse optical applications. Finally, a brief summary of the obtained results, as well as an outlook on possible future developments in the Si-Ge-Sn field is given in **chapter 6**.

2 Si-Ge-Sn material system

Contents

Before the main results are discussed in the upcoming chapters, this chapter provides a brief overview on the physical and technological background of Sn-based epitaxy. Upon its first mentioning in 1982, GeSn binaries were thought to have promising material properties, offering a small bandgap and higher carrier mobilities than III-V materials, due to the absence of polar scattering.[30] Due to severe technological challenges, however, it took more than thirty years from the first microcrystalline binaries[31] until the direct bandgap proof via demonstration of optically pumped lasing.[18] These challenges, as well as techniques for their overcoming, are discussed in this chapter following an introduction on the particular electronic properties of Sn-based group IV alloys.

2.1 Band structure considerations

The key of the promising electronic properties of Si-Ge-Sn materials lies within alloying a semiconductor (silicon or germanium) with the semimetal tin (Sn). From the several phases of Sn, which are stable in different pressure and temperature

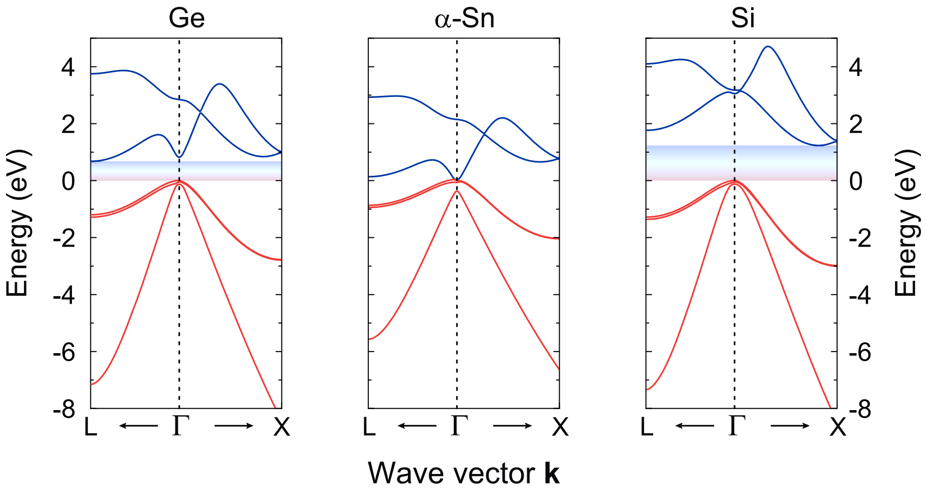

Figure 2.1 – Band structures of elemental a) Germanium, b) α-Sn and c) Silicon. Data adapted with permission from reference [32]. ©IOP Publishing. All rights reserved.

ranges, α-Sn is most interesting for this purpose. It exists in a cubic diamond lattice, as the other group IV elements silicon (Si) and germanium (Ge), and is stable for temperatures below 13.1 °C.[33] The main difference in their electronic properties can be seen from the elemental band structures of Ge, α-Sn and Si, which are illustrated in **Figure 2.1**a-c at the center of the Brillouin zone (Γ point), as well as around the high symmetry points L and X. All three elements have their valence band top located at Γ, but their conduction bands show minima at different points in reciprocal space.

An overview on the most important band structure parameters can be found in Table 2.1. Germanium, as can be seen from Figure 2.1a, features a narrow, indirect bandgap of 0.76 eV (for 0 K) at L. Silicon, on the other hand, has its smallest bandgap of 1.17 eV at 0 K at the X valley, which also makes it an indirect semiconductor. The exceptionality of α-Sn lies within its negative bandgap at Γ, as proposed already early in the 1960s,[34] which actually makes it a semimetal similar to graphene[35] or bismuth.[36] Since the difference of Ge and Sn bandgaps is larger at Γ than at the L point ($\Delta E_\Gamma = E_{\Gamma,\mathrm{Ge}} - E_{\Gamma,\mathrm{Sn}} > \Delta E_L = E_{L,\mathrm{Ge}} - E_{L,\mathrm{Sn}}$), the

Γ energy is expected to decrease faster than L, when Sn is incorporated into Ge. Thus, it is qualitatively clear that alloying Germanium, which features only a slight difference of about 140 meV between Γ and L, with Sn would turn the alloy into a direct bandgap semiconductor. Since the effective mass of Γ electrons is an order of magnitude smaller than that of L electrons,[37,38] a strong boost in carrier mobility can be expected, as soon as a considerable number of electrons occupy states at Γ, thus in case of direct bandgap alloys.[22] High Sn incorporation may allow even inverse bandgap regimes or topological semimetal phases for exciting new physics.[39,40] For example, certain two-dimensional arrangements of hydrogenated GeSn alloys are expected to be 2D topological insulators (*quantum spin hall insulators*).[41]
Silicon incorporation on the other hand acts diametrically and decreases the valley difference $\Delta E = E_L - E_\Gamma$, later on referred to as directness, making the alloy 'more indirect'.[42] This interplay between Si and Sn is the secret for designing dedicated heterostructures.[43,44]

For $\mathrm{Si}_x\mathrm{Ge}_z\mathrm{Sn}_y$ alloys (GeSn in case of $x = 0$), the band energy of the critical points can be empirically found by quadratic interpolation of the constituents band energies

$$E^\Lambda = E^\Lambda_{\mathrm{Si}}\ x + E^\Lambda_{\mathrm{Sn}}\ y + E^\Lambda_{\mathrm{Ge}}\ z - b^\Lambda_{\mathrm{SiGe}}\ x\ z - b^\Lambda_{\mathrm{GeSn}}\ y\ z - b^\Lambda_{\mathrm{SiSn}}\ x\ y, \tag{2.1}$$

where $x/y/z$ correspond to the Si/Sn/Ge concentrations in the alloy (and $z = 1 - x - y$), E^Λ describes the band energy at the valley $\Lambda = \Gamma, L$ or X and b denotes the bowing parameter for the binaries.[49,50] Knowledge of exact bowing values are of strong importance for prediction of efficient heterostructure designs and will be further discussed in section 4.2.2.

Table 2.1 – High symmetry point energies of elemental Si, Ge and α-Sn at 0 K[42,45] and lattice constants.[46–48]

Element	E_Γ(eV)	E_L (eV)	E_X (eV)	lattice constant (Å)
Si	4.10	2.23	1.17	5.4198
Ge	0.90	0.76	1.16	5.6578
α-Sn	-0.41	0.12	0.91	6.4892

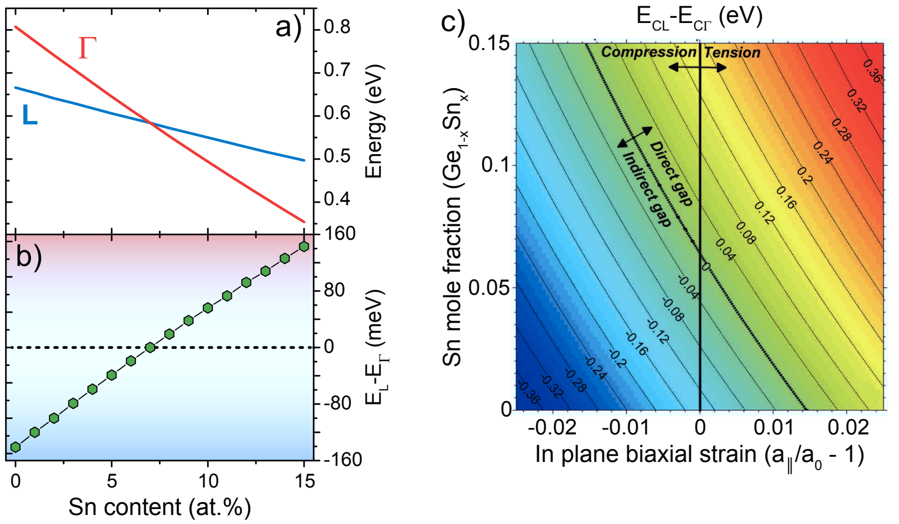

Figure 2.2 – a) Γ- and L-valley position for cubic GeSn alloys reveal an indirect-to-direct bandgap transition above ∼7 at.%. b) Higher Sn contents lead to an increased directness of the material. c) Influence of biaxial strain on GeSn band structure. Reprinted from,[53] with the permission of AIP Publishing.

The exact theoretical value of Sn incorporation, needed for the indirect-to-direct transition in cubic GeSn to occur, rather spreads in literature between 4.5–17 at.%, depending on the employed theoretical model.[32,37,51–53] Calculations, which are performed in cooperation with the University of Leeds and employ parameters from the supplementary of ref.,[18] are shown in **Fig. 2.2**a and give a value for the indirect-to-direct transition of about 7 at.%. To maximize the number of carriers at the direct Γ-valley, even higher Sn contents well above 10 at.% are required to ensure alloys with a high directness, as shown in Fig. 2.2b. Systematic investigations of temperature-dependent photoluminescence of GeSn alloys and subsequent modeling of the data with a joint-density-of-states model revealed an experimental value of about $8-9\,\%$,[18] and was later supported by lasing studies of underetched, and thus strain-free, GeSn structures.[19]

Besides incorporation of Si and Sn, the presence of biaxial strain has strong impact on the electronic band structure. Due to the large lattice mismatch of the single elements (c.f. Table 2.1), alloys grown on top of Si or Ge buffers will always possess a considerable amount of strain. In the calculation's code, the influence of atom's displacement from their cubic lattice positions on band structure is described by deformation potentials. For the Γ bands at the center of the Brillouin zone, those are applied within an 8-band $k \cdot p$ model to include the interaction of bands.[54,55] For the conduction band L-valley, it is sufficient to include the deformation potentials within the effective mass method.[56] Qualitatively, tensile strain acts very similar as the incorporation of Sn atoms, pulling down the conduction band faster at Γ compared to L, as predicted also for elemental Ge.[57,58] On the other hand, this results in compressive strain counteracting the effect of Sn incorporation, as visible for GeSn alloys in Fig. 2.2c from reference,[53] or similar for SiGeSn ternaries.[59] The presence of compressive strain, for example in GeSn films grown coherently on top of Ge buffers, necessitates higher amounts of Sn for the indirect-to-direct transition to occur. This implicates that epitaxy of defect-free GeSn films with very high Sn contents alone won't help much for the formation of a direct bandgap material, as the positive effect of Sn incorporation is always masked by the increased compressive strain in the sample.

Thus, the formation of efficient heterostructures for light emitters poses a number of requirements:

1. GeSn, without Si incorporation, shall be used as active material with an as high Sn incorporation as possible, to ensure a high directness of the material.
2. At the same time, the active layer needs to be at least partially relaxed on top of the grown Ge or Si buffer layer.
3. For carrier confinement by cladding layers, SiGeSn ternaries containing high amounts of Si are ideal candidates. However, a tradeoff between high Si incorporation and emerging tensile strain in the layer, reducing carrier confinement anew, needs to be found.

While the results on the formation of GeSn and SiGeSn layers are presented later in chapters 3 and 4, the next section will shed light on the general challenges in epitaxy of this material system, especially regarding the above mentioned heterostructure requirements.

2.2 Growth technique

Fueled by the promising electronic structure of Sn-based alloys, a number of different epitaxy techniques were developed over the years. Nowadays, GeSn alloys can be formed directly by *molecular beam epitaxy* (MBE),[60–68] or rely on post-recrystallization techniques as for *magnetron sputtern*,[69,70] *solid phase epitaxy*[71,72] or *pulsed laser induced epitaxy*.[73] The latter ones often produce polycrystalline layers and do not offer device quality yet. Due to their flexibility regarding the substrate, however, they're promising for targeting tandem solar cells[74] or flexible photonics.[75,76] MBE-grown films on the other hand, suffer from epitaxial breakdown related to surface roughening from the low growth temperature.[77] This epitaxial breakdown hampers growth of thick and strain-relaxed layers, which are required for direct bandgap material as discussed in the previous section. Other techniques, such as solution-processing, are adequate only for synthesis of nanocrystals and not bulk layers.[78]

Historically, chemical synthesis via *chemical vapor deposition* (CVD), a technique commonly used in semiconductor industry, was proposed to circumvent these challenges. But since the lowest order Sn-containing hydride stannane (SnH_4) is unstable even at room temperature,[79] epitaxy from chemical reactions required the development of deuterium-stabilized SnD_4 in the 2000s.[80,81] Nowadays, several CVD techniques are available, also from metal-organic precursors (MOCVD),[82,83] requiring ultra high vacuum (UHV-CVD),[84–86] atmospheric pressures (AP-CVD)[87] or reduced-pressure (RP-CVD) environment.[88–94] Employing gold (Au) nanoparticles as catalyst, also vapor-liquid-solid (VLS) growth of GeSn nanowire arrays and even axial- and radial-heterostructured nanowires were shown.[95–97]

Since a lot of growth techniques for GeSn epitaxy are available nowadays, research has also focussed on formation of ternary SiGeSn alloys. Due to their larger bandgap, numerous applications in opto-[98] and nanoelectronics,[99] as well as photovoltaics[100] can be foreseen. The incorporation of considerable amounts of Si, however, poses even additional challenges compared to GeSn, since thermal budget constraints, discussed in the following section, limits growth temperatures to maximum values of around 425 °C.

For our studies of (Si)GeSn and later on heterostructures a special designed RP-

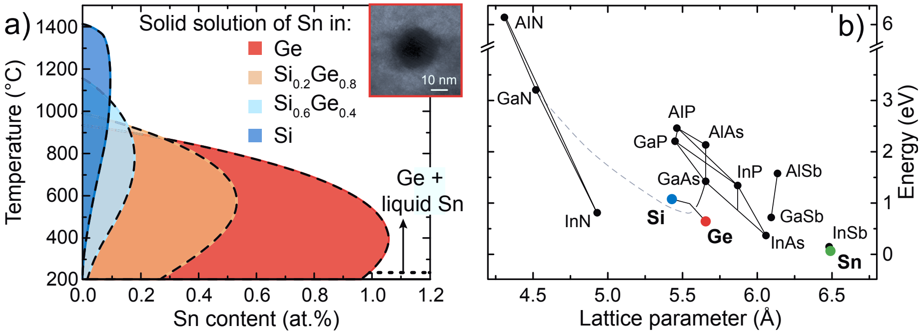

Figure 2.3 – a) Si-Ge-Sn phase diagram shows the small solid solubility range in that system. Adapted with permission of the Electrochemical Society from Ref. [102]. Inset: Sn-rich precipitation after thermal annealing. b) Bandgap energy versus lattice parameters of several semiconductors. Adapted from Ref. [103]

CVD system was used, which offers advantages concerning the specific challenges of Sn-based epitaxy, as discussed in the next subsections.

2.2.1 Growth challenges

Including Sn into group IV alloys poses tremendously higher challenges compared to Si-Ge epitaxy. While Si and Ge are a fully miscible system over the whole composition range,[101] only a very small part of the GeSn binary phase diagram is a solid solution.

In **Figure 2.3**a, an enlarged view on the Ge-rich part of the phase diagram is shown in red. Herein, it can be seen that only a maximum value of slightly above 1 at.% Sn in a Ge matrix forms a solid solution at around 400 °C.[33,104] Higher Sn-containing alloys cannot be maintained in a thermodynamically stable mixture, as both phases would separate into Ge and either solid or liquid β-Sn (for $<$ or $>$231 °C, respectively). Regarding silicon as matrix for the solute Sn, depicted in Fig. 2.3a in blue, the maximum solid solubility is given at an even smaller value of about 0.1 at.%.

From previous theoretical considerations in section 2.1 it is known, however, that GeSn alloys with Sn incorporations above about 10 at.% are mandatory to obtain direct bandgap material. Thus, only growth far away from equilibrium conditions,

e.g. CVD or MBE growth, is able to accomplish this goal.
During epitaxy, phase separation is mainly driven by *surface segregation*.[105–108] In GeSn alloys it is energetically favorable for a Ge adatom to switch its position with a subsurface Sn atom.[77,109] This exchange process can be described by a characteristic segregation length[110,111]

$$\Delta_s \propto \frac{1}{\sqrt{R}} \cdot \exp\left(-\frac{E_s}{k_B T}\right), \tag{2.2}$$

using the growth rate R, Boltzmann constant k_B and temperature T. The activation energy E_s is linked to surface diffusion and the mentioned energy gain by exchanging matrix and solute atom. This relationship offers two different paths for dealing with surface segregation. By lowering growth temperature the exchange rate between the atoms can be strongly reduced, while the time frame for exchange is reduced at higher growth rates. Thus, for suppression of surface segregation epitaxy at smallest possible temperatures is beneficial, when high growth rates can be maintained.
Generation of Sn precipitates inside the GeSn alloy is the second crucial phase separation mechanism. Due to the distinctly higher energy barriers (diffusion of Sn atoms and high local strain values), this mechanism is important in particular during post-epitaxial thermal annealing.[111–113] The inset in Figure 2.3a demonstrates the formation of a Sn precipitate after thermal annealing in a TEM micrograph. Thermal annealing above growth temperature can thus not be considered useful for strain relaxation,[91,114] but may be interesting for the formation of Sn-rich nanocrystals.[115–117] Other techniques for enhancing thermal stability are discussed in literature, for example the incorporation of carbon into GeSn.[118,119]
A further challenge arises from the large lattice constant differences between Si, Ge and Sn (see also Table 2.1). As visible in Fig. 2.3b, the over 16 % lattice mismatch exceeds even most values from III-V materials, and will result in very defective layers with large threading dislocation (TD) densities, when grown on bulk Si wafers. The critical thickness for strain relaxation for example of bulk Ge, grown directly on Si, is at around 3-4 monolayers.[120] Hence, growth of thick GeSn layers and devices will be performed on top of about 2.5–3 µm Ge *virtual substrates* (Ge-VS), produced in a different reactor in advance, to minimize the lattice mismatch to the buffer. These buffers further offer very smooth surfaces (∼0.5 nm) and a low TD density

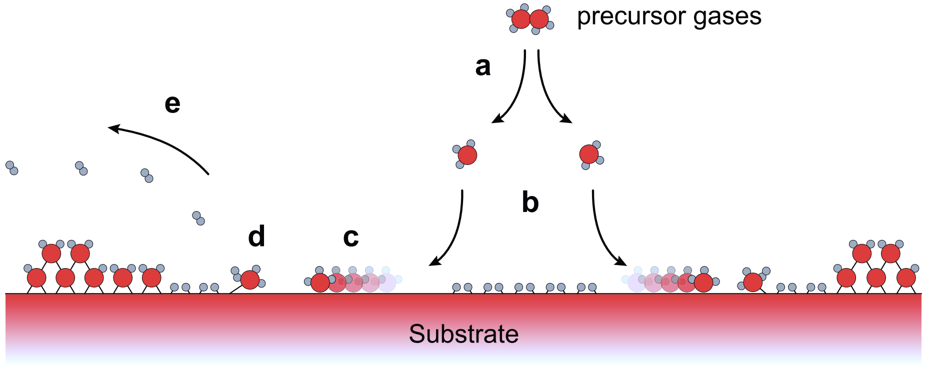

Figure 2.4 – Overall reaction in *chemical vapor deposition*. The precursor gas needs to a) decompose, then adsorb b) and diffuse c) on the substrate. d) Chemical reactions with surface atoms dissociate the precursor and incorporate it into the layer. Undesired by-products desorb and stream out of the reaction chamber.

($\sim 5 \times 10^6\,\mathrm{cm}^{-2}$).[121]

2.2.2 Reduced-pressure CVD epitaxy

Chemical vapor deposition relies on decomposition of adequate precursor gases and the incorporation of their respective atoms on the substrate into the grown film. One can divide the overall process into several different key steps[122]

a decomposition and mass transport into the boundary layer close the substrate,

b adsorption on the substrate's surface,

c surface diffusion,

d chemical reaction and nucleation and

e desorption of volatile reaction by-products,

which are depicted also in **Fig. 2.4**. First, as marked by a, the precursor gas needs to decompose and be delivered homogeneously to the wafer (often using H_2 or N_2 as carrier gas), before adsorbing onto the substrate's surface, as marked by b. Close to the wafer surface a thin *chemical reaction boundary layer* is formed, in which most of

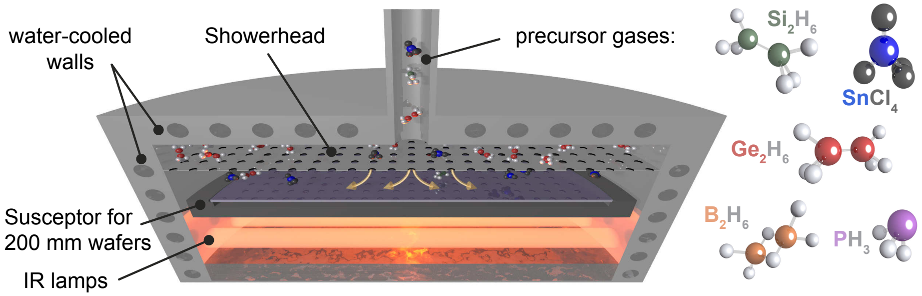

Figure 2.5 – Schematic rendering of the used RP-CVD reactor and precursor gases.

the gas phase pyrolysis occur.[123] Once impinged on the surface, the adsorbed radicals will diffuse to appropriate lattice sites, as shown in 2.4c. This is a first critical step, especially in low-temperature epitaxy. In there, the small growth temperature strongly reduces adatom mobility and prevents them from crossing step edges, which results in a transition from the desired layer-by-layer growth (Frank-van der Merwe growth mode) to a growth of isolated islands (Volmer-Weber growth mode). Macroscopically, this leads to a severe layer roughening, which has been shown for example in low-temperature epitaxy of silicon[124] and germanium.[89,125]

Next, as shown in Fig. 2.4d, the precursor needs to react with surface atoms, so that it is incorporated into the film. Desorption of the surface-bonded hydrogen to obtain open lattice sites has been shown to be growth rate limiting step in low-temperature (<325 °C) Ge epitaxy,[126] but can be promoted by appropriate choices of precursor and carrier gas.

In the end, as shown in Fig. 2.4e, the unwanted reaction by-products, as well as excess precursor, will desorb from the surface and leave the reactor exhaust.

The exact regime, in which growth occurs, strongly depends on the chosen growth parameters, mainly reactor temperature, pressure and choice of precursor gases, thus different growth rate-limiting steps can emerge. Since epitaxy of Sn-based alloys imposes severe constraints on the thermal budget, high growth rates needs to be ensured for example by appropriate choices of precursor gases. In this respect, the CVD reactor used for sample growth in this thesis, also offers several design benefits.

All layers were grown on full 200 mm wafers in an industry-compatible *AIXTRON*

Tricent RP-CVD reactor, from which a schematic rendering is shown in **Fig. 2.5**. The most conspicuous difference, compared to frequently used horizontal CVD tube furnaces, is the showerhead, which allows a fully homogeneous precursor distribution over the wafer surface. Wasted deposition on showerhead and reactor walls can be prevented in this design by water-cooling both. Only the graphite susceptor is heated from underneath by nine infrared lamps, so chemical reactions in the gas phase are suppressed and take place only in the boundary layer and on top of the hot wafer surface.

Different precursor gases are used for deposition of the group IV materials, as also shown in Fig. 2.5. The second-order hydrides digermane (Ge_2H_6) and disilane (Si_2H_6) assure higher growth rates, compared to commonly used germane (GeH_4).[90,127] The reason lies within the weaker bond strength, the Ge–Ge bond (2.9 eV) in digermane molecules being much smaller compared to the Ge–H bond (3.6 eV) in germane.[128] Furthermore, digermane is able to overcome one additional limitation in low-temperature growth, the above mentioned hydrogen desorption, by the following chemical reaction on the wafer surface:

$$\mathrm{Ge_2H_6} + \overline{H} \rightarrow {}^{\bullet}\mathrm{GeH_3} + {}^{\bullet}\mathrm{GeH_3} + \overline{H} \rightarrow \mathrm{GeH_4} + \overline{\mathrm{Ge}}\mathrm{H_3} \tag{2.3}$$

It is able to open hydrogen-terminated lattice sites by first splitting up their Ge – Ge bonding, formation of germane with an adsorbed H-atom (marked by the bar above) and adsorption of the remaining GeH_3 radical on the surface.[89]

Nowadays, most CVD growth processes, such as in this thesis, rely on the commercially available Sn precursor tin tetrachloride ($SnCl_4$), which has been shown to enable CVD growth without any precursor instability issues.[87] It is liquid at room temperature and requires a bubbler source for vaporization. Due to its composition, it may also help in our growth process. The presence of chlorine may lead to an exothermic reaction with the adsorbed hydrogen, which may provide additional local energy, beneficial for fueling the chemical reactions on the surface or boost adatom mobility. Combined with the choice of nitrogen as carrier gas during growth process, the described scheme leads to enhanced GeSn growth rates of still around $35\,\mathrm{nm\,min^{-1}}$ at 400 °C, sufficient for suppression of Sn surface segregation.[92] Furthermore, the dopant precursors diborane (B_2H_6) and phosphine (PH_3) can be

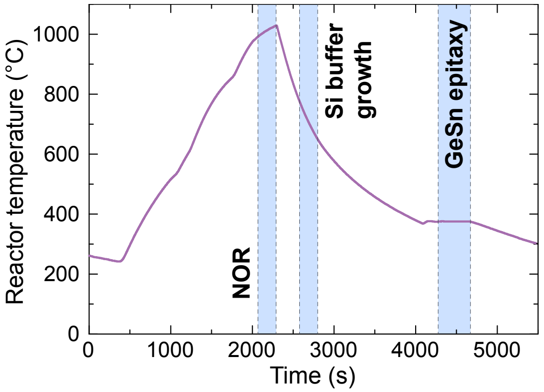

Figure 2.6 – Typical GeSn growth process on top of Si. Prior GeSn epitaxy, an *in-situ* hydrogen bake is performed, followed by a Si buffer growth, before deposition of the GeSn layer itself.

employed for doping, which will become important for the in-situ growth of complete diode structures, as later discussed in chapter 5.

Since the full epitaxial process also includes additional modules, such as *pre-epitaxial* cleaning, the next section will give a short overview on a typical GeSn epitaxial process.

2.2.3 Exemplary GeSn process

Prior growth, the native oxide has to be removed from the wafer surface. Since also the Ge-VSs feature a thin Si capping layer of ∼1 nm for passivation, the same chemistry can be used for both types of substrates. In a fully automated *SEMITOOL Raider* cleaning tool, HF vapor chemistry (plus additional isopropyl alcohol for surface wetting) chemically removes the SiO_2, without any water rinsing, and leaves a mostly hydrogen-terminated wafer surface, before transfer into the reactor chamber.

A typical growth process of a 100 nm GeSn layer on a Si wafer in that reactor is shown in **Fig. 2.6**.

The temperature ramping during the process, as well as significant process parts, is shown in Fig. 2.6. Since temperature is measured by six thermocouples inside the susceptor itself, deviations between the monitored and the wafer surface temperature may be present. Before the actual deposition starts, the reactor temperature is ramped up for a three minute hydrogen bake, also denoted as *native oxide removal* (NOR). Here the remaining oxide residues, as well as other contaminants such as F or C atoms are removed, to start epitaxy on a pristine and fully hydrogen-passivated surface. Potential defects, created during the high-temperature bake, shall be overgrown during the following Si buffer growth of a few tens of nm (only when grown on Si wafers). Subsequent ramping of the reactor temperature to the desired growth temperature, in this case 375 °C, takes longer compared to reactors with direct heating of the wafer. Owing to the massive graphite susceptor, this reactor design is not suited for quickly alternating temperature ramps. Directly before GeSn epitaxy, the different precursor gases are mixed and injected into the chamber using nitrogen as carrier gas. After growth of the GeSn layer, the wafer can be unloaded when cooled down to about 300 °C.

In the previous section, the foundations were laid for investigation of Si-Ge-Sn epitaxy. The requirements for both the active direct bandgap material and carrier-confining cladding materials were outlined. Severe constraints in the Sn-based group IV material system were highlighted and our approach using RP-CVD for epitaxy is discussed. In the next chapter, this knowledge is adopted to systematically investigate the growth of direct bandgap GeSn alloys for active group IV optoelectronics.

3 Direct bandgap GeSn epitaxy

Contents

This chapter deals with epitaxy of direct bandgap GeSn alloys, especially designed for heterostructure light emitters. As it was outlined in previous section 2.1, the two main premises for direct bandgap alloys are high Sn incorporation and strain-relaxed layers.

While several groups demonstrated potentially interesting alloys above 15 at.% Sn incorporation,[67,93,115,129] the exact growth kinetics are only scarcely investigated yet.[93,94,130]

In the following, first the influence of different precursor flows and temperature on growth kinetics and the alloy's properties are investigated, aiming for ideal conditions to produce high Sn content layers. Next, strain-relaxed layers are grown, highlighting creation and evolution of misfit defects and to examine optical properties of the alloys. Parts of the results in the upcoming chapter have previously been published under reference.[92]

3.1 GeSn growth kinetics

The three main dimensions influencing CVD growth are reactor temperature, reactor pressure and gas flow. As our reactor features cooled walls and gas phase and as the pressure can be set to a fixed value, gas flow is the most complex one and will be investigated first. It includes not only the amount of the different precursor's flows, but also carrier gas and total flow. The latter ones were fixed at a few slm (*standard litre per minute*) of nitrogen, as nitrogen turned out to deliver higher growth rates at least in case of bulk Germanium growth in previous investigations.[29,90] Since the utilized reactor has several dummy sources, the total flow can be kept constant during growth, even for arbitrary changes in the precursor's flows. Further, if not stated otherwise, the alloys in this first section were grown on bulk Si wafers, so deviations from the optimized growth parameters are more easily observed.

3.1.1 Precursor flow dependencies

For the following investigations, all layers were grown at a fixed temperature of 375 °C and a reactor pressure of 60 mbar.

Digermane flow

First, the influence of digermane flow alone is investigated, keeping the $SnCl_4$ partial pressure constant at 0.6 Pa.

Figure 3.1a shows *Rutherford Backscattering Spectrometry* (RBS) spectra of a 97 nm $Ge_{0.92}Sn_{0.08}$ sample. This powerful technique facilitates 1.4 MeV He^+ ions to extract information on layer stoichiometry and thickness up to several hundred nm's from the backscattered spectra in random alignment (blue in Fig. 3.1a). Herein,

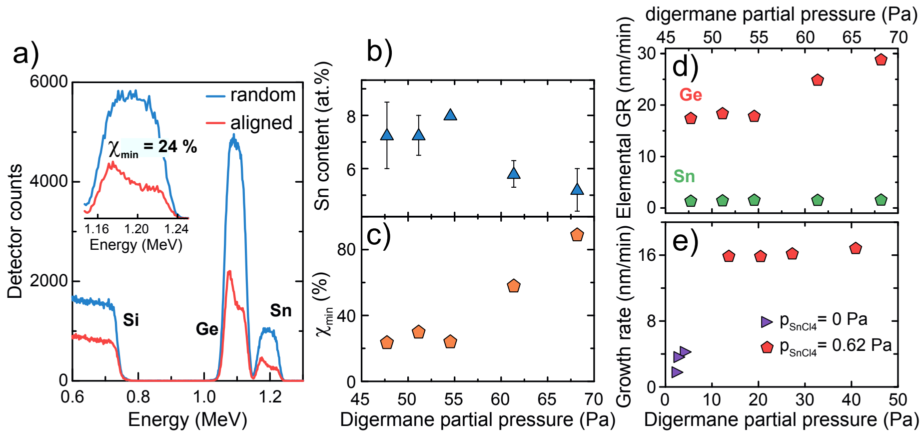

Figure 3.1 – a): Random and channeling RBS spectra of a 100 nm GeSn sample. Sn incorporation b) and minimum channeling yield χ_{min} c) in alloys grown on *bulk Si* with varying digermane flows. d): Elemental growth rates (GR) for GeSn alloys and pure Ge e).

the different elements, Ge and Sn from the alloy plus Si from the substrate, are well separated due to varying backscattering losses, dependent on their atomic masses. Secondly, RBS can also be employed when the sample is aligned in the (001) crystalline direction. In this case (red spectrum in Fig. 3.1a) the backscattered signal is strongly reduced, as incoming ions are able to follow the aligned crystal channels. To quantify this, the ratio between both signals, the minimum channeling yield χ_{min}, is evaluated (theoretically possible for each element individually) close to the sample surface, and amounts for Sn to 24 %, in this case (see inset). This value indicates adequate growth parameters, considering a value of 100 % for amorphous layers, although χ_{min} values as small as 5 % are reachable using high-quality Ge-VS.

When systematically tuning the digermane partial pressure between 48–68 Pa, different effects occur. Overall, it seems that there is only a small stable region around 55 Pa for GeSn growth with the applied Sn precursor flow, as shown in Fig. 3.1b. Up to that point, the layer quality still is good enough, as indicated by χ_{min} in Fig. 3.1c. When the digermane flow is ramped further up, however, a slight decrease in Sn incorporation can be seen in Fig. 3.1b, caused by the increased elemental growth rate of Ge, visible in Fig. 3.1d. In this case, Sn atoms are also not built-in homogeneously anymore, as indicated by the error bars. Often Sn accumulation towards the surface or regions with strongly varying concentrations can be observed, resulting in the worsened layer qualities shown in Fig. 3.1c.

The physical reason for these correlations may be the following: Since the growth rate does not strongly depend on the digermane flow (until ∼55 Pa), supply of precursor gas isn't the limiting step for GeSn growth at these conditions. This is further underlined by investigations of the Ge elemental growth rate in Fig. 3.1e. It is visible here, that for pure Ge there is indeed a strong linear dependence of growth rate on digermane flow (violet triangles). When $SnCl_4$ is added, however, the growth rate is nearly constant over a wide range until about 40 Pa (red pentagons). For even higher digermane flows, as investigated in Fig. 3.1b, there may now arise a surface poisoning from the high number of germane radicals, occupying surface sites and changing the surface chemistry.

In the following, the influence of $SnCl_4$ flow is investigated more detailed.

Tin tetrachloride flow

As tin tetrachloride is a liquid precursor, it requires a bubbler for vaporization. In there, an appropriate temperature results in a given vapor pressure of the precursor. To minimize the number of parameters, temperature of the bubbler bath was kept constant for the next series, while only the flow of carrier gas through the bubbler was altered.

In contrast to the weak influence of digermane flow, tuning of the tin tetrachloride flow clearly has a linear influence on Sn incorporation in the alloy, as visible in **Fig. 3.2**a. Still, not the complete investigated region is useful for epitaxy of high-quality layers. Alloys grown below a $SnCl_4$ partial pressure of about 0.4 Pa show amorphous character and increase in quality only with elevated $SnCl_4$ flows, as the evolution of χ_{min} in Fig. 3.2b shows. For highest Sn flows at around 0.8 Pa, however, Sn incorporation starts to become inhomogeneous again. From the elemental growth rates in Fig. 3.2c it can be seen that only the incorporation of Sn atoms is affected by changes in $SnCl_4$ partial pressure.

Although the exact reaction scheme of the employed precursors is not fully understood yet, some indications can be drawn. The influence of tin tetrachloride on Sn

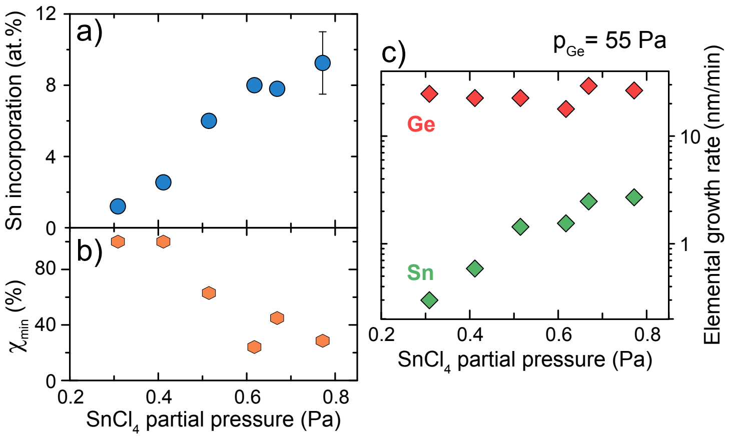

Figure 3.2 – Impact of $SnCl_4$ tuning on Sn incorporation a), layer quality b) and elemental growth rates c).

incorporation is superlinear, as visible in Fig. 3.2 a), much stronger compared to the impact of digermane. At the same time, Sn incorporation in the alloy is always higher than the gas phase ratio would suggest. Thus, it can be concluded that $SnCl_4$ has a higher reaction order, it is easier incorporated. Similar findings have also been shown by MARGETIS et al., who investigated CVD growth from *germane* and tin tetrachloride.[94] However, as the energy of the Sn–Cl binding (3.3 eV)[131] is even larger than the digermane binding (2.9 eV),[128] the chemical reaction path here most likely features additional reactions, e.g. with the involvement of chlorine.

As the previous investigations showed, only a small window in the parameter space is suitable for epitaxy of high quality layers. To still be able to tune the stoichiometry at a given temperature and pressure, as needed later for heterostructures, the effect of *simultaneously* tuning $SnCl_4$ and Ge_2H_6 will be investigated.

Fixed $SnCl_4/Ge_2H_6$ partial pressure ratio

When optimized growth parameters for both precursor flows are found, *simultaneous* tuning of both Sn and Ge precursors has the advantage that all chemical reactions stay in balance, from which a higher layer quality can be expected.

Indeed as **Figure 3.3**a shows, this type of tuning allows formation of alloys with

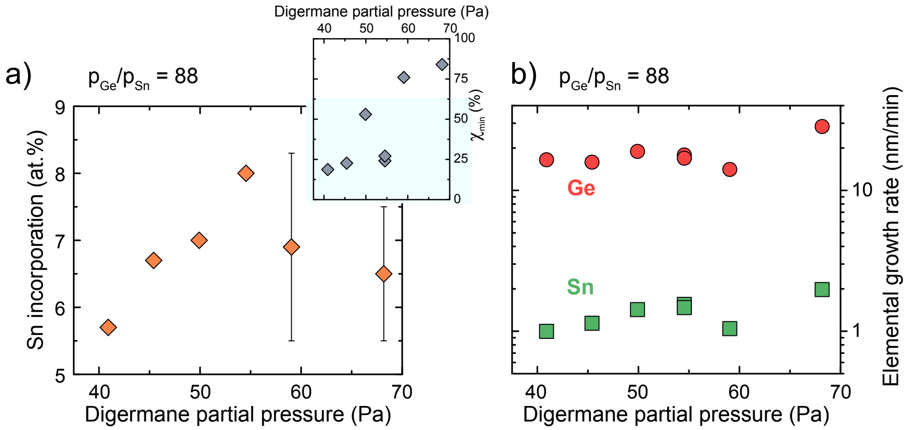

Figure 3.3 – Simultaneous tuning of both precursors allows constant tuning of Sn incorporation a) maintaining a small χ_{min} values. b): Elemental growth rate evolution.

constant Sn incorporations in a range of about 5.5–8 at.%. While the range may be extended also to even smaller Sn values, higher precursor flows result in inhomgeneous layers with deteriorated quality, as depicted in the inset of Fig. 3.3a. In the linear regime, however, the small minimum yield values show a good crystalline quality, while the sample at digermane partial pressure of about 50 Pa may just be an outlier.

This approach, however, will be limited to the bottom from an overall growth rate reduction, the latter one already visible in Fig. 3.3b. Too small growth rates at a given temperature can promote Sn surface segregation, on the other hand also layer roughening may occur.

3.1.2 Temperature dependence

After the previous sections discussed the influence of precursor gases on the epitaxy, this section deals with the impact of growth temperature. Since epitaxy takes place in a low-temperature regime below 400 °C, a huge impact is presumed, as most chemical reactions and processes will be kinetically limited.

For this series, GeSn alloys were pseudomorphically grown at a fixed precursor ratio $p_{\mathrm{Ge_2H_6}}/p_{\mathrm{SnCl_4}}$ of about 88 on Ge-VS, tuning only the reactor temperature. Corre-

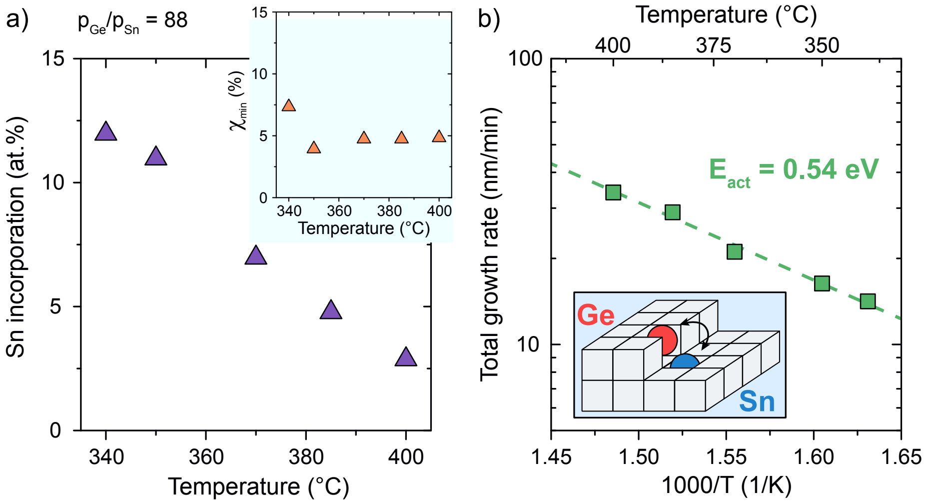

Figure 3.4 – a) Strong impact of growth temperature on Sn incorporation, maintaining high atom substitutionality (upper inset). b) ARRHENIUS-plot of GeSn growth rate versus reversed temperature, revealing a kinetically-limited growth regime.

spondingly, the alloying degree is strongly affected, as visible in **Fig. 3.4**a. The Sn atomic fraction in the alloy is elevated from 2.7 at.% to 12 at.%, when temperature decreases between 400–340 °C. At the same time, all layers show excellent atom substitutionality, as represented by χ_{min} in the inset of Fig. 3.4a. However, as previously already mentioned, the differences in thermal decomposition of digermane and tin tetrachloride cannot explain the tremendous increase in Sn incorporation.

Segregation of Sn, as discussed already in section 2.2.1, is a process, which is also strongly affected by temperature. As schematically depicted in the inset of Fig. 3.4b, subsurface Sn atoms can switch positions with Ge adatoms at step edges before overgrowth, strongly limiting the number of built-in Sn atoms. This exchange mechanism, and maybe also subsequent desorption of the Sn radical, is certainly strongly suppressed at lower temperatures and may lead to the observed increase in Sn incorporation.

To prove a kinetically limited growth regime, an ARRHENIUS-plot of the total GeSn growth rate as function of the reverse temperature is given in Fig. 3.4b. An exponential growth rate increase from 14 nm min^{-1} to 34 nm min^{-1} is observed at elevated temperatures, as expected in a kinetically limited growth regime. The extracted activation energy of 0.54 eV fits close to the value (0.47 eV), previously determined by other groups.[93]

This first part of the GeSn epitaxy chapter featured only investigations on pseudomorphic and relatively thin GeSn samples to learn more about the growth kinetics and optimal parameters. As growth of high-Sn content layers was shown possible, the next section deals with the second requirement of direct bandgap layers, that is strain relaxation.

3.2 Relaxed layer growth

The formation of strain-relaxed layers in the GeSn material system is not a straightforward task. Approaches from the SiGe system, relying on thermal annealing[132] or ion implantation,[133] are not useful as they would lead to severe Sn diffusion. The most obvious solution would be the epitaxy of layers well above the critical thickness for strain relaxation. In that case, plastic relaxation sets in by formation of misfit dislocations at the interface to the substrate. Still, it poses several challenges, as defects may lead to a reduced layer quality and also impair the optical and electrical properties of the material.[134–136]

3.2.1 Thick layer growth kinetics

Epitaxy of thick GeSn layers is possible using optimized growth parameters, as determined previously in section 3.1.1. However, certain changes in growth kinetics are observed in thicker layers, which are investigated more detailed in the following. **Figure 3.5**a and b show *secondary ion mass spectrometry* (SIMS) analysis of two GeSn alloys with an average Sn incorporation of 12–12.5 at.% and thicknesses of 280 nm and 970 nm, respectively. In those measurements, depth distribution of Sn and Ge atoms (here in arbitrary units) is evaluated. In the thinner sample in Fig. 3.5a, two distinct regions with varying Sn contents, as marked in different gray tones, are visible, despite no changes in growth parameters. The lower ∼180 nm part of the alloy features a constant, but slightly smaller Sn incorporation than the top part of the alloy. The same is true in even thicker layers, as shown in Fig. 3.5b. Also here,

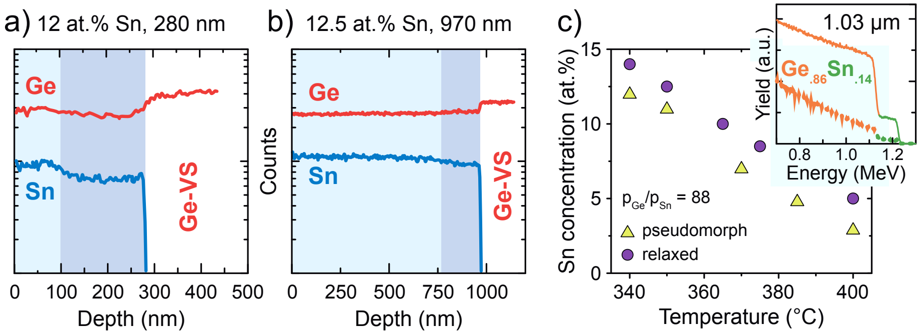

Figure 3.5 – SIMS spectra of 280 nm a) and 970 nm b) thick GeSn alloys show two distinct regions with different Sn incorporations. The trend of increased Sn incorporation is visible over the whole growth range c), while the layer quality maintains high (RBS channeling spectra in the inset).

Sn content increases to a higher but constant value on top of the bottom ∼ 200 nm. As will be shown in the next section, this value coincides with the thickness, where strong plastic strain relaxation occurs. The larger lattice constant, resulting from the diminishing residual strain, allows for a higher Sn incorporation on top of the GeSn template. Similar behavior was also found for GeSn alloys, grown in different reactors or with different precursor and carrier gases.[20,94]
The trend of increased Sn concentration is visible over the whole growth range, as depicted in Fig. 3.5c. In all layers, an increase of 1.5–2 at.% in the top alloy region is visible. This peculiar property of epitaxial GeSn layers is further beneficial for optoelectronic applications, as not only strain relaxation, but also the higher Sn content helps them becoming more direct.

Not only changes in Sn incorporation, but also in growth rate occur during thick layer epitaxy. Comparison between pseudomorphic and relaxed layers in **Fig. 3.6**a show stronger differences at lower growth temperatures, i.e. higher Sn contents. At 340 °C for example, a diminishing from 14.2 nm min^{-1} down to 10.3 nm min^{-1} is visible, corresponding to a reduction of nearly 30 %. It shall be noted that growth rate in relaxed layers is defined here as a *mean* growth rate, determined by dividing the total layer thickness by growth time, as no in-situ measurement techniques are available in our CVD reactor. The overall growth rate reduction also leads to a

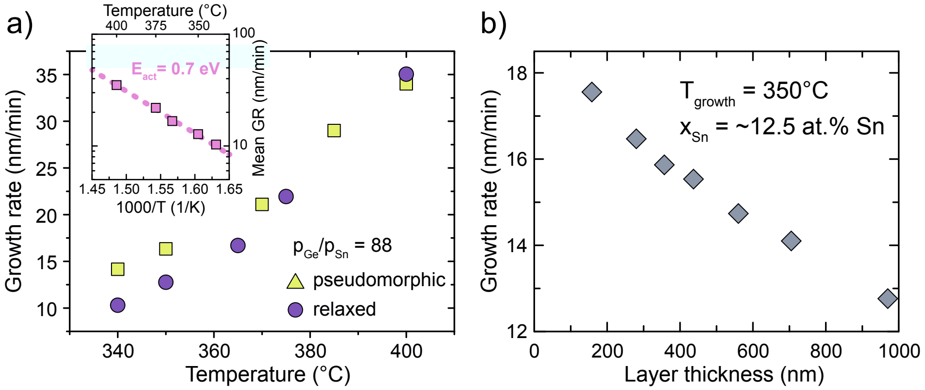

Figure 3.6 – a) Growth rate deviations between pseudomorphic and relaxed GeSn layers lead to increased activation energies in thick layer growth (inset). b) In this, growth rate gradually decreases, possibly related to layer roughening.

slightly reduced activation energy compared to pseudomorphic layers (c.f. Fig. 3.4b on page 25), as shown in the inset of Fig. 3.6a.

Diminishing of the overall growth rate is a continuous process during epitaxy that is observed also by different groups[137] and is depicted in Fig. 3.6b. As discussed for the growth challenges in section 2.2.1, changes in growth rate influence the Sn segregation length and, thus, may have an impact on Sn incorporation of the alloy. Previously shown SIMS spectra, however, proved a homogeneous Sn incorporation throughout the (upper part of the) layer, despite the continuous changes in growth rate. It is thus likely that the observed growth rate changes do not originate in surface chemistry changes, but in morphological changes, such as a strong increase in surface roughness. Then, the larger *effective* surface together with adatom mobility-limiting surface steps may explain a growth rate reduction. Further investigation of surface morphology will be performed in section 3.2.3.

3.2.2 Strain relaxation

For strain determination, different techniques such as Raman spectroscopy have been performed in literature.[138–140] In this thesis, *X-Ray diffraction* (XRD) techniques were employed by a *Bruker D8* high-resolution diffractometer, using the K_α

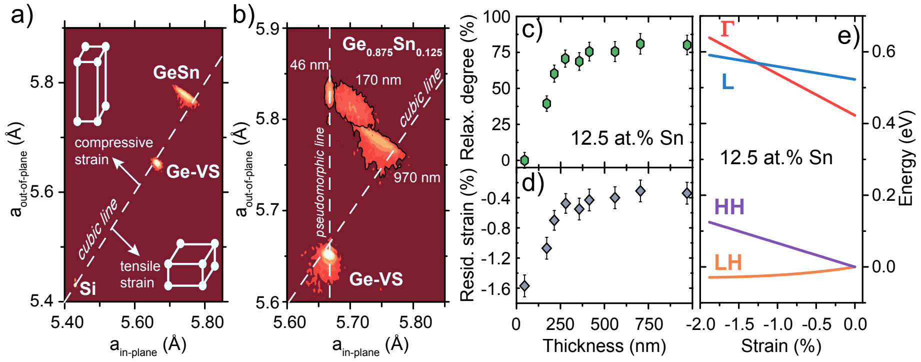

Figure 3.7 – a): Exemplary RSM of a 970 nm $Ge_{0.875}Sn_{0.125}$ layer. b): Overlay of three RSM with increased relaxation. Overview on relaxation c) and residual compressive strain d) for a series of $Ge_{0.875}Sn_{0.125}$ layers. e) Corresponding evolution of band structure for strain-relaxing $Ge_{0.875}Sn_{0.125}$ alloys.

wavelength of copper (Cu, 1.54 Å). For simultaneous acquirement of in- and out-of-plane lattice information, *reciprocal space maps* (RSM) were carried out around the asymmetric (224) or ($\bar{2}\bar{2}4$) reflex.

In **Figure 3.7**a, a typical RSM of a 970 nm thick $Ge_{0.875}Sn_{0.125}$ sample with several important features is shown. In there, three different peaks can be identified and attributed to the bulk Si wafer underneath, the Ge-VS and the GeSn layer on top. The dashed line in the middle marks the line of cubic crystals with equal in- and out-of-plane lattice constants. Thus, peaks located above the line contain compressive, below contain tensile strain. It must be noted that the Ge-VS itself is slightly tensily strained (∼0.15 %). Since Ge and Si differ in their thermal expansion coefficients, the layer will become slightly stressed when cooled down after buffer growth.[121] As expected, growth of GeSn alloys on top of Ge-VS yields compressively strained layers, which exhibit a tetragonal distortion of their crystal lattice.

The evolution of strain relaxation during thick layer growth is better followed in Fig. 3.7b. Herein, a thickness series of GeSn (about 12.5 at.% Sn) is grown and investigated. Thin (in this case 46 nm) GeSn layers grow pseudomorphically on top of the Ge-VS. They share the same in-plane lattice constant, as indicated by the dashed white line. XRD $\theta/2\theta$ scans of this layer (see Fig. A.1 in the appendix) feature regular thickness fringes, indicating a smooth interface and surface. A thicker layer of 170 nm thickness, likewise shown in Fig. 3.7b, is already partially strain relaxed. Stress is relieved plastically by formation of misfit dislocations at the interface, leading to expanding in-plane and shrinking out-of-plane lattice constants. This trend is continued in a 970 nm thick sample, moving closer towards the cubic line.

Relaxation is summarized in Figures 3.7c and d. Here the evolution of relaxation degree and residual compressive strain, respectively, can be observed. Relaxation degree R and biaxial (in-plane) strain $\epsilon_{\parallel}$ can be calculated as follows:

$$\epsilon_{\parallel} = \frac{a_{\parallel}^{\mathrm{GeSn}} - a_0^{\mathrm{GeSn}}}{a_0^{\mathrm{GeSn}}}, \quad R = \frac{a_{\parallel}^{\mathrm{GeSn}} - a_{\parallel}^{\mathrm{Ge}}}{a_0^{\mathrm{GeSn}} - a_{\parallel}^{\mathrm{Ge}}}, \tag{3.1}$$

with $a_{\parallel}^{\mathrm{GeSn/Ge}}$ being the in-plane lattice constant of GeSn and the (Ge) substrate, respectively. a_0^{GeSn} denotes the relaxed GeSn lattice constant, which can be calculated following elastic theory[141] from the determined in- and out-of-plane lattice constants:

$$a_0^{\mathrm{GeSn}} = \left(\frac{a_{\perp}^{\mathrm{GeSn}} + 2\ a_{\parallel}^{\mathrm{GeSn}}\ C_{12}/C_{11}}{1 + 2\ C_{12}/C_{11}} \right). \tag{3.2}$$

The required elastic constants C_{12} and C_{11} can be extrapolated for GeSn alloys for example from Ref. [137], or, more generally, for arbitrary SiGeSn alloys from Ref..[142] The compressive strain inside a coherently grown (on Ge) 12 at.% Sn alloy amounts to about $-1.60\,\%$, while the error bars stem from uncertainties in determination of the exact lattice constants from the RSM. This value is high enough that the grown alloy still maintains its indirect bandgap,[92,143] as can be seen from the strain-dependent band structure calculations in Fig. 3.7e.

Between 50–100 nm thickness, plastic strain relaxation sets in and leads to a rapid diminishing of the residual strain. To predict the critical thickness for strain relaxation in the SiGe system, People and Bean developed a model. In there, onset of strain relaxation is assumed, when the strain energy of the film exceeds the self-energy for formation of an isolated dislocation.[144] Later it was found that it also offers a very reasonable description of strain relaxation in the GeSn system.[67] In that respect, the expected critical thickness of about 60 nm for $\mathrm{Ge_{0.875}Sn_{0.125}}$ fits pretty well to our observations.

Once the critical layer thickness is reached, strain relaxation sets in very rapidly,

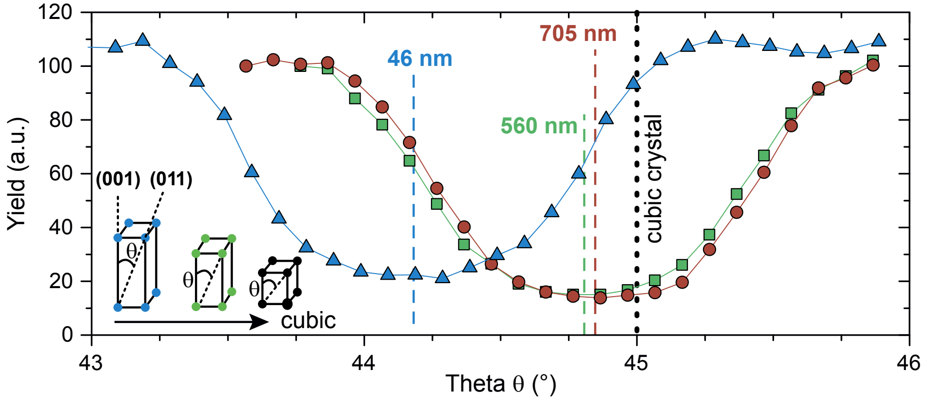

Figure 3.8 – RBS angular yield scans for alloys with increasing layer thickness. The shrinking difference $\Delta\theta_{[011]}$ between the observed values and the expected $\theta = 45°$ between [001] and [011] crystal directions indicate on-going strain relaxation.

as depicted in Figures 3.7c/d. After 300–400 nm a residual compressive strain of about −0.4 % (∼75 % relaxation) is reached, and strain relaxation begins to saturate. This behavior is also known from the SiGe material system, where µm thick layers and compositional grading are necessary to obtain fully relaxed buffers.[145,146] Nevertheless, a value of −0.40 % is sufficient to obtain a directness of about 70 meV, as the indirect-to-direct transition occurs when compressive strain surpasses below −1.27 %, as shown in Fig. 3.7e.

Since determination of material strain is such a critical value for band structure calculation and, later on, heterostructure design, it was also determined using an independent technique, that is ion channeling angular yield scans. RBS in channeling alignment, as previously presented in section 3.1.1, allows determination of the relative position of different crystal directions and is a useful tool for ascertainment of the internal layer strain.[92,147,148] In our case, angular scans were performed in the (100) plane, around the [001] and [011] crystal directions. In a fully relaxed, cubic crystal, the enclosed angle should amount to 45°. Biaxial strain, however, induces a tetragonal distortion of the crystal unit cell, altering the enclosed angle to smaller (biaxial compressive strain) or larger (biaxial tensile strain) values than 45°.

Figure 3.8 shows angular scans around the [011] direction for three different GeSn alloys with 12–12.5 at.% Sn incorporation. The 46 nm thin, pseudomorphically grown sample shows the strongest tetragonal distortion with an angular shift of 0.819°. The amount of tetragonal distortion ϵ_T, defined as the difference between in- and out-of-plane biaxial strain ($\epsilon_\parallel$ and $\epsilon_\perp$),[148] is linked to the angular shift via

$$\epsilon_T = -2 \cdot \Delta\theta_{[011]}. \tag{3.3}$$

Thus, the resulting angular shift of the pseudomorphic sample corresponds to a tetragonal distortion of −2.9 %. Strain relaxation in thicker layers of 560 nm and 705 nm can be easily observed from the reduction of tetragonal distortion. Both thick layers are closely situated near a cubic crystal, with angular shifts of 0.193° (560 nm) and 0.153° (705 nm). For comparison with XRD results, the tetragonal strain value can be converted to a biaxial strain value via elastic theory[148] following

$$\epsilon_T = \epsilon_\parallel - \epsilon_\perp = \epsilon_\parallel \left(1 + 2\frac{C_{12}}{C_{11}}\right). \tag{3.4}$$

Values of about −1.60 % and −0.30 % for the pseudomorphic (46 nm) and the strongly relaxed (705 nm) layer, respectively, are in very good agreement with strain values, previously determined by XRD in Fig. 3.7d.

3.2.3 Surface Morphology

For investigation of GeSn surface morphology and especially its evolution, *atomic force microscopy* (AFM) is employed on $10 \times 10\,\mu\text{m}^2$ big areas. AFM micrographs for a GeSn thickness series with constant Sn incorporation (previously already investigated for their strain relaxation in Fig. 3.7 c/d) are depicted in **Fig. 3.9**, with their respective layer thicknesses and rms roughnesses.

Both the Ge-VS, as well as the coherently grown GeSn layer in Fig. 3.9a&b imply smooth surfaces with only a small roughness below 1 nm. Roughness originates in slight surface undulations, a so-called *crosshatch* pattern, which is present on the surface and typical mark for regular misfit dislocations at the underlying Ge-VS/Si interface.[121]

For thicker layers, for example 160 nm in Fig. 3.9c, a higher amplitude *crosshatch*

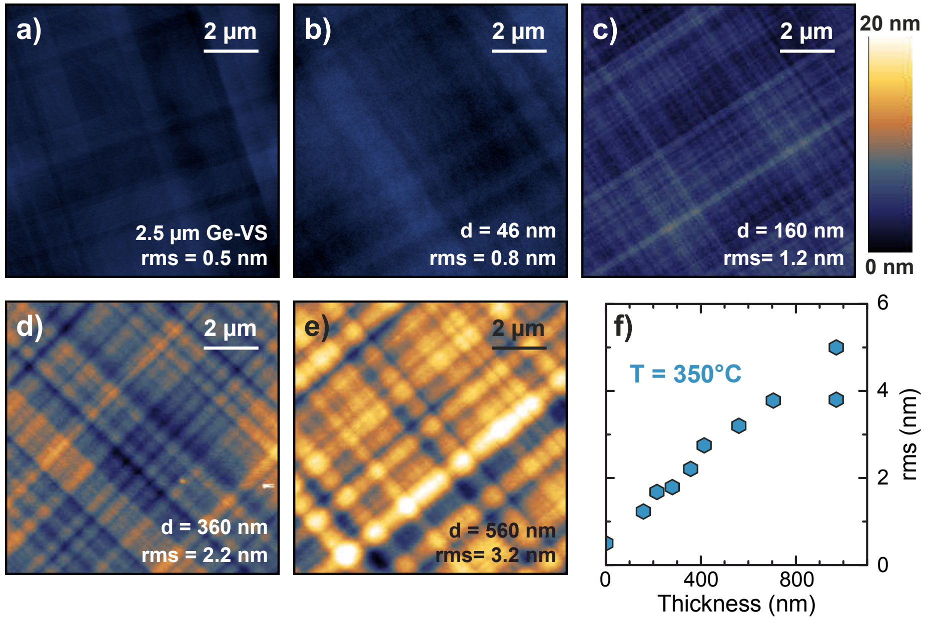

Figure 3.9 – AFM micrographs show evolution of surface morphology for Ge$_{0.875}$Sn$_{0.125}$ layers, from the Ge buffer a) to a 560 nm thick layer e). f) Linear roughness increase in thickening layers, possibly related to increased dislocation formation from strain relaxation.

starts to appear on the surface. It is aligned along the (011) and (0$\bar{1}$1) directions and related to periodic strain fields arising from misfit dislocations at the GeSn/Ge-VS interface. Thus, during strain relaxation, strain energy within the system is traded in for surface energy.[149]

Surface *crosshatch* evolves with increasing layer thickness, visible in Fig. 3.9c-e, hills and valleys on the surface start merging together. The spatial periodicity of the surface undulations in a 560 nm thick sample (Fig. 3.9e) is in a range of around 1 µm, which is several times that of thinner layers. The reason for this coalescence lies directly in the increased distance between the misfit interface and the sample surface. Strain fields, arising from the misfit dislocations, become more homogeneous, as it has been simulated for the SiGe material system.[150] One would expect this to become driving force for planarization, as growth on top of mounds is ener-

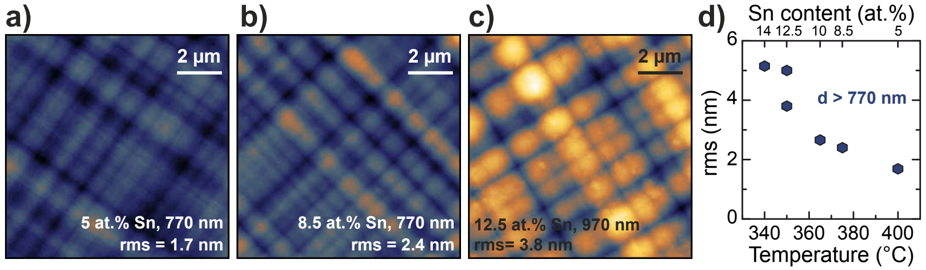

Figure 3.10 – a)-c) AFM micrographs for thick (> 770 nm) GeSn layers Sn incorporations between 5–12.5 at.%. d) Decline of surface roughness with Sn content, related to less layer misfit and higher growth temperatures.

getically not favorable anymore, leading to downhill mass transport and coalescence of mounds. At the same time as merging of mounds, however, an increase in rms is visible with elevated layer thickness in Fig. 3.9f. It linearly increases in the whole investigated range up to 4–5 nm for a 1 µm thick sample. The observed rms spread in that sample can be explained by local variations on different micrographs, as the undulation period becomes larger.

The reason for the linear roughness increase lies within the relaxation of layers during the first few hundred nm's, as misfit dislocations are continuously formed anew. Another contribution may lie within the low growth temperature. The kinetically limited adatom mobility has been shown to result in linearly increasing rms roughnesses, even without formation of new misfit dislocations, for example in Ge epitaxy.[125] The roughness values itself, however, are comparable to few µm thick SiGe buffers (with 30–50 at.% Ge)[146,151] and could be dealt with by *ex-situ* planarization techniques such as *chemical-mechanical planarization* (CMP).

Strong roughness variations between different stoichiometries, as in SiGe buffers,[146] are demonstrated in **Fig. 3.10**a-c. Thick layer (> 770 nm) with Sn contents between 5–12.5 at.% are shown, exhibiting similar undulation periodicities, but strongly varying roughnesses. As condensed in Fig. 3.10d, roughness strongly increases in high Sn content alloys by a combination of two effects. On one hand, higher Sn contents require a larger number of misfit dislocations for strain relaxation, leading to stronger surface undulations. On the other hand, low-Sn content layers were grown at higher temperatures (visible on the x-axis) which helps to overcome Schwoebel-Ehrlich

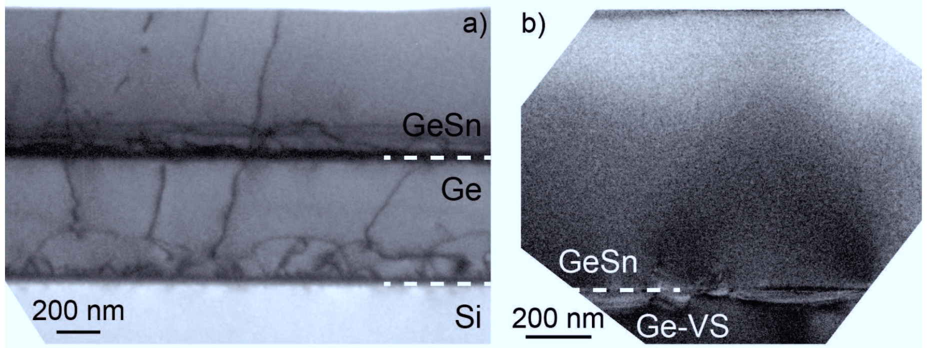

Figure 3.11 – a) TEM micrograph of a low-quality Ge buffer which induces a high threadings dislocation density in the GeSn alloy, while a high-quality Ge buffer allows epitaxy of high-quality GeSn.

barriers that are limiting surface diffusion across step edges during epitaxy.[152,153]

3.2.4 Defect evolution

As shown in the previous section, GeSn layers relax plastically during epitaxy via formation of misfit defects. For optoelectronic applications, these defects may act as sinks for excited carriers, offering non-radiative recombination paths,[134,135] while they act as scattering centers in nanoelectronic devices, reducing carrier mobility. As they play a critical role in later devices, their evolution and dependence for example on buffers is evaluated in the following section.

Growth on Ge buffers is strongly favored for minimizing lattice mismatch, as previously already discussed in section 2.2.1. Nevertheless, the buffer itself needs to be optimizied, as **Figure 3.11** proves. Here, TEM micrographs of thick (700–800 nm) GeSn alloys, grown on different Ge buffers are shown. In Figure 3.11a, the alloy is grown on a non-optimized, about 600 nm thick Ge buffer, featuring a high *threading dislocation* (TD) density. The GeSn layer on top features a very defective region in the bottom 150 nm, but also a number of threading dislocations. Partly, these line defects originate in the buffer and are not terminated at the GeSn/Ge interface. They are thus penetrating through the whole layer stack and are able to form midgap trap states in the GeSn.[154] Since they are present already in coherently grown layers,

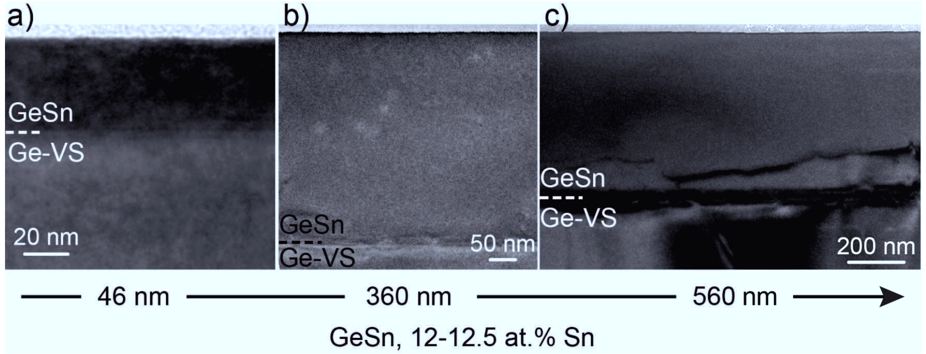

Figure 3.12 – TEM micrographs of a 46 nm coherently grown alloy a) and partially relaxed layers with 360 nm and 560 nm thickness [b) and c), respectively]. More defects are formed in thicker layers, still maintaining a high-quality top region.

it is important to reduce the TD density by optimizing Ge buffer growth.

Epitaxy of an 800 nm thick GeSn alloy on an optimized buffer is shown in Fig. 3.11b. Cyclic thermal annealing helped reducing the TD density in the Ge buffer down to $5 \times 10^6\,\mathrm{cm}^{-2}$ in Ge buffers externally grown by Jean-Michel Hartmann (CEA-LETI),[121] resulting in high-quality layers. A second clear complement lies within the defective region at the GeSn/Ge. In contrast to low-quality Ge buffers, defects also penetrate into the buffer, a distinct features, which will be taken up in the further course of this section.

Defect evolution under constant growth parameters, but increasing layer thickness is shown in **Fig. 3.12**. In a coherently grown alloy in Fig. 3.12a, no defects are visible in the TEM micrograph. For a partially relaxed alloy with 360 nm thickness in Fig. 3.12b, a rather dense misfit dislocation network is formed at the GeSn/Ge-VS interface, still leaving the top part of the layer pristine. Generation of defects continues in even thicker layers, as shown for a 560 nm thick sample in Fig. 3.12c. Here, several dislocation half-loops penetrate into the Ge-VS, but also create a defective region about 200 nm within GeSn. In even thicker layers, the defective region reaches even further into the *bulk* GeSn part, accompanied by an increased number of threading dislocations.

The different regions of a 410 nm thick $Ge_{0.875}Sn_{0.125}$ alloys are more closely depicted

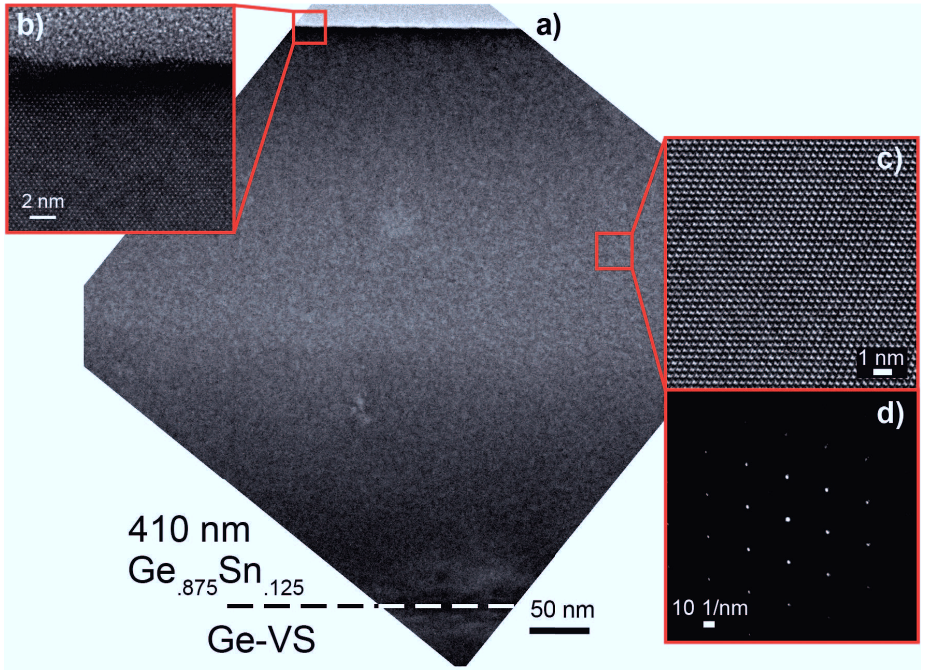

Figure 3.13 – TEM micrographs of 410 nm thick $Ge_{0.875}Sn_{0.125}$ layer: a) overview on the complete layer, b) surface region, c) high-resolution micrograph and d) diffraction image from the bulk region

in **Fig. 3.13**. The overview in 3.13a shows misfit dislocations confined at the GeSn/Ge-VS interface and no threading dislocations visible here. A region close to the top, shown in 3.13b, depicts a smooth sample surface without any sign of roughening from the low growth temperatures. In the bulk region of the sample, an exceptional crystalline quality is proved by the micrographs. The *brightfield* image in Fig. 3.13c offers atomic resolution and very regular atom arrangement. Furthermore, the *selected area electron diffraction* pattern shows the two-fold symmetry of the [110] zone axis, while distinct diffraction spots also indicate a high single-crystalline quality.

Figure 3.14a closely depicts the interface region of a different, but also hundreds of nm thick alloy. Several misfit dislocations, here marked by orange arrows, were

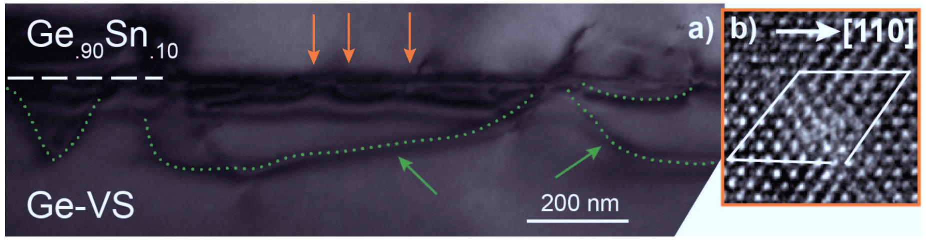

Figure 3.14 – a) TEM micrograph of a defective GeSn/Ge interface shows misfit dislocations and dislocation half-loops into the buffer. b) Close up of a pure edge dislocations.

formed during strain relaxation and form a dense network at the GeSn/Ge interface. High-resolution analysis, taken a few degrees off of the (220) zone axis, enabled identifying some of them as pure edge dislocations, as shown in Fig. 3.14b. Since only the component of the Burgers vector lying in the interfacial plane participates in strain relaxation, pure edge dislocations are most efficient in relaxing the in-plane compressive strain.[155]

A second important observation from Fig. 3.14a is the existence of dislocation half-loops in the Ge-VS. These line defects are not originally in the high-quality Ge buffer, as previously stated, but are formed during epitaxy. A mechanism in which the buffer participates in strain relaxation, reducing the dislocation density in the upper layers, is of course very beneficial for optoelectronic applications. One possible explanation for this behavior, which has previously been studied also in graded SiGe buffers[156,157] or III-V phosphides,[158] may be as following.

A pinned misfit dislocation formed at the GeSn/Ge interface may start acting similar as so-called Frank-Read sources,[159] which are able to generate additional dislocation loops. Once these loops reach the sample surface, both threading segments can move towards the wafer edge, while the lower part of the half-loop is pushed into the substrate. This mechanism might explain both dislocations in the substrate and only a small number of threading segments in the top part, but are also in accordance to other observations. On one hand, a certain length of the initial misfit dislocation is needed in the described model. If the initial dislocation density is too high, the Frank-Read mechanism energetically never starts operating, which explains the qualitatively different relaxation behavior in low-quality Ge buffers (c.f.

Fig. 3.11a on page 35). Second, this mechanism may also explain the strong increase in TD density in µm thick GeSn layers. As strain relaxation proceeds, more and more misfit dislocations are formed at the GeSn/Ge interface. Pinning of dislocations at their intersection is likely to occur and has been shown responsible for the large number of observed threading dislocations in SiGe buffers.[160] Similar pinning may be present also in our GeSn system, if the number of formed misfit dislocations surpasses a critical value. An expedient may then be given by grading the GeSn layer. In that case the dislocations are not solely located at the GeSn/Ge interface, but are spread across the graded region, which may help avoid pinning of threading segments even for thicker layers.[157] Indeed, a much better layer quality was found in case of step-graded GeSn layers.[161]

Nevertheless, this mechanism, originally developed for SiGe alloys, fully neglects the influence of vacancies on strain relaxation. In our case however, a large number of those is expected, both from the low growth temperature and the high lattice mismatch (i.e. up to 2 % mismatch for a 14 at.% Sn-containing alloy) between GeSn alloy and Ge substrate. Differences in their elasticities may promote injection of vacancies into the buffer, where they may also form dislocation loops responsible for the observed behavior. For a definite conclusion, detailed investigations of the involved types of defects will be necessary.

Besides the previously investigated misfit line defects and mentioned vacancies, several other types of point defects have been predicted in the GeSn system. Besides theoretical investigations of non-substitutional β-Sn defects,[162,163] mainly electronic properties of Sn-vacancy complexes were calculated.[164–166] Experimentally, the formation of midgap traps in GeSn from point and line defects was observed by *deep level transient spectroscopy*.[154,167] Direct observation of vacancies, however, for example by *positron annihilation spectroscopy* have so far only been pursued in bulk Ge material.[168]

In the following, defects are investigated by their electronic interaction in *electrochemical capacitance-voltage* (ECV) profiling. By this technique, a carrier concentration is derived from C-V measurements across the SCHOTTKY barrier between semiconductor and an electrolyte in contact.[169,170] Furthermore, a well-chosen electrolyte allows homogeneous etching of the semiconductor, hence periodic measurement-etch cycles allow depth-dependent profiles of the electrically active carrier concentration

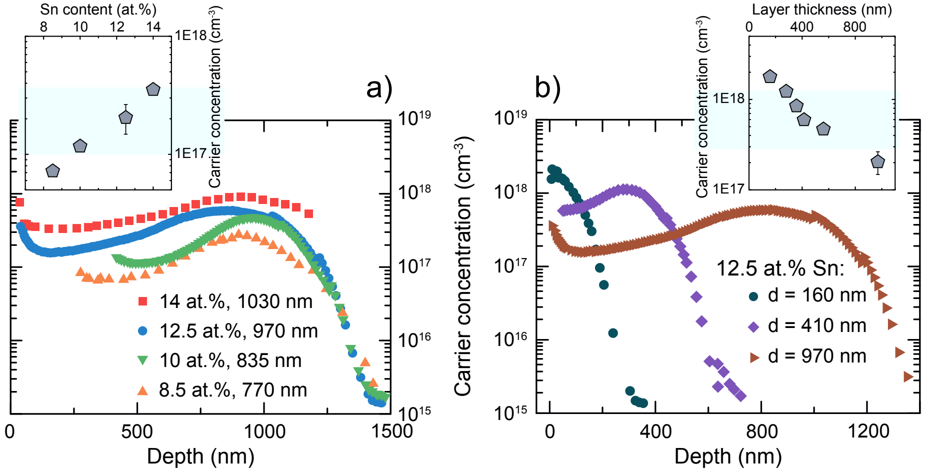

Figure 3.15 – a) p-type carrier concentration in thick GeSn alloys. Inset shows determined values close to the surface. b) Depth-resolved carriers for 12.5 at.% Sn series with varying thicknesses. Inset gives overview on concentration evolution.

throughout the sample. It shall be noted, however, that in narrow bandgap semiconductors, such as GeSn, the early onset of inversion region may impede a reliable value extraction. The absolute concentration values from ECV measurements have to be taken with a grain of salt, nonetheless it shall clearly indicate any trends.

ECV profiles of several thick GeSn alloys are shown in **Figure 3.15**a. For a better comparison, all data points were shifted, so their GeSn/Ge interfaces are on top of each other. All investigated samples show clear p-type behavior, consistent to unintentionally p-doped GeSn[171–173] and SiGeSn.[171,174] In these thick layers, different defect sources seem to contribute to the observed unintentional carrier concentrations. A clear increase in carrier concentration is observed surrounding the GeSn/Ge interface for elevated Sn incorporation, which is clearly linked to the higher amount of misfit dislocations, necessary for strain relaxation. In all layers, the carriers also clearly reach inside the buffer region, which coincides with the previously observed emission of defect half-loops into the substrate. Further away from the interface, the carrier concentration declines in each sample and may now be governed by vacancy point defects, typical for low-temperature epitaxy.[175–177] Only in these thick samples, a slight increase in carrier concentration is visible towards the surface. To rule out an artifact, e.g. from surface contamination, analysis of the top 50 nm are excluded in Fig. 3.15a. The still visible carrier concentration increase may be linked to additional defects injected from the surface during growth, when no more misfit defects can be formed at the interface as their density gets too high. Nonetheless, a clear trend of carrier reduction close to the surface is visible in the overview in the inset of Fig. 3.15a. It shall be noted, however, that the derived concentration in the 6×10^{16}–$5 \times 10^{17}\,\mathrm{cm}^{-3}$ may be off from the true values. For example, carrier concentrations determined by HALL measurements are about an order of magnitude smaller.[178] The reason for this deviation may lie in distortion of the ECV measured values due to the small bandgap material.

Similar ECV investigations are performed for a series with constant Sn incorporation, but differing thicknesses. Figure 3.15b shows a clear decline in carrier concentration for increasing layer thicknesses. Two possible explanations may be responsible for this behavior. On one hand, the distance between surface and the defective interface is larger leading to a stronger decrease in observed carrier concentration. On the other hand, on-going relaxation may reduce the amount of electrically active vacancies, as compressive strain in the layers is reduced. For a definite judgement, the exact type of defect needs to be observed, for vacancies for example possible by the previously mentioned *positron annihilation* technique.

3.3 Optical properties

After the previous section focussed on the structural and morphological properties of thick GeSn alloy, this section monitors their evolution in optical properties. To illustrate changes in bandgap and directness, two different optical measurement techniques were employed.

3.3.1 Measurement techniques

As a first technique, absorption measurements were performed in a *Bruker VERTEX 80V* Fourier Transform Infrared (FTIR) spectrometer system. Halogen and Globar SiC lamps are used to provide near- and mid-infrared light, respectively. The

Table 3.1 – Structural properties of thick GeSn series.

x_{Sn} (at.%)	thickness (nm)	strain (%)
8.5	770	-0.06
10	835	-0.23
12.5	970	-0.34
14	1030	-0.67

absorption spectra itself were acquired by a HgCdTe detector, which was cooled by liquid nitrogen. For maximum light collection, all samples were placed on top of a gold-coated, highly reflective sample holder, inside an integrating sphere.

The same measurement system further allows carrying out temperature-dependent photoluminescence (PL) measurements. In that case, samples were excited by a continuous-wave solid-state laser with an excitation wavelength of 532 nm and a maximum output power of about 100 mW. Photoluminescence, emitted by the samples, was then detected by a likewise nitrogen-cooled InSb detector with a detection range as low as 0.23 eV in step-scan mode. To further optimize light collection and reduce the influence of thermal radiation, an additional filter with ∼3 µm cutoff was positioned in front of the detector.

To allow a systematical, decoupled investigation of the independent influences of strain and Sn content, two different series were investigated. First, a series with nearly fully relaxed GeSn alloys with Sn incorporation in the range 8.5–14 at.% was examined. Beyond that, a series with a fixed Sn concentration of about 12.5 at.% was studied, with gradually increasing layer thickness and, thus, strain relaxation. An overview on the most important sample properties in both series are given in Tables 3.1 and 3.2.

3.3.2 Tuning Sn incorporation for bandgap engineering

The influence of Sn incorporation on light absorption is clearly visible in **Fig. 3.16**a. Reflection measurements of thick (>770 nm) layers are depicted in there, together with a spectrum of the underlying Ge-VS. The strong absorption edge of the latter one, slightly below 0.8 eV, can be attributed to the direct transition at the Γ-valley, which fits the literature value of 0.76 eV for the Ge direct gap (c.f. Table 2.1 from

Table 3.2 – Structural properties of GeSn thickness series for constant Sn incorporation.

thickness (nm)	x_{Sn}(at.%)	strain (%)
46	12	-1.65
215	12.5	-0.70
357	12.5	-0.55
414	12.5	-0.43
560	12.5	-0.40
705	12	-0.31
970	12.5	-0.34

page 7). In GeSn alloys, the position of the strong absorption edge, i.e. the Γ valley position, is strongly redshifted. For alloys with 8.5 at.% Sn it is located at around 0.50 eV, while for a 14 at.% alloy it is shifted as low as 0.37 eV. These values correspond to wavelengths of 2.46 µm and 3.39 µm, respectively. While in theory, modeling of the GeSn absorption spectra may yield more precise band structure parameters,[179,180] an exact determination of direct and indirect absorption edges in these samples are complicated by the presence of thickness fringes around the region of interest. Nonetheless, these results, as also expected from theory (c.f. section 2.1), demonstrate the high versatility of GeSn alloys. While in this thesis focus is placed on the formation of efficient group IV light emitters, the observed tunable absorption makes these alloys promising materials also for near- to mid-infrared absorption applications. Indeed, several GeSn-based photodiodes were reported in literature,[129,181–185] extending the spectral range of Ge detectors[7] further into the infrared. Also for applications such as electro-optical modulators, required in *opto-electronic integrated circuits* (OEIC), the material system is of interest.[186]

Besides light absorption, Sn incorporation also shows its impact on light emission. Figure 3.16b features normalized photoluminescence spectra, recorded at 4 K. Also in here, a clear redshift of PL peak position is observed at elevated Sn concentrations. Furthermore, a broadening of PL emission is observed in higher Sn content alloy, in case of the 14 at.% Sn sample (red) a second peak emerges. There are two possible explanations for this behavior. First, both peaks may be attributed to different transitions, from Γ to heavy or light hole (HH/LH). Indications for this were found

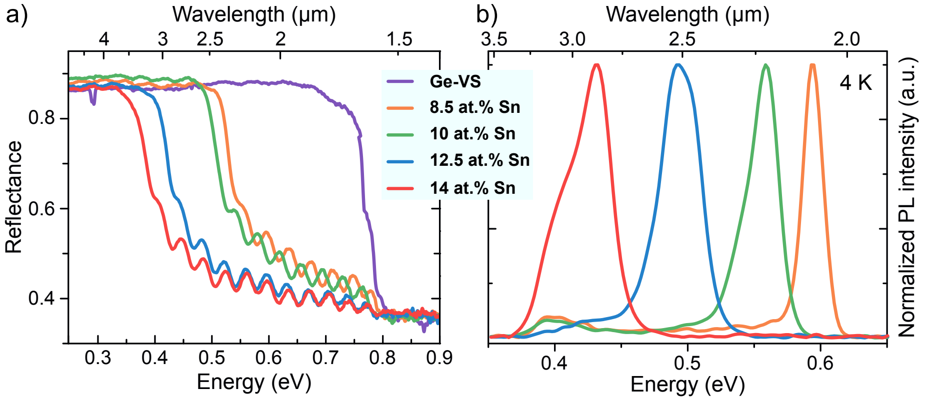

Figure 3.16 – Optical characterization of thick GeSn layers. Room temperature reflection measurements a) and normalized PL at cryogenic (4 K) temperatures b) indicate a clear bandgap redshift by increased Sn incorporation.

in power-dependent measurements in reference.[143] Another explanation may lie in the inhomogeneity of the layer. As discussed and shown previously in Fig. 3.5, thick layers feature an additional smaller Sn content region close to the interface. Only in cases of high Sn content alloys, both regions are *direct* enough to considerably contribute to PL emission, which may also explain the observed peak broadening only in high Sn content samples.

Temperature-dependent photoluminescence spectra were recorded for thick GeSn alloys to learn more about parameters needed for theoretical modeling of the alloys. As previously discussed, valley energies in GeSn can be calculated from the weighted individual element energies and additional bowing parameters (c.f. formula 2.1, page 7):

$$E^{\Lambda} = E^{\Lambda}_{\mathrm{Sn}}\; x + E^{\Lambda}_{\mathrm{Ge}}\; (1-x) - b^{\Lambda}_{\mathrm{GeSn}}\; (1-x)\; x \tag{3.5}$$

For the individual elements, temperature-dependence is included by applying appropriate Varshni parameters α and β, since T-dependent electron lattice interaction and dilatation of the lattice influence the bandgap following:[187]

$$E_{\mathrm{Ge/Sn}} = E_0 - \frac{\alpha T^2}{T+\beta}. \tag{3.6}$$

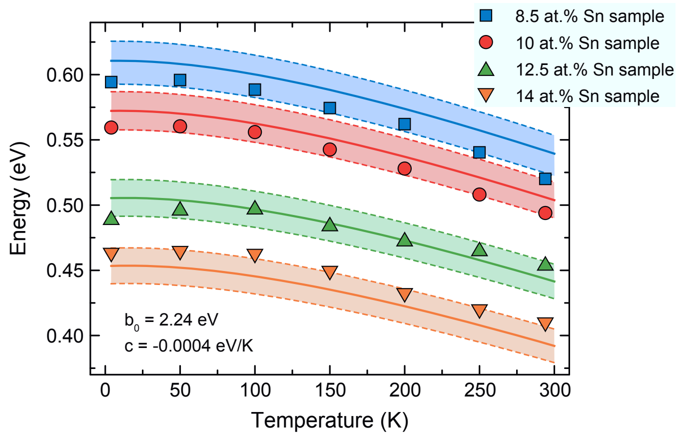

Figure 3.17 – Temperature-dependent direct bandgap energies from PL measurements are used for fitting temperature dependence of the GeSn bowing parameter b_{GeSn}. Data are well described by the fits (solid lines), including an uncertainty in Sn incorporation of ± 0.5 at.% (dashed lines).

While VARSHNI parameters are known at least for some valleys in Ge[188] and α-Sn,[189] no temperature-dependence of the bowing term b_{GeSn} is known. It can be included using a linear first order approximation

$$b_{\mathrm{GeSn}} = b_0 + c \cdot T. \tag{3.7}$$

Temperature-dependent Γ energies, obtained from the PL peak position E_{PL} by $E_\Gamma = E_{\mathrm{PL}} - k_B T/2$,[190] are plotted for a range of different alloys in **Fig. 3.17**.

Global fitting of all four temperature dependences allows extraction of a single pair of parameters b_0 and c for all four samples. Temperature trends are well described by the collective parametes $b_0 = 2.24\,\mathrm{eV}$ and $c = -4 \times 10^{-4}\,\mathrm{eV\,K^{-1}}$, indicated by the solid lines in Fig. 3.17. Certain deviations between fit and PL peaks can be solely explained by uncertainties in measurement of sample properties, ±0.5 at.% in Sn concentration and ±0.05 % strain. For each sample, the respective fits in Fig. 3.17 are also shown for maximum errors of measurements (that is +0.5 at.% Sn & and −0.05 % strain and vice versa) as dotted lines. Within these limits, the new parameters very well describe temperature behavior, and are used for band structure

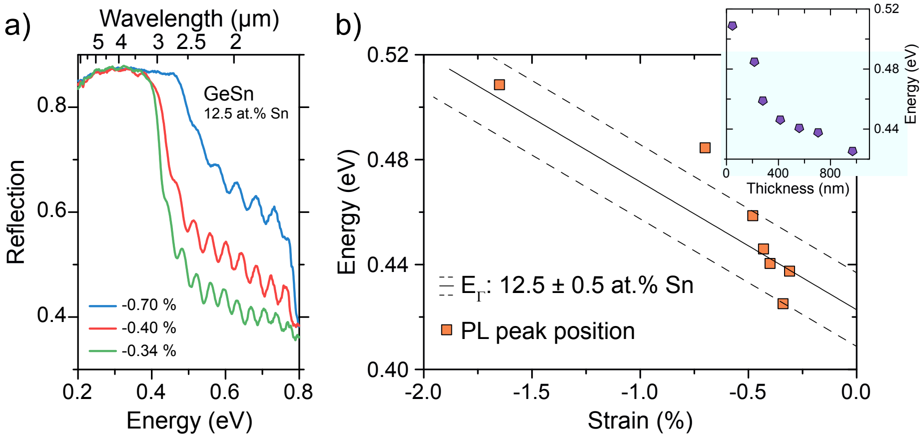

Figure 3.18 – a) Reflection measurements on a series with constant 12.5 at.% Sn, but varying compressive strain. b) Strain- (Inset: Thickness-) dependent direct bandgap positions, as determined from PL spectroscopy.

calculations in the following.

3.3.3 Influence of strain on layer properties

For investigating strain effects on the GeSn band structure, reflection and PL measurements were conducted on a series of samples with constant Sn incorporation, but varying residual strain (c.f. table 3.2, page 43). From reflection measurements of three samples, visible in **Fig. 3.18**a, the influence of compressive strain on the direct bandgap Γ-valley is clearly indicated. A distinct shift of the strong absorption edge from about 2.6 µm to 3.1 µm is observed, when the compressive strain relaxes from −0.70 % down to −0.34 %. A similar behavior, as expected from band structure theory (c.f. section 2.1), is also visible in PL measurements.

Figure 3.18b depicts direct bandgap positions, as determined from room temperature measurements, versus residual compressive strain. All samples besides one clearly match the theoretical predictions for (12.5 ± 0.5) at.% Sn alloys, as indicated by solid and dashed lines in Fig. 3.18b. Thickness dependence, as shown in the inset, illustrates a clear peak shift only in the first few hundred nm's of growth, which resembles the strain relaxation behavior, proving it to be cause for the PL

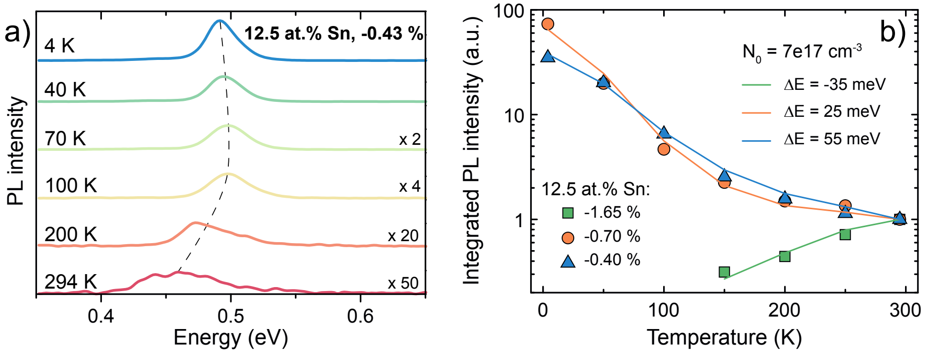

Figure 3.19 – a) Temperature dependent PL spectroscopy shows strongly increased light emission at cryogenic temperatures, originated in the direct bandgap character and a reduction of non-radiative recombinations. b) JDOS modeling of PL emission yields directnesses, comparable to band structure calculations (see Table 3.3), and proves an indirect-to-direct transition solely by strain relaxation.

redshift.

Further information on the layers' directness can be gained by temperature dependent investigation of light emission. In **Figure 3.19**a, changes in photoluminescence are demonstrated, when temperature ramping is performed from room temperature down to 4 K. Besides a VARSHNI-like shift in PL peak position, a distinct thermal quenching of PL intensity at room temperature is observed. The reason for this diminishing is a combination of two different effects. On one hand the fundamentally direct bandgap in this sample – the theoretically expected directness is about 65 meV – plays an important role. Due to the significantly smaller effective mass and, thus, density of states of Γ electrons, only a fraction of electrons is actually located at Γ. At least at room temperature, thermal broadening of the FERMI distribution leads to a non-negligible number of electrons at L. At cryogenic temperatures, however, electrons condense into the lowest occupiable energy states at Γ. Light emission is then enhanced, as a larger number of electrons is available for radiative direct energy transitions.

The second strong impact is raised by changes in non-radiative recombination time. Due to their relatively long diffusion length, optically excited electrons are able to reach the defective GeSn/Ge interface within their recombination time. The high number of misfit dislocations there, however, offer non-radiative recombination paths strongly deteriorating the efficiency of radiative transitions. At cryogenic temperatures, these non-radiative recombination centers are thermally not activated anymore, hence strongly increasing non-radiative recombination time.

Temperature dependent PL behavior of alloys can be modeled, employing a *joint-density-of-states* (JDOS) model. This model, as previously detailed discussed in reference [29] and the supplementary of reference [191], allows determination of the layers' directness within certain boundaries. The basic approach will be briefly explained in the following.

Emitted photoluminescence is directly related to the spontaneous photon emission rate $\bar{R}_{\mathrm{sp}}$ in the material and can thus be described via

$$\bar{R}_{\mathrm{sp}} \propto \sum_{i=\Gamma-\mathrm{HH/LH}} \int_{E_\Gamma}^{\infty} \rho_{\mathrm{3D}}\left(E, m_r^*, E_i\right) \cdot f_e\left(E'_{\mathrm{CB}}, \mu_e, T\right) \cdot f_h\left(E'_{\mathrm{VB}}, \mu_h, T\right)\, dE, \tag{3.8}$$

with the joint density of states $\rho_{\mathrm{3D}} \propto \left(m_r^*\right)^{3/2} \sqrt{E - E_{\mathrm{Gap}}}$, which shows the typical reduced mass m_r^* and energy E dependence in three dimensions. The FERMI distributions $f_{e/h}$ for electrons and holes are evaluated around primed energies

$$E'_{\mathrm{CB}} = E_\Gamma + \frac{m_r^*(\Gamma, \mathrm{HH/LH})}{m_\Gamma^*} \Big(E - \big(E_\Gamma - E_{\mathrm{HH/LH}}\big)\Big) \tag{3.9}$$

$$E'_{\mathrm{VB}} = E_{\mathrm{HH/LH}} + \frac{m_r^*(\Gamma, \mathrm{HH/LH})}{m_{HH/LH}^*} \Big(E - \big(E_\Gamma - E_{\mathrm{HH/LH}}\big)\Big) \tag{3.10}$$

for Γ → HH and Γ → LH transitions, respectively. The quasi-FERMI levels $\mu_{e/h}$, which arise due to the non-equilibrium occupation of bands from optical pumping, can be calculated from effective masses m^* (determined by 8-band k·p) and injected carrier concentration (from pumping power, in our case $N_0 = 7 \times 10^{17}\,\mathrm{cm}^{-3}$).

To eliminate the temperature dependent change in non-radiative recombination time, normalized PL of different samples were collectively fitted, assuming identical non-radiative recombination times. This is an important boundary for the model, as only samples with similar defect densities can be compared. Impact of temperature on PL intensity in those samples should then solely be caused by different occupation of Γ and L states, thus making the directness $E_L - E_\Gamma$ the only

Table 3.3 – Comparison of directness $E_L - E_\Gamma$, obtained from JDOS modeling and band structure calculations.

thickness (nm)	x_{Sn}(at.%)	strain (%)	directness from JDOS model (meV)	directness from band structure calculations (meV)
46	12	-1.65	-35	-40
215	12.5	-0.70	25	44
560	12.5	-0.40	55	69

fitting parameter.

Results of photoluminescence and respective JDOS modeling are shown in Fig. 3.19b. Excellent agreement is found between the normalized PL data and the modeled curves, for fully strained (green), as well as partially relaxed samples (blue and orange). The fully strained sample shows decreasing PL intensity at reduced temperatures. As previously discussed, the fundamental indirect bandgap in this samples leads to an occupation of L states. At cryogenic temperatures, L → Γ carrier transfer is suppressed, resulting in a diminishing of PL emission.

In partially relaxed samples, a qualitative difference in PL evolution is visible. Instead of a continuous PL decrease for temperature reduction, a steady emission increase is observed. An indirect-to-direct transition of the fundamental bandgap by strain relaxation can be accounted for the behavior difference in partial relaxed GeSn alloys. Further decrease of residual compressive strain from $-0.70\,\%$ to $-0.40\,\%$ and the accompanied increased directness leads to slight changes in temperature trend, which are reflected also in the JDOS fit. For highest directnesses, normalized PL intensity at 4 K is smaller than for intermediate strain values. In this case, a significant fraction of electrons populate the Γ-valley already at room temperature, thus the *relative* PL increase with temperature reduction will be less pronounced in this sample. Comparison of directness obtained from JDOS model and band structure calculations are illustrated in table 3.3. An adequate agreement between both methods is found. In particular, the expected indirect-to-direct transition, which is expected from theory for a value of about $-1.27\,\%$ (c.f. Fig. 3.7e on page 29), is reflected also in JDOS modeling. Thus, clear evidence of improved light emission properties by relaxation of GeSn alloys is found.

3.4 Summary

The previous section dealt with RPCVD growth of GeSn alloys at temperatures below 400 °C, down to 340 °C. Diverse techniques such as RBS, TEM and XRD were employed for structural investigation of grown alloys. Influence of stoichiometry and strain on band structure were investigated optically by carrying out temperature-dependent PL and reflection measurements. Those results were furthermore verified by band structure calculations. In the following, the most important results are summarized.

- Investigation of GeSn growth kinetics revealed two reliable mechanisms for tuning of Sn incorporation. Temperature reduction enables elevated Sn contents between 2.5–12 at.%, while symmetric tuning of digermane and tin tetrachloride flows allow changes in Sn concentration at a given temperature.

- Epitaxy of up to 1 µm thick GeSn layers with Sn incorporation as high as 14 at.% Sn was demonstrated. Layers undergo plastic strain relaxation by formation of misfit dislocation, which, however, can be confined at the interface for intermediate thicknesses of several hundreds of nm.

- Independent tuning of strain and Sn content allows engineering of the direct bandgap in the short-wave- to mid-infrared region up to 3.4 µm (0.37 eV), enabling versatile applications not only for emitters, but also for photodetectors or optical modulators.

- Temperature-dependent photoluminescence enabled improvements of the theoretical description of alloys, by determining temperature-dependence in bowing parameters.

- Overall, the suitability of GeSn alloys for light emitters was proven, demonstrating both requirements postulated in section 2.1: Growth of high-Sn content *and* strain relaxed alloys. Strong room temperature light emission was shown, while also an indirect-to-direct transition of alloys, induced by strain relaxation, promotes their use as active medium in efficient group IV light emitters.

4 Growth of SiGeSn ternary alloys

Contents

After epitaxy of binary GeSn alloys has been successfully developed in the previous chapter, this chapter deals with investigation of even more complex group IV ternary SiGeSn alloys. The low growth temperature (<425 °C) puts severe constraints on epitaxy, as even low-temperature growth of Si (using disilane) can only be performed down to 550 °C, before growth rates drop below 1 nm min^{-1}.[192] However, considerable Si incorporation is necessary for sufficient carrier confinement in GeSn/SiGeSn heterostructures. Despite these drawbacks, epitaxy of ternaries with Si and Sn concentrations up to 14 at.% has successfully been shown in literature.[130,193–198] There however, only marginal systematic investigations of growth kinetics or band engineering are performed.

Here, growth of SiGeSn ternaries is investigated, since they are ideal candidates for indirect and large-bandgap material in different types of heterostructures. Possible

applications range from heterostructure light emitters,[44,193,199] over heterostructure electro-optical modulators, to photodetectors[42] and to drain terminals in *tunneling field effect transistors* (TFETs).[99] Emphasis in this chapter is first placed on systematic inquiry of the influence of precursor gases, temperature and reactor pressure, analogue to the GeSn investigations in chapter 3. Tuning of band structure properties, for all compositions and strain individually, is performed again by optical techniques.
The presented results have in part been previously published under reference.[193]

4.1 Growth kinetics

In the previous chapter, an ideal partial pressure ratio $p_{\mathrm{Ge_2H_6}}/p_{\mathrm{SnCl_4}}$ of about 88 has been found for high quality epitaxy of GeSn layers. Starting from these parameters, the influence of disilane, temperature and pressure is investigated consecutively, leaving everything else constant.

4.1.1 Precursor flow dependencies

First, the impact of disilane flow on growth kinetics is investigated. As before for GeSn, these experiments were conducted at a growth temperature of 375 °C on Si wafers.
The changes in Si and Sn incorporation for a plain increase in disilane flow are shown in **Figure 4.1**a. While the Sn incorporation stays mainly constant at around 8.5 at.%, Si concentration is increased from 5 at.% to 11 at.%, when disilane flow is ramped up between 50–85 Pa. When compared to growth without any disilane, Sn incorporation in ternaries is slightly lifted by about 1 at.%. This well-known characteristic of SiGeSn ternaries[130,195] is linked to local strain compensation by the smaller-sized Si atoms, allowing a larger fraction of Sn atoms to be built-in the layer. It shall be noted that very high Si precursor flows (higher p_{Si} than p_{Ge}) are needed here to obtain a noticeable amount of Si incorporation, which is likely related to the small cracking efficiency of disilane at the low growth temperature. This additionally has the effect of deteriorating the layer properties. For disilane partial pressures above 68 Pa, no homogeneous atom incorporation is observed anymore, as

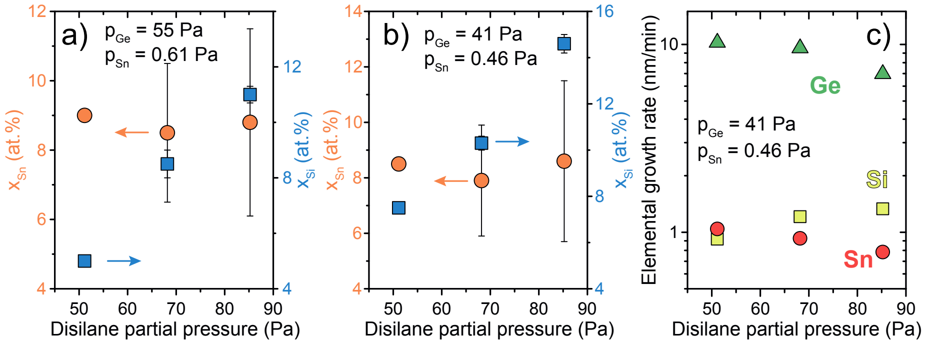

Figure 4.1 – a), b): Influence of disilane partial pressure on layer stoichiometry for two different $Ge_2H_6/SnCl_4$ flows at 375 °C. Increases in Si precursor flow are however accompanied by inhomogeneous elemental compositions. c) Elemental growth rates prove a surface poisoning by Si atoms, obstructing integration of Sn and Ge atoms.

proven by RBS measurements (see Fig. A.2 in the appendix).

Similar behavior is found for a disilane flow series, with smaller digermane and tin tetrachloride flows. As visible in Fig. 4.1b, Sn incorporation stays constant again, Si concentration linearly increases, while layer quality is degraded at higher disilane flows. To investigate the origin of this degradation, the elemental growth rates of the series from Fig. 4.1b are depicted in Fig. 4.1c. While growth rates for Si increase due to the higher Si mass flow, growth rates of both Sn and Ge diminish. The high amount of Si adatoms may obstruct lattice sites and limit adatom mobility, thus impedes the incorporation of Ge and Sn atoms.

For smallest disilane flows in Fig. 4.1a and b, however, different stoichiometric alloys are achievable. Both layers also show a high crystallinity, as proved further by small minimum channeling yields χ_{min} below 20 %. Keeping a constant disilane mass flow, while simultaneously adjusting only digermane and $SnCl_4$ flows (as for GeSn alloys) may be a valid solution for tuning stoichiometry at a given temperature.

To investigate this more systematically, a sample series was grown, keeping a constant disilane partial pressure of 68 Pa. The partial pressure ratio $p_{\text{Ge}_2\text{H}_6}/p_{\text{SnCl}_4} = 88$ was kept constant, only the absolute Ge and Sn precursor flows were varied simultaneously. **Figure 4.2**a shows the effect of Ge/Sn precursor adjustment on stoichiometry. While Sn content is fixed at around 8 at.%, a strong change in Si content

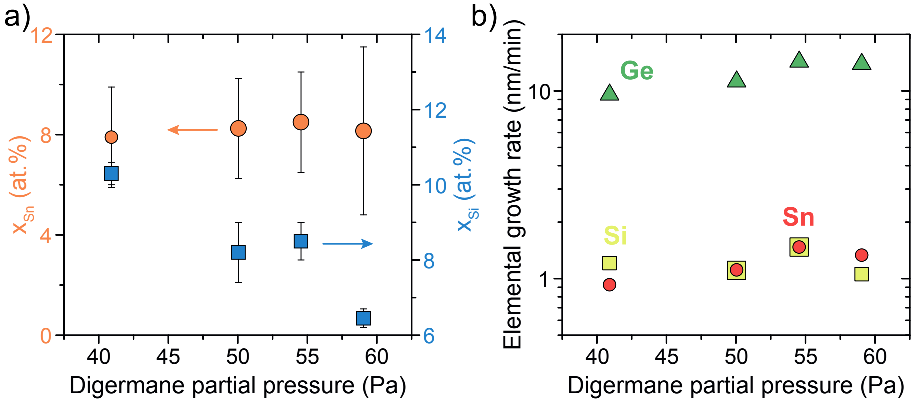

Figure 4.2 – a) Stoichiometry can be adjusted by coherent tuning of $Ge_2H_6/SnCl_4$ precursor flows, leaving disilane flow constant. c) Elemental growth rates show growth rate increases for Sn and Ge atoms and leveling of Si atoms, comparable to GeSn growth, making this approach useful for stoichiometry tuning at a given temperature.

between 6.5–10.3 at.% is visible. It must be noted that the overall layer quality is rather poor, which is due to the inflated amount of disilane flow in this series. The methodology itself, however, shall work also at smaller disilane mass flows. This is justified by the elemental growth rates in Figure 4.2b. Simultaneous increase in Ge/Sn precursor flows yield higher growth rates of both species, which was already shown in section 3.1.1 to produce high quality GeSn alloys with varying stoichiometries. As the Si growth rate maintains constant in this methodology, Si incorporation can reliably be adjusted by this method.

4.1.2 Reactor pressure dependence

A different parameter set, left out before, is the reactor pressure. Changes in pressure will have strong influence on growth kinetics, since it can accelerate precursor reactions in gas phase and thus have a strong impact on later film properties.[200] Although we always remain in a low-pressure regime around 60 mbar, the *particle* gas flow is kept constant in our reactor. Hence, pressure changes result in varying gas flow profiles above the wafer surface, which may have an influence on homogeneity. Further, also the shape of the *chemical reaction boundary layer* may change,

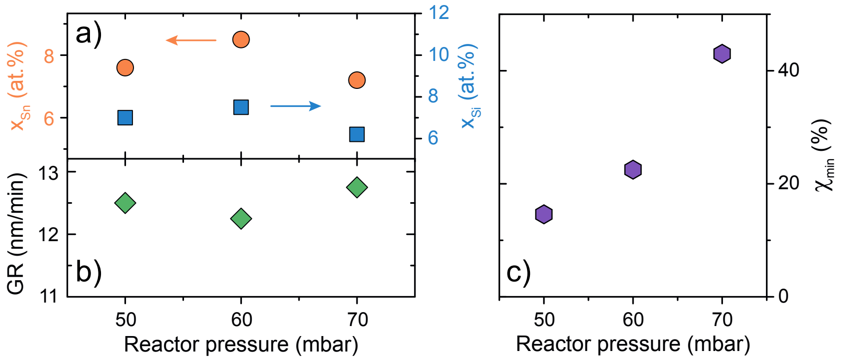

Figure 4.3 – Reactor pressure does not strongly influence composition a) or growth rates b) in this low-pressure regime. Layer quality, however, is increased for smaller pressures c), likely related to changes in chemistry in the chemical boundary layer close to the wafer surface

impacting the layer quality.

The effect of pressure changes on layer stoichiometry and growth rate are shown in **Fig. 4.3**a and b. Leaving the Ge/Sn/Si precursor partial pressure ratios constant, no clear influence on those layer composition and growth rate is observed. Admittedly, no drastic changes in gas phase reactions are expected in this low-pressure regime. A definite effect can be seen however on the crystalline quality, as characterized by the minimum channeling yield value. Decreasing χ_{min} values down to 15 % are observed, which may be related to changes in the *chemical reaction boundary layer* above the wafer surface. In this diffusion-limited region, sticking for a number N of precursor gas molecules on the surface is given by the HERTZ-KNUDSEN equation

$$\frac{\mathrm{d}N}{\mathrm{d}t} \propto \frac{p}{\sqrt{MT}}, \tag{4.1}$$

with reactor pressure p, molar mass of precursor molecule M and temperature T.[201] It is evident that clear changes in impinging rate are expected, although growth remains in a low pressure regime. This may influence surface reactions and thus impact changes in layer quality.

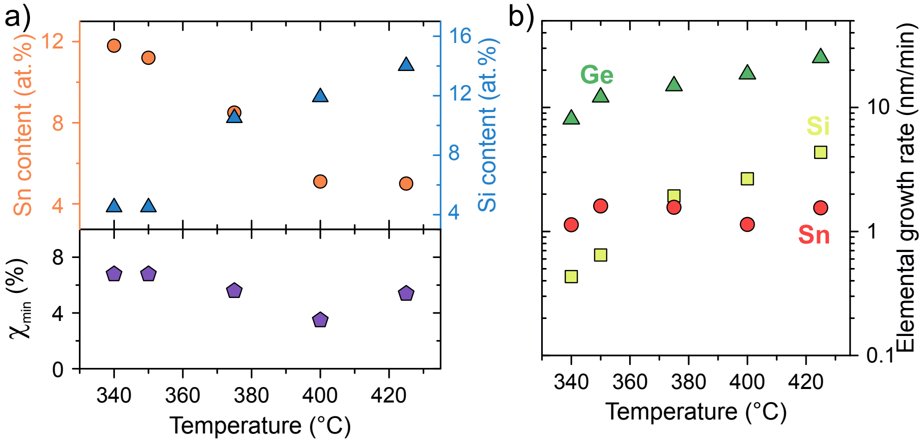

Figure 4.4 – a) Elevated Sn contents and decreased Si contents are observed when growth temperature is reduced, maintaining a high quality for all layers. b) Superlinear increase in elemental Si growth rate indicates kinetically limited Si incorporation from inefficient disilane cracking at low growth temperatures.

4.1.3 Temperature dependence

Similar as for GeSn, strong changes in growth kinetics can be expected from tuning the reactor temperature. A series of pseudomorphic SiGeSn layers is grown on top of Ge-VS for constant partial pressures of $p_{\mathrm{Ge/Si/Sn}} = 55/68/0.62\,\mathrm{Pa}$ in a temperature range from 340–425 °C.

The strong impact of temperature on layer stoichiometry is depicted in **Fig. 4.4**a. Temperature reduction to 340 °C is accompanied by a clear elevation of Sn content from about 5.0 at.% to 11.8 at.%. Similar to GeSn epitaxy, this behavior can be explained by a temperature-related diminishing of the Sn segregation length, permitting a higher number of Sn atoms in the layer at smaller temperatures.

For Si atoms, a clear reverse incorporation trend is observed. The reduction of incorporated Si atoms from 14.0 at.% to 4.5 at.% at smaller temperatures is clearly linked to the smaller cracking efficiency of the silicon precursor. The rather high binding energy of 3.20 eV of the Si–Si bond in disilane[128] impairs the formation of SiH_x radicals reducing the amount of incorporated Si atoms. This connection is further proved by the elemental growth rates in Fig. 4.4b. A super-linear Si growth rate increase proves the kinetical limitation of Si precursor cracking, while no change in Sn deposition speed is observed.

Nonetheless, incorporation of Si into the lattice at these reduced temperatures is astonishing in the first place, as the minimum growth temperature of Si from disilane is around 500–550 °C.[192] As the presence of chlorine accelerates the formation of radicals, additional chemical reaction paths going hand in hand with the $SnCl_4$ precursor may enhance Si incorporation at these small temperatures.

Regardless of growth temperatures, all layers exhibit excellent minimum channeling yields below about 7 %, proving layers in a broad stoichiometric range with up to 14 at.% Si or Sn, even without the formation of precipitates or a considerable number of atoms on interstitial sites.

4.1.4 Strain relaxation

Strain in the ternary is an important band structure parameter, just the same as for GeSn alloys. High Sn incorporation still results in compressively strained layers. In **Fig. 4.5**a, the RSM of a coherently grown layer with 4.5/11.8 at.% Si/Sn is shown. It possesses a smooth interface and surface, as visible from periodic oscillations – thickness fringes – around the SiGeSn peak.

In contrast to GeSn epitaxy, compressive strain is not necessarily always present in layers grown on Ge-VS. By adding a sufficient amount of Si atoms internal strain can be reduced, or even turned into tensile strain. This behavior is visible in an overview of several coherently grown samples in Fig. 4.5b. For small Si/high Sn contents, large compressive strain values of $-1.56\,\%$ are measured, similar to high Sn-content GeSn alloys. Increasing the number of Si atoms and/or reducing the Sn content minimizes the internal strain. For samples with a stoichiometry of 12/4 at.% Si/Sn, the layers are grown nearly lattice matched on the Ge-VS, which is comparable to a Si/Sn ratio of ~ 3.7, as found in reference.[202] For even higher Si contents, tensile strain is induced in the layer. In principle, this behavior acts as an additional degree of freedom in heterostructure designs. Decoupling of bandgap and lattice constant allows the design of stress-free heterostructures with a reduced number of interface defects. Different SiGeSn stoichiometries are also of interest for nanoelectronic applications, such as source/drain stressors. Inducing strain in the channel

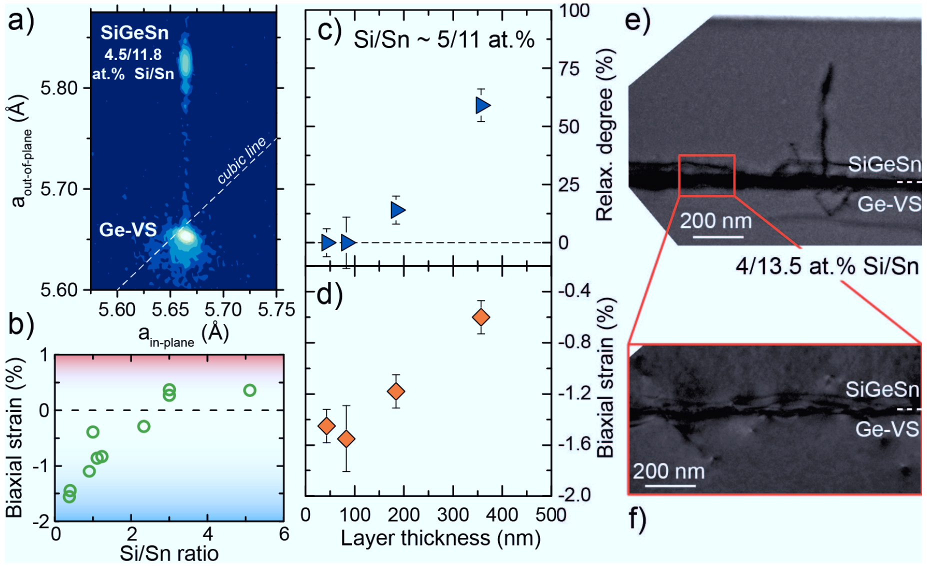

Figure 4.5 – a) *Reciprocal space map* of a coherently grown, compressively strained SiGeSn alloy. b) Strain in coherently grown SiGeSn alloys depends on Si/Sn ratio, allowing both tensile and compressively strained layers. c) & d) Relaxation degree and biaxial strain versus layer thickness, respectively, for a series with constant alloy composition show plastic strain relaxation when growth surpasses the critical thickness. e) & f) TEM micrographs shows formation of misfit dislocation close to the SiGeSn/Ge-VS interface and injection of dislocation half-loops into the Ge buffer layer.

of Si MOSFETs by replacing source and drain regions by SiGe (compressive) or SiC (tensile), is a nowadays commonly used technique for boosting carrier mobility.[203] SiGeSn can, depending on the exact stoichiometry, induce uniaxial compressive or tensile strain in the channel region of future Ge-based electronics, and thus could lead to enhanced device characteristics.[204,205]

Alike GeSn epitaxy, SiGeSn layers relax plastically, when grown beyond the critical thickness for strain relaxation. An overview on relaxation degree and residual strain is given for a series with ∼5/11 at.% Si/Sn in Fig. 4.5c and d, respectively. Coherent growth of thicker layers (up to nearly 100 nm) is possible, compared to previous investigated GeSn alloys in section 3.2.2, which is reasoned by the smaller mismatch stress to the Ge-VS.

Table 4.1 – Overview of the different ternary series, used for optical characterization.

Sample series	Si composition (at.%)	Sn composition (at.%)	thickness (nm)	strain (%)
Constant Sn	5.0	5.0	50	-0.39
	11.9	5.1	67	-0.29
	15.0	5.0	90	0.27
Constant Si	5.0	5.0	50	-0.39
	4.5	11.8	48	-1.56
	4.5	13.5	598	-0.59
Constant composition	4.5	11.2	43	-1.50
	5.5	10.5	184	-1.18
	4.5	11.5	357	-0.60
PL series	12.0	4.0	200	0.37
	6.0	11.0	195	-0.75
	4.0	13.0	243	-0.64

The microscopic origin of stress relieve is again very similar to GeSn alloys. As TEM micrographs in Fig. 4.5e&f prove, plastic relaxation occurs via formation of a large number of misfit dislocations and dislocation half loops, mainly confined at the bottom interface. As for GeSn, dislocation half-loops are pushed into the substrate, keeping defects away from the epilayers.

In conclusion, strain relaxation in ternaries strongly resembles that of GeSn. As growth has been shown successful, their versatility renders them interesting for several heterostructure applications. Origin of this multiplicity of applications lies within the potential of bandgap engineering. Bandgap tuning, individually by Si and Sn content is possible, and will be demonstrated in the upcoming section.

4.2 Bandgap engineering

As for GeSn alloys, bandgap engineering can be monitored by investigating absorption and emission properties of the grown layers. Different series of samples are measured for their optical properties in the following, an overview on their properties can be found in table 4.1.

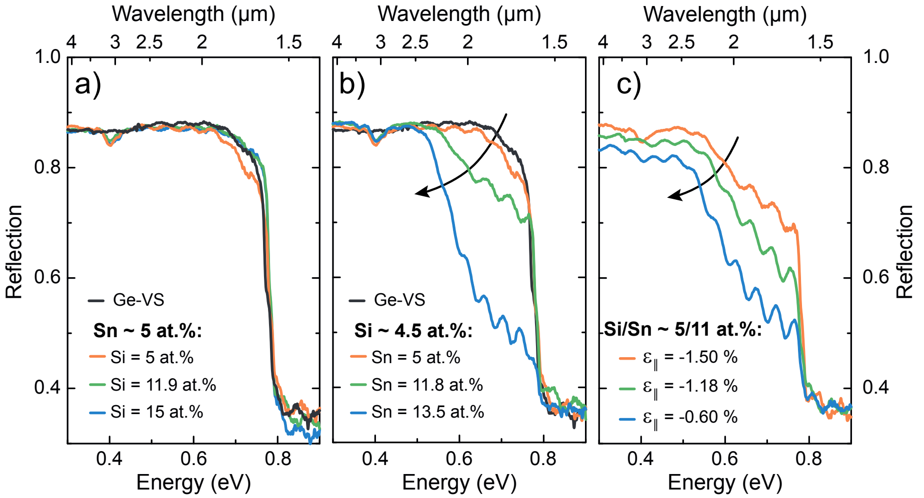

Figure 4.6 – Reflection spectra probing the strong absorption edge in different SiGeSn series. a): No clear effect of Si incorporation is seen, as the direct bandgap is shifted above the one of the Ge-VS. b) Sn increase leads to a distinct redshift of the Γ-valley, as does ongoing strain relaxation c).

4.2.1 Absorption measurements

To individually probe the influence of Si content, Sn content and residual strain on band structure, three sets of layers are investigated: i) for a constant Sn concentration of ∼5 at.% and varying Si contents; ii) for several Sn contents, but fixed Si concentration of ∼4.5 at.%; iii) fixed composition of 5/11 at.% Si/Sn, but different relaxation degrees (c.f. table 4.1). By tracing the position of the strong absorption edge, shifts of the direct bandgap at Γ can be investigated. **Figure 4.6**a shows reflection spectra of the first series with constant Sn content. All samples exhibit strong absorption beyond 0.8 eV, exactly as the Ge virtual substrate, which is given as comparison. It can thus be concluded that this absorption originates in the underlying Ge buffer, the value indeed matches the direct bandgap transition of Germanium.[42] While for the first sample with 5 at.% Si incorporation (orange curve) a slight absorption effect can be observed in a range slightly below 0.8 eV, all other samples seem to show exactly the same absorption behavior. Reason for the latter is the rather high amount of incorporated Si atoms. As discussed in band structure theory in section 2.1, Si atoms increase the direct bandgap at Γ, in this case well above the position of Ge. Thus, absorption from those SiGeSn alloys can not be observed in this configuration (grown on Ge), as it is always masked by strong absorption from the buffer itself.

In the second set of ternaries, however, a clear effect of Sn incorporation is made visible in figure 4.6b. For a small and constant Si content of about 4.5 at.%, a definite shift of the strong absorption edge is observed, when Sn content increases from 5 at.% to 11.8 at.%. The change in bandgap is composed not only of the increase in Sn content, but is even counteracted by the blueshift from increased compressive strain in the coherently grown samples. This needs to be taken into account especially for the third sample of the series. The 4.5/13 at.% Si/Sn sample (blue curve) is even further redshifted, compared to the 4.5/11.8 at.% Si/Sn sample (green curve), not only due to the increased Sn content, but also because of its partial strain relaxation.

To further decouple those two effects, reflection measurements on a thickness series (c.f. Fig. 4.5c/d from page 58) with constant composition of about 5/11 at.% Si/Sn were performed. Here, in Fig. 4.6c, even in a pseudomorphic layer, with $-1.50\,\%$ residual strain, clear absorption for energies smaller than 0.8 eV, thus not related to the Ge-VS, is observed. When strain relaxes in the ternaries, a further redshift of the absorption edge, and, accordingly, the Γ-valley energy is observed. From TAUC plots, a drop of the direct bandgap from 0.62 eV to 0.57 eV is determined, when compressive strain relaxes from $-1.50\,\%$ to $-0.60\,\%$ (see Fig. A.3 in the appendix). Thus, all expected influences of Si and Sn content, as well as strain relaxation, were observed from changes in absorption behavior. Impact of stoichiometry should also be able to be made visible in light emission spectra, as investigated in the following subsection.

4.2.2 Light Emission

Figure 4.7a shows room temperature photoluminescence spectra of three different ternaries, an overview on their properties is given in table 4.1. As discussed already in reference,[29] PL peak shifts can be attributed to changes in both layer composition and strain state. While a Si-rich ternary (orange) features light emission at around

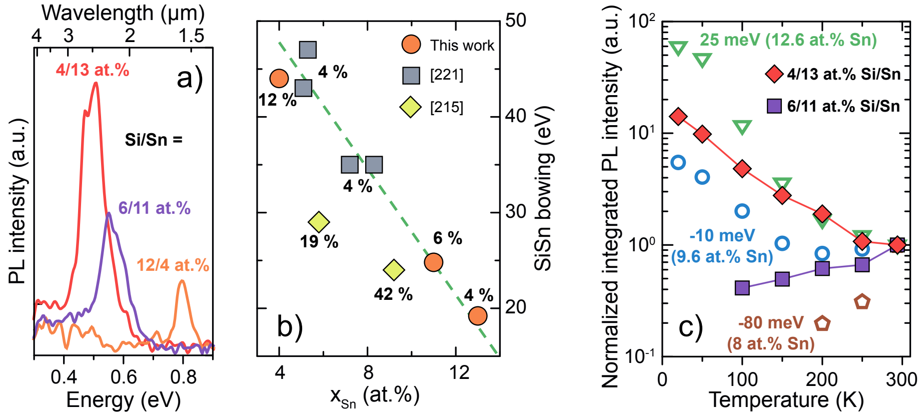

Figure 4.7 – a) Room temperature PL spectra of three SiGeSn samples. b) Determination of b_{SiSn}, using equation (4.2) and the peak positions of a), yield a composition dependence, which conforms literature data. c) Comparison of temperature dependent PL of ternaries and GeSn binaries, yields SiGeSn at the edge of the indirect-to-direct transition.

0.8 eV, emission is shifted beyond 0.55 eV (6/11 at.% Si/Sn, violet curve), and down to 0.49 eV for a Sn-rich ternary (4/13 at.% Si/Sn, red curve). For the Si-rich alloy, emission corresponds to a wavelength of 1.55 µm, while the Sn-rich alloy emits at about 2.53 µm. SiGeSn is thus able to extend the usable wavelength range of Sn-based alloys from mid-IR (GeSn) down to the lower end of the short-wavelength IR regime.

PL emission can further be utilized to fit band structure calculations to experimental data. As already discussed in the background chapter, valley energies can be determined by interpolating values from the single elemens (Si, Ge & Sn) and adding appropriate bowing terms, as in

$$E^{\Gamma} = E^{\Gamma}_{\mathrm{Si}}\ x + E^{\Gamma}_{\mathrm{Sn}}\ y + E^{\Gamma}_{\mathrm{Ge}}\ z - b^{\Gamma}_{\mathrm{SiGe}}\ x\ z - b^{\Gamma}_{\mathrm{GeSn}}\ y\ z - b^{\Gamma}_{\mathrm{SiSn}}\ x\ y \tag{4.2}$$

for the Γ-valley. While values for the different elements can be very well determined by experiment or band structure calculations, larger uncertainties are present for the exact bowing values. As they can be determined from binary alloys,[50] several works have been performed investigating SiGe bowing parameters,[206,207] yielding a value of

b_{SiGe} ~0.2 eV for Γ.[207] Similar works have been performed for GeSn bowing, where values in a range of 2.1–2.8 eV were found.[61,207–209] The strong difference between b_{SiGe} and b_{GeSn} may be explained by their underlying physical origins. Bowing arises from several microscopic effects, such as volume deformation of the unit cell, as well as charge exchange between different atom species and changing bond lengths.[210] Indeed, it was found that bowing parameters in different alloys scale by the product of their electronegativity and atom size mismatch.[210] This is sufficient to explain the differences between GeSn and SiGe bowing terms.

A much larger uncertainty is given for the SiSn bowing term, which arises from the fact that no optical measurements on those binaries are available. The small solubility of Sn in Si (c.f. Fig. 2.3a on page 11) hinders high quality grown layers so far, although considerable works have been performed in the field.[116,118,211–214] Values for b_{SiSn} have, thus, always been obtained indirectly from SiGeSn ternaries, explaining the huge spread in literature values between 29 eV,[215] 13.2 eV,[216] to even negative values of −21 eV.[217] Theoretical calculations yield a value of 3.9 eV, somewhere in between the experimental range.[42]

For further clarification, we investigated bowing from the PL data in Fig. 4.7a. Direct PL transitions were assumed to calculate the Γ-valley energy from PL emission. Fitting Γ energies by equation (4.2) (with additional strain correction) only by variation of b_{SiSn}, yielded an interesting result, depicted in Fig. 4.7b. There, b_{SiSn} is plotted versus Sn concentration in the ternary, while Si contents are added as numbers in the graph. Not a single SiSn bowing parameters is satisfactory for all three samples (orange symbols), the fitted values scatter between 19 eV for the Sn rich and 44 eV for the Si rich ternary. From these findings it can be concluded that a single SiSn bowing parameter can not be valid over the whole compositional range. It shall be either made composition-dependent, or, alternatively, higher-order terms (cubic in Si/Ge/Sn content) may be added to equation (4.2). This phenomenon is, however, not limited to the SiGeSn system, similar behavior was found also for nitride ternaries InGaN[218] and GaSbN.[219] For the SiGeSn system, this phenomenon may be related to an ordering effect of Si atoms, which was observed by *atom probe tomography* (APT) analysis in high Sn content ternaries.[220]

Figure 4.7b further features additional data, extracted from references[215] and.[221] For a small and constant Si content, a clear linear decrease of b_{SiSn} is found. It can be described by the linear relation

$$b_{\mathrm{SiSn}} = 61\,\mathrm{eV} - 3.3\,\mathrm{eV/at.\%} \cdot x_{\mathrm{Sn}}, \tag{4.3}$$

which was obtained by linear fitting of the 4 at.% Si data points. On the other hand, no clear conclusion can be drawn from high Si-content ternaries in Fig. 4.7b, although its influence seems to be less pronounced compared to Sn content.

The emission boost in Fig. 4.7a, as already discussed in reference,[29] is caused by the higher directness of Sn-rich alloys, allowing more efficient radiative transitions. Similar to GeSn alloys, directness of the ternaries can be determined from a JDOS model (c.f. section 3.3.3). However, as simultaneous fitting of multiple samples is required, and full-range temperature dependence is only available for the Sn-rich alloy, only rough estimations can be given here. Figure 4.7c shows the normalized integrated PL intensities for the Sn-rich (red) and the medium (violet) sample. For comparison, three different *GeSn* samples are given (open symbols), on which JDOS modeling already lead to good agreement to band structure theory for their directness values.[18] Qualitatively, the Sn-rich ternary shows similar temperature dependent behavior as the GeSn samples. A continuous PL increase at temperature lowering can be observed, attributed to both reduction of non-radiative recombination paths and condensation of carriers in the direct Γ-valley for appropriate band alignments. Its trend lies in between two GeSn samples, which directnesses previously have been determined to 25 meV and −10 meV, respectively. Thus, this sample may just about exhibit a fundamentally direct bandgap. Indeed the JDOS model predicts a (rough) value of 10 meV for the directness.[29] Band structure calculations, employing a SiSn bowing term of 19.2 eV, apparently overestimate the directness, as a directness of 40 meV is yielded.

The violet sample in Fig. 4.7c shows a clear indirect bandgap behavior, as its PL emission clearly diminishes with temperature reduction. Nonetheless, there are good prospects to fabricate also ternary-based light emitters, as given by the demonstrated results.

4.3 Summary

This chapter is concerned with low temperature growth ($\leq$425 °C) of SiGeSn ternary alloys. Structural and optical investigations revealed high quality layers, similar as for binary GeSn alloys. Below, the central outcomes are briefly recapitulated.

- Epitaxy of SiGeSn ternaries was demonstrated, yielding a broad composition range for both, Si and Sn contents, each up to 14 at.% by tuning precursor flows and growth temperature. The rather high Si incorporation substantiates their use as cladding layers or barriers in heterostructure light emitters, as postulated in section 2.1.
- Bandgap engineering was proven possible by means of reflection and photoluminescence spectroscopy. Direct bandgaps from 0.49 eV (2.53 µm) up to above bulk Ge values, 0.8 eV (1.55 µm), were found, enabling a broad range of applications such as photodetectors or optical modulators. Indications for fundamentally direct bandgap ternaries were found, which may allow also active components such as light emitters.
- Photoluminescence spectra yielded a Sn composition dependence in the SiSn optical bowing parameter, which may help resolve uncertainties present today in that parameter. Thus, it allows more reliable band structure and alignment calculations, which are needed for designing efficient GeSn/SiGeSn heterostructures.

5 Advanced group IV heterostructures for light emitters

Contents

As discussed in the introduction, the creation of a light source for *opto-electronic integrated circuits* (OEICs) is not a straight-forward task. Heterogeneous integration of III-V materials on Si showed indeed promising results,[13–15] but using a monolithical group IV approach allows leveraging Si photonics by exploiting the mature CMOS technology. As Sn-based alloys have been shown prime candidates for group IV lasers,[222] lots of research on electrical-driven light emitters was performed, yielding first GeSn homojunction diodes.[223–225] More complex designs applied Ge for simple heterostructures[226–228] or even quantum well structures.[225,229] In all cases, however, group IV light emitters were limited in a regime close to the indirect-to-direct transition of the fundamental bandgap.

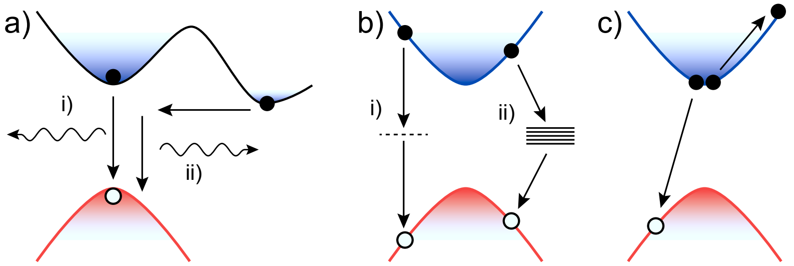

Figure 5.1 – a) Radiative recombination in i) direct and ii) indirect semiconductors. b) Non-radiative recombination via i) trap and ii) surface states. c) Auger recombination, in which the released recombination energy excites a free carrier.

The demonstrated results from previous chapters, direct bandgap GeSn alloys and indirect SiGeSn ternaries, allow the fabrication of more complex and efficient heterostructures. After a short recapitulation on heterostructure light emitters, epitaxy of basic GeSn homojunction diodes is demonstrated. Moving on towards heterostructures, different types of *multi quantum well* (MQW) LEDs employing Ge and SiGeSn barriers are fabricated and compared for their light emission. In the end, all pieces are put together by combining direct bandgap GeSn with SiGeSn claddings to form truly efficient group IV double heterostructures and MQWs. Parts of the shown results have been previously published in references.[193,199,225,230]

5.1 Heterostructure LED theory

Light emission in LEDs relies on radiative recombination of electron-hole pairs in a semiconducting material. Although recombination is the preferred process, several other non-radiative recombination paths exist in a semiconductor, which can only hardly be suppressed. **Figure 5.1** depicts several possible recombination processes, showing interband recombination in a). Radiative recombination in a direct bandgap semiconductor, as shown for i), requires only the availability of an electron-hole pair and is thus a very efficient process. Recombination rate R is proportional to the availability of electrons and holes and can be described (for non-degenerately doped semiconductors)[231] as

$$R = Bnp. \tag{5.1}$$

This so-called *bimolecular rate equation* features electron and hole concentrations n and p. These total concentrations are the sum of an equilibrium concentration n_0/p_0, present in the material, and a number of excess carriers $\Delta n/\Delta p$, which are excited either by electrical or optical injection. The rate equation further features a proportionality constant B, which is called the *bimolecular recombination coefficient.*

In indirect bandgap semiconductors, where the conduction band minimum is not located above the valence band maximum, an additional phonon is required for the transition, see ii) in Fig. 5.1a. Since massless photons can only carry a small momentum, a phonon is required for fulfilling conservation of momentum, when an electron is scattered into the center of the BRILLOUIN zone before recombination with a hole. Thus, radiative recombination in an indirect bandgap semiconductor is a much less efficient recombination path. This is reflected in the *recombination coefficient* B, which amounts to $2 \times 10^{-10}\,\mathrm{cm^3\,s^{-1}}$ for direct GaAs and $2.8 \times 10^{-13}\,\mathrm{cm^3\,s^{-1}}$ for indirect Ge[231] at room temperature. From these values, a radiative recombination time can be calculated, which is given for small carrier injections[231] by

$$\tau_\mathrm{r} = \frac{1}{B\left(n_0 + p_0\right)}. \tag{5.2}$$

Different recombination processes, related to impurities, are shown in Fig. 5.1b. Structural defects, such as misfit dislocations or vacancies, may give rise to discrete energy levels inside the forbidden energy gap. Transitions, involving those levels, can be understood as annihilation of an electron and a hole, which are both excited into a trap energy state. Non-radiative recombination time τ_nr for this so-called SHOCKLEY-READ-HALL process, can be calculated for an intrinsic material with equal electron and hole capture rates as[231,232]

$$\tau_\mathrm{nr} = \tau_0 \left[1 + \cosh\left(\frac{E_T - E_{F,i}}{k_B T}\right)\right], \tag{5.3}$$

where E_T describes the position of the trap energy level, $E_{F,i}$ of the intrinsic FERMI level. The (minority) carrier lifetime $\tau_0 = \left(N_T \nu_0 \sigma_0\right)^{-1}$ can be calculated from a known trap density N_T, carrier velocity and capture cross section ν_0 and σ_0, respectively. From equation (5.3) it is visible that non-radiative recombination is at its peak for energy levels at midgap, thus $E_T \approx E_{F,i}$. Further, it is reduced at temperature lowering, which is well-known from previous temperature dependent PL investigations on GeSn and SiGeSn alloys.

A different non-radiative recombination type, marked as ii) in Fig. 5.1b, is surface recombination. Dangling bonds, surface reconstruction or, more general, the broken periodicity of the crystal lattice at the layer's surface give rise to a continuum of states inside the bandgap, which also allows non-radiative recombination paths. Though passivation partly helps to reduce surface recombination,[231] growth schemes for efficient structures should electronically keep carriers away from surfaces. Same holds true for dealing with defective interfaces, e.g. from misfit dislocations, as they cannot be avoided during growth of strain-relaxed Sn-based alloys.

Besides the previously mentioned recombination processes, Figure 5.1c also depicts a higher-order process, that is AUGER recombination. In this process, the energy released from electron-hole recombination is transferred onto a second free electron or hole, which is excited upper/deeper into the conduction/valence band. As these excited carriers are able to relax via phonon emission, the energy is also not available for light emission. In contrast to radiative recombination, described by equation (5.1), the AUGER process requires an additional carrier to be excited. Its recombination rate thus increases as the cube of carrier concentration and therefore plays a role only for high excitation, for example in semiconductor lasers.

In the end, it is impossible to completely suppress non-radiative recombination paths. In fabricated devices there will always be a competition between different recombination processes. Giving a measure on LED performance, the internal quantum efficiency η_{int} can be expressed by radiative and non-radiative recombination times as

$$\eta_{\mathrm{int}} = \frac{\tau_{\mathrm{nr}}}{\tau_{\mathrm{r}} + \tau_{\mathrm{nr}}}. \tag{5.4}$$

From this relation, two different strategies arise to form efficient light emitters, either minimize radiative recombination time, and/or increase the non-radiative lifetime. In the following, both approaches shall briefly be discussed.

In light emitting devices, both electrons and holes are injected electrically into an active region via a forward-biased p-n junction. The respective band alignment for a simple homojunction diode, i.e. from a single material, is given in **Figure 5.2**a.

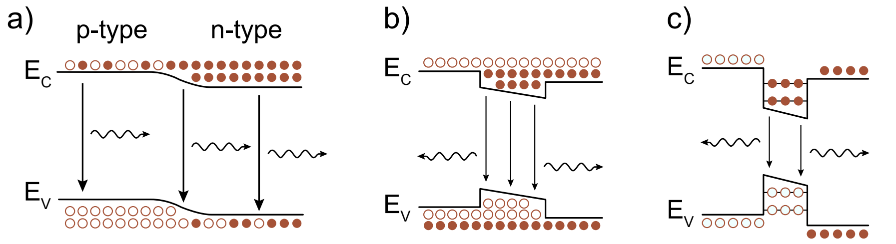

Figure 5.2 – Light emission in different LED structures: From a homojunction diode a), a double heterostructure (DHS) b) and a quantum well design c).

Forward-biasing reduces the junction barrier, allowing electrons and holes to diffuse into the former depletion region and into a region of opposite conductivity type, where they recombine. As the diffusion length of minority carriers is relatively long, typically in the order of several µm,[231] the region of recombination is rather large, which is not ideal for efficient emission.

On the other hand, carriers can be confined within an active region by means of larger bandgap cladding layers, in so-called heterojunction structures. In the *double heterostructure* (DHS) design, depicted in Fig. 5.2b, the effective recombination region is given by the active layer thickness, typically in the order of a few hundred nanometer's, rather than by the diffusion length of injected carriers. Recalling equation (5.1), a higher carrier concentration in the active region yields inevitably higher recombination rates, thus reduces radiative recombination time. Therefore, light emission will always benefit from heterostructures, as long as their thickness is below the carrier's diffusion length. One slight problem in these designs is the existence of a p-n charged interlayer at the heterointerface, increasing the resistance for carrier transport. It can be, however, circumvented by compositional grading the interface region, instead of having abrupt profiles.[231]

From equation (5.1), it is visible that also slight doping of the active device region is beneficial, as it increases the number of available carriers for recombination. Certainly, the possible window is rather small, as an increased number of dopants also gives rise to stronger impurity scattering and *free carrier absorption*.[231]

Efficiency can be even more increased by implementing two-dimensional quantum wells (QWs) as active regions, as shown in Fig. 5.2c. The even smaller layer thickness, compared to DHSs, allows reaching similar active carrier concentrations by smaller injected currents, further increasing radiative efficiency. To avoid a carrier overflow out of the active region, it is beneficial to increase the number of wells, i.e. move towards multi quantum well (MQW) structures. In addition, the density of states is changed in two-dimensional structures, as quantized states are formed in the well region due to quantum confinement. Looking even further, this effect enables an easier population inversion, which will become important in future heterostructure lasers.[233,234]

The second strategy for increasing device efficiency is elevation of the non-radiative recombination time τ_{nr}. Native defects can never be averted in epitaxial layers and will always be present just from thermodynamical considerations. One possible way is to confine defects far away from the active region, since the formation of misfit dislocations is necessary for strain relaxation. As will be later discussed in section 5.3.3, the use of buffer layers can keep defects from the recombination region, and thus strongly enhance light emission.

5.2 Homojunction GeSn diodes

The first investigated LED designs are homojunction diodes. Several LEDs with differing Sn contents between 8–12.5 at.% were epitaxially grown by tuning growth temperature between 350 °C and 375 °C. To avoid damage from ion implantation, doped layers for efficient carrier injection into the diode were obtained by in-situ doping during growth. Both n-type[235,236] and p-type[87,237] doping of GeSn have previously already been shown to yield high-quality layers. Even very high dopant concentrations in the order of $1 \times 10^{19}\,\mathrm{cm}^{-3}$ have been achieved by demonstration of *negative differential resistance* (NDR) in GeSn p-i-n homojunction diodes.[238]

The grown layer structure is visible in **Figure 5.3**a. A TEM micrograph of the 500 nm GeSn layer (8 at.%) proves high quality layers, with misfit defects only close to Ge-VS interface. In the overlaid SIMS line scan, different regions can be distinguished, otherwise invisible in the micrograph. The bottom 150 nm are p-type doped for injection of holes, as boron is clearly visible in the SIMS signal. The carrier concentration was determined to about $4 \times 10^{18}\,\mathrm{cm}^{-3}$ by ECV measurements, since SIMS without additional standards can only offer arbitrary intensity signals.

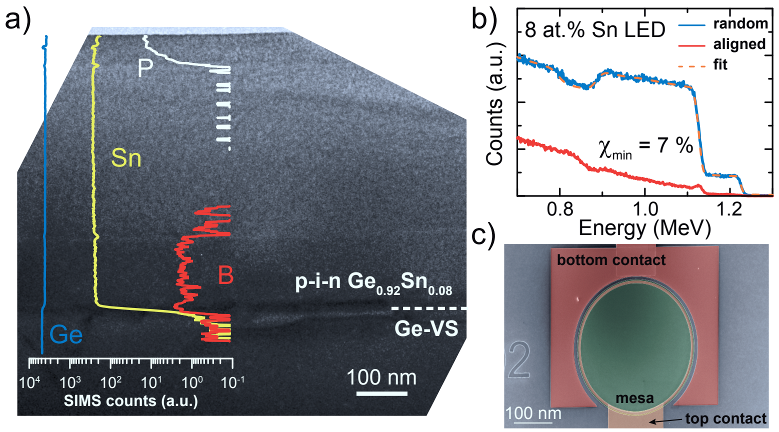

Figure 5.3 – a) TEM micrograph of the complete Ge$_{0.915}$Sn$_{0.085}$ homojunction diode, p-i-n regions are distinguishable from the overlaid SIMS profile. b) RBS random (with respective spectrum fit) and channeling aligned spectra prove a high crystalline quality of the structure. c) SEM micrograph of a fabricated LED structure shows mesa, as well as top and bottom contacts.

On top, a roughly 200 nm thick intrinsic layer was grown as active layer for carrier recombination, still comprising a p-type carrier concentration of about $3 \times 10^{17}\,\mathrm{cm}^{-3}$. The structure is completed by an about 50 nm thick n-doped ($\sim 8 \times 10^{19}\,\mathrm{cm}^{-3}$) region, acting as electron injection layer.

As visible by the SIMS signal, no strong influence of dopants on Sn incorporation is observed, as the Sn content remains reasonably constant throughout the complete layer stack. This observation is in line with literature, where an influence is expected only from strain compensation of the smaller-sized boron and phosphorus atoms.[87,88,239] This, of course, holds only true as long as rigorous changes in surface chemistry, for example from surface poisoning, are avoided.[87]

However, a very thin Sn-depleted interlayer between the intrinsic and both doped regions is visible in the SIMS linescan from slight dips in the Sn signal. Their appearance is linked to growth interruptions during epitaxy, which were necessary for changing precursor flows. As a few nm thin Ge interlayer is also always visible when GeSn is grown on bulk Si, this effect may be linked to a larger growth delay of Sn, compared to Ge. Decomposition and incorporation of Sn into the grown layer may require additional chemical steps compared to Ge, explaining the thin interlayer. Electronically, however, it may cause a slight band bending, and thus additional resistance for carriers, which is why growth interruptions should be avoided, in more complex structures.

RBS spectra, shown in Fig. 5.3b, were performed aligned in [100] crystal channeling and random directions. The small minimum yield value of about 7 % verifies a high layer quality, in-situ doping apparently does not degrade layer quality.

To investigate electroluminescence (EL) of the layers, LED structures were fabricated using solely Si-CMOS compatible processing technology.[240] The basic process flow followed the description from reference.[225] Circular mesa structures were defined by means of optical lithography and subsequent Cl_2/Ar *reactive ion etching* (RIE). Mesa passivation was performed by a two-step approach. First, a highly conformal 10 nm thick Al_2O_3 or HfO_2 layer was grown by *atomic layer deposition* (ALD), followed by a 150 nm thick PECVD SiO_2 layer. Contact windows were defined afterwards, again by optical lithography and subsequent CHF_3 etching. Ten nanometers of Ni were deposited in a sputter tool, before forming gas (N_2:H_2) annealing at 325 °C for 10 s yields low-resistive NiGeSn contacts.[241] At the end, an additional Al contact layer was sputter deposited, to allow contacting of single diodes via wire bonding. A 30° tilted *scanning electron microscope* (SEM) image shows a finished device with 300 µm diameter in Fig. 5.3c. In this false color image, both the ring contact on top and the bottom contact surrounding the LED mesa are visible, allowing contacting of individual LEDs with different mesa sizes.

Electrical characterization of the grown 8.5 at.% homojunction LED is depicted in **Fig. 5.4**a. Two very distinct regimes, under forward and reverse bias, are visible in the shown $I-V$-curves. In forward direction, the junction barrier is lowered, allowing carrier transport into the former depleted junction region. In this regime, the device's operation as light emitter can be expected. On the other hand, current flow in the reverse-biased regime is strongly suppressed, as only a small number of carriers is able to overcome the energetic junction barrier. In this regime however, devices are suitable to function as passive optoelectronic components, such as photodetectors. In those, optically excited electron-hole pairs are separated by the electric field across the junction, leading to a measurable current flow.

While the fabricated GeSn diodes apparently allow versatile applications, emphasis

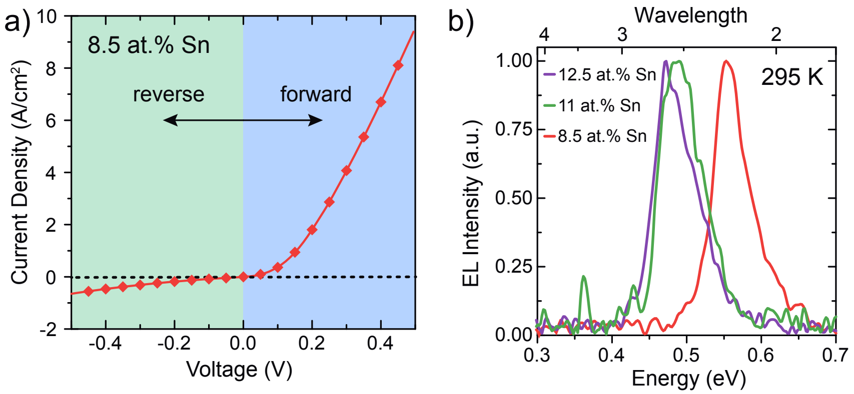

Figure 5.4 – a) I-V curves of a 8.5 at.% Sn LED shows distinct forward and reverse bias regimes for light emission and absorption devices. b) Demonstrated tuning of emission wavelength by incorporated Sn content.

will be placed on their use as light emitters in the following. In this regard, normalized EL emission, collected at 295 K, of three different homojunction diodes is compared in Fig. 5.4b. As demonstrated, light emission can be tuned by GeSn composition of the LED. While a diode with 8.5 at.% Sn features room-temperature light emission at about 0.551 eV (2.25 µm), emission is redshifted to 0.472 eV (2.63 µm) for a 12.5 at.% Sn diode. From band structure calculations, the latter one also comprises a fundamentally direct bandgap with a directness of 67 meV, making it a much more efficient light emitter, compared to the 8.5 at.% Sn diode with 4 meV directness.

Next the influence of different doping schemes in homojunction diodes is discussed. **Figure 5.5**a and b show ECV measurements of two homojunction diodes, referenced to as samples A and B, respectively. Both are grown with identical growth parameters, yielding 8.5 at.% Sn in the active region. In sample A, however, the bottom and top parts are p- and n-type doped, respectively, which is inverted for sample B. Comparing both ECV spectra yields steeper doping profiles in the top layer. One reason is certainly a broadening effect, as etching through the sample during ECV determination is not perfectly homogeneous. Second, also the p-type misfit defects, present at the bottom hundred nanometer's, may disturb the measurement. Comparing the nominally intrinsic region in both devices, a slightly higher, but decreasing p-type doping ($3 \times 10^{17}\,\text{cm}^{-3}$ vs $1.5 \times 10^{17}\,\text{cm}^{-3}$) is visible in sample

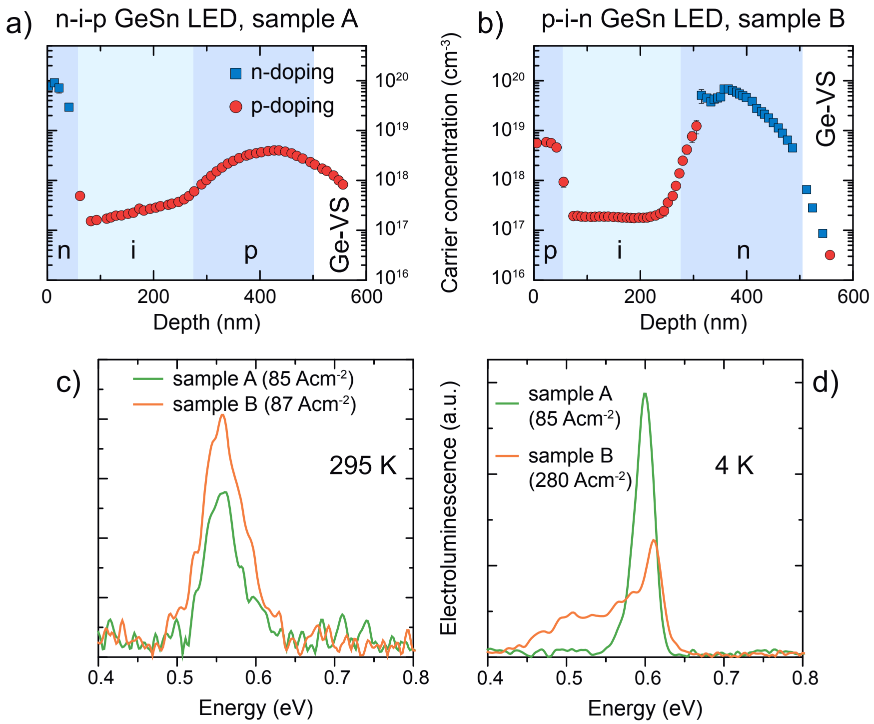

Figure 5.5 – Carrier profiles, determined by ECV, of two similar n-i-p a) & p-i-n b) stacks. Room temperature c) and 4 K d) electroluminescence spectra prove benefits of the first design, since recombination takes place further away from the defective bottom interface.

A. This may be related to residual diborane molecules in the reactor chamber, which leads to unintentional doping of the intrinsic layer. As much higher diborane flows are necessary to obtain sufficient p-type doping, compared to phosphine and n-type doping, the unintentional doping effect is only visible in sample A.

In figure 5.5c, room temperature EL spectra of both samples are depicted. For the same injected current density of about 85 A cm^{-2}, light emission in both samples is quite comparable, only slightly stronger in sample B. The situation changes dramatically at cryogenic temperatures of 4 K, depicted in Fig. 5.5d. Here, strong light emission is visible in sample A, while emission from the band edge is rather weak in sample B, despite a higher injection current in the latter one. Furthermore, sample B features a rather broad side emission band between 0.45–0.6 eV. Since this emission is energetically positioned distinctly below the fundamental bandgap of the $Ge_{0.915}Sn_{0.085}$ material, it must be linked to radiative transitions through impurity states in the bandgap. Thias may be related to misfit defects from the GeSn/Ge-VS interface. Since intrinsic GeSn is also slightly p-type, the main p-n-junction, where recombination occurs, is located between the intrinsic and n-type carrier injection region in both samples. For sample A, this p-n region is located ∼50 nm below the sample surface. In sample B, however, the region is located much closer to the bottom interface, so injected carriers in this region are much more likely to recombine through the available trap states. It shall be noted that sample B further exhibits slight contact problems at cryogenic temperatures. Nonetheless, those should not be the cause for the observed side band emission. Therefore, optimized devices shall position the p-n junction far away from any defects by appropriate doping schemes as in sample A. Further improvements in efficiency may be achieved, if injected carriers can be confined electronically, far away from any defective regions. The most apparent way to reach this, is the introduction of heterojunctions in the LED, which will be discussed in the next section.

5.3 Sn-based heterostructures for light emitters

After the demonstration of epitaxy and light emission of simple homojunction LEDs has been shown, this section covers different ways for improving light emission from group IV LEDs. It deals with different heterostructure designs, DHS and MQWs, and the use of different barrier materials for efficient carrier confinement in the GeSn active regions.

5.3.1 GeSn/Ge MQW LEDs

The first and most straight-forward approach is to use bulk Ge as barrier material. A multi quantum well LED was grown, comprising of seven GeSn (8 at.%) wells and Ge barriers, to maximize the obtainable emission. The structure further features a 115 nm thick boron-doped GeSn buffer ($\sim 1.4 \times 10^{18}\,\mathrm{cm}^{-3}$) and a 60 nm thick

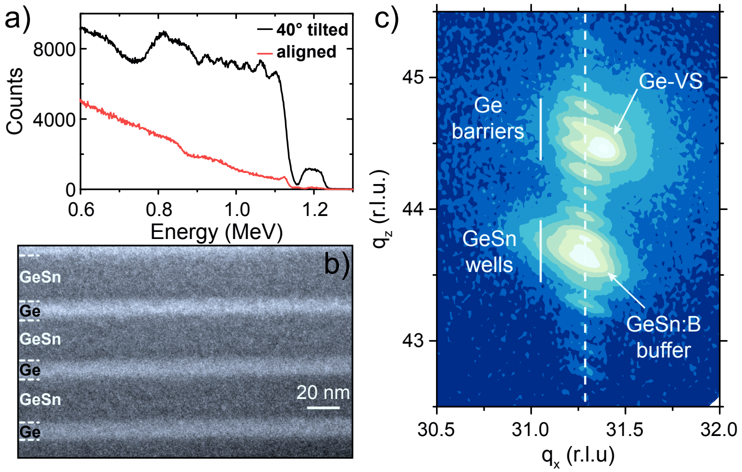

Figure 5.6 – a) Oscillations in RBS spectra are clear signature of the GeSn/Ge MQW structure, yet implying a small minimum channeling yield. Sharp interfaces within the MQW region can be proved from TEM micrograph in b), and also condense in strong oscillations of a GeSn/Ge superlattice in the RSM c).

phosphorus-doped cap layer ($\sim 7 \times 10^{19}\,\mathrm{cm}^{-3}$) for carrier injection.

RBS spectra of the grown sample are shown in **Fig. 5.6**a. For a better separation of well and barrier region, random spectra were gathered under a tilt of 40°. Clear oscillations occur in the acquired random spectrum, which are linked to an oscillating signal of Sn atoms in the multi well region. As visible in the channeling spectrum, the structure yields a high crystalline quality with only a small number of atoms at interstitial sites.

A cross-sectional TEM micrograph, visible in Fig. 5.6b shows a close-up of the inner well region. GeSn layers with a thickness of 20 nm are clearly distinguishable from the 14 nm thin Ge barriers, due to different contrasts, originated in their varying atomic masses. The structure features sharp interfaces without any interface defects, underlining the high structural quality.

Absence of newly generated defects can further be substantiated from the RSM. The MQW was grown fully coherently on top of the GeSn:B buffer, with perfect matching of their in-plane lattice constants. The high number of distinct satellite peaks, oscillations visible in the RSM, are additional evidence of sharp interfaces in

Table 5.1 – Structural properties of both multi quantum well LEDs.

Structure	Sn in well (nm)	strain in well (%)	active region thickn. (nm)	Si/Sn in barrier (at.%)	barrier thickn. (nm)
GeSn/Ge	8.0	-0.71	20	-/-	14
GeSn/SiGeSn	8.6	-0.24	19	10.5/10.9	11

the well region. Its spacing yields a superlattice constant of 37 nm, comparable to the values determined from the TEM micrograph. Since both, well and barrier, strongly differ in their cubic lattice constants, a separation of both contributions is possible from the RSM. This allows separate determination of strain in both regions, while normally RSM can only deliver an average value of the superlattice. It eventuates that the Ge barriers even feature a tensile strain of 0.48 %, while the GeSn wells are still slightly compressively strained by about $-0.71\,\%$. Especially the former will play an important role, when judging LED performance, as will be later discussed. Previously however, epitaxy of a MQW LED shall be discussed, employing SiGeSn ternaries as barrier material. An overview on structural properties of both MQW LEDs can be found in table 5.1

5.3.2 GeSn/SiGeSn MQW LEDs

To probe the influence of the barrier material on light emission properties, a similar MQW structure was grown as before. Again, a stack of seven wells, separated by barriers was grown on top of a readily-doped and partially strain relaxed 280 nm thick GeSn buffer, in this case, however, employing SiGeSn instead of Ge as barrier material. Several further growth optimizations were performed in this sample. Phosphorus doping of the buffer ($\sim 3 \times 10^{19}\,\mathrm{cm^{-3}}$), for example was stopped 60 nm prior to the heterojunctions, to avoid unintentional doping of the active device region.
Figure 5.7a features a RSM of the grown structure. A clear peak can be assigned to the GeSn buffer, with wells and barriers grown coherently on top. From this, strain in the structure can be determined to $-0.24\,\%$ in the well and $-0.09\,\%$ in the barrier region. Ideally, strain compensation between wells and barriers in such structure is achieved by alternating tensily and compressively strained layers. In

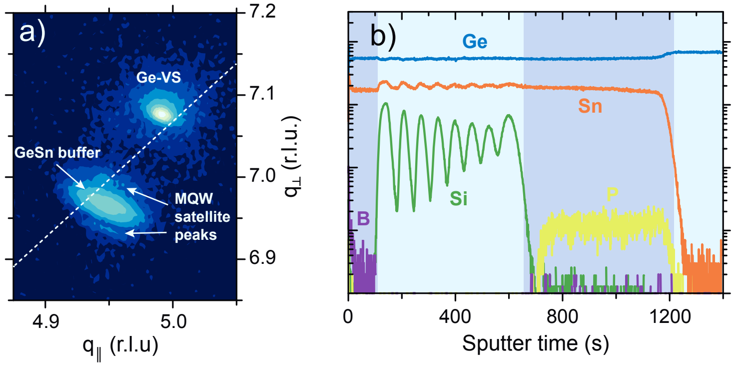

Figure 5.7 – a) RSM of the grown GeSn/SiGeSn MQW structure. b) Wells and barriers, as well as doped buffer and top region can be distinguished from the SIMS profile.

case of direct bandgap GeSn alloys, the required amount of Si, necessary for tensile strained ternaries, is not reachable in low-temperature CVD grown layers so far. From the RSM, only the first order satellite peaks of the MQW structure are identifiable. Reason for this observation may be the non-ideal periodicity of the device, which is also visible from the SIMS profile in Fig. 5.7b. Herein, barrier and well regions can be clearly distinguished from the oscillating signal of Si atoms, while only slight oscillations stemming from Sn atoms are visible. Merging of the Si signal in bottom barriers may be an artifact due to inhomogeneous sputtering during SIMS profiling. The decrease in intensity, however, suggests real fluctuations in Si incorporation, indicating non-ideal growth parameters. This is further underlined by the oscillations in Sn signal, which slightly enhances in the barrier regions. Increase of Sn incorporation after introduction of Si during growth was a previously discussed effect (c.f. section 4.1.1), likely stemming from local strain compensation of the small-sized Si atoms. During heterostructure growth this phenomenon should be avoided, as a higher Sn content in the barrier decreases the possible carrier confinement. *Atom probe tomography* (APT) was used to quantify the Sn enhancement (not shown here), yielding compositions of 8.6 at.% Sn in the GeSn wells and 10.5/10.9 at.% Si/Sn content in the SiGeSn barriers. As discussed below, these values are still sufficient to obtain type I alignment of electrons in the well regions.

The average thickness of well and barrier regions was determined to 19/11 nm and poses a critical parameter for device performance. On purpose, we chose a reasonably thick well dimension, leading only to a rather small quantization of about 16 meV for Γ electrons. The reason lies within the small directness of GeSn alloys. As a first approximation, energy states from quantum confinement in the GeSn region can be treated by a *particle in a box* model, yielding quantized states at

$$E_n = \frac{\hbar^2 \pi^2 n^2}{2m^* d^2}, \tag{5.5}$$

with effective mass m^* and well thickness d. As Γ electrons feature a much smaller effective mass than L electrons, their energy states are elevated much stronger in thin wells, therefore deteriorating the already small directness of the material.[225] Therefore, in our scheme we use wells mainly for carrier confinement. Also the influence of barrier size may be discussed systematically. While thick barriers entail higher resistances during carrier exchange between wells, this exact overlap of wells in thin barriers may impede analysis of light emission by broadening of the quantized states into minibands. Such analysis, however, lies beyond the scope of this thesis. An overview on the structural properties of both grown MQW LEDs can be found in table 5.1.

To probe the influence of SiGeSn barriers on light emission, electroluminesce of fabricated LEDs was recorded and compared to that of previously investigated GeSn/Ge MQW LEDs.

As visible in **Fig. 5.8**a, the LED comprising SiGeSn barriers shows much stronger light emission at room temperature, with a definitely stronger signal-to-noise ratio. This superiority can be understood when the band structure of both devices is considered. Band alignment for the GeSn/Ge MQW is given in Fig. 5.8b, which can be compared to that of the GeSn/SiGeSn structure in Fig. 5.8c. The calculations further include positions of the first two quantized states of Γ and *heavy hole* (HH) bands as dashed lines. A slightly smaller Γ position (and higher directness) is visible for the SiGeSn-containing LED, which mirrors itself in a small redshift in EL emission, visible in Fig. 5.8a. Still, it shouldn't cause a strong difference in emission intensity, as both structures have a fundamentally indirect bandgap in common, which is not ideal for efficient light emission. Apart from that, clear differences can

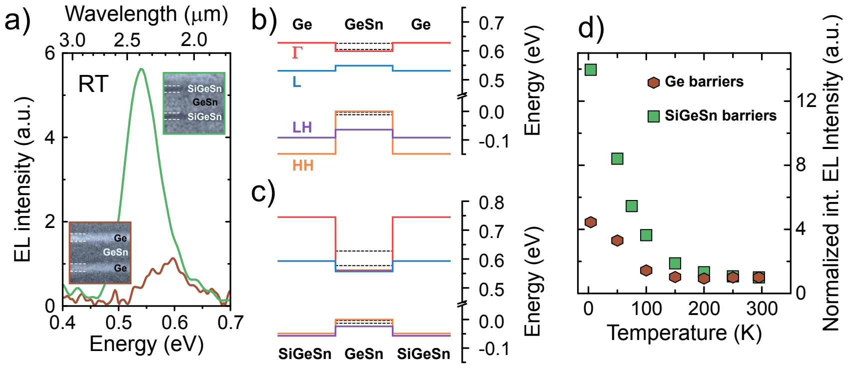

Figure 5.8 – a) Room temperature electroluminescence of the GeSn/Ge (brown) and GeSn/SiGeSn (green) MQW LEDs show clear differences in EL emission, originated from the differing band alignments, which are shown for both devices in b) and c). Efficient carrier confinement is reachable only in case of SiGeSn barriers, which also mirrors itself in more efficient temperature dependent emission, visible in d).

be seen for both LEDs in band alignment between well and barrier region. In case of Ge barriers, no type I band alignment can be achieved for electrons in the structure. Electrons at the L-valley, which actually provide the overwhelming number of electrons due to their large effective mass, cannot be confined inside the GeSn wells, but are rather located in the Ge barriers. The reason for this separation is the tensile strain in Ge, which was induced from coherent growth on top of partially relaxed GeSn layers. This effect poses an overall drawback for using Ge barriers, as it also increases for even higher Sn incorporations in the active region. Calculations have shown that only a slight type I confinement of maximum 40 meV is reachable at room temperature in a small parameter region, which may not be efficient for room temperature lasers.[225]

In the case of SiGeSn barriers on the other hand, a clear type I band alignment, thus confinement of electrons in the well region, is visible. In the shown calculations, an optical bowing parameter of $b_{\mathrm{SiSn}} = 3.9\,\mathrm{eV}$ was assumed. As discussed previously, a much higher bowing coefficient is expected due to its compositional dependence. For a value of 19.2 eV, confinement shrinks to 11 meV, albeit one has to keep in mind that exact values from theoretical calculations has to be considered with care, as they tend to overestimate the SiGeSn's directness.

The indication of superiority of SiGeSn barriers, however, is still valid, further underlined by normalized temperature dependence of light emission from both LEDs in Fig. 5.8c. Compared to the LED with Ge barriers, a much stronger EL increase is observed at cryogenic temperatures. One contribution originates from the slightly higher directness in that sample, resulting in a higher fraction of electrons at the direct Γ-valley. Another contribution is caused by an efficiency increase of the SiGeSn-containing LED. At lower temperatures, the still rather small carrier confinement is able to keep an increasing number of electrons in the well region, thus strongly reducing the radiative recombination time. With that, efficiency of the LED increases in compliance with equation (5.4), yielding stronger light emission.

Therefore, in contrast to Ge barriers, SiGeSn provides a path towards efficient heterostructure light emitters. Still, so far in this thesis only GeSn alloys with rather small amounts of Sn were combined with SiGeSn claddings. In the following section, finally the merging of direct bandgap GeSn and SiGeSn ternaries for advanced heterostructure emitters is discussed.

5.3.3 Direct bandgap heterostructure light emitters

In this section, advanced structural characterization of different types of direct bandgap group IV heterostructures is discussed. Two different types of heterostructures are investigated in the following. The first type are double heterostructures (DHS), in which the active layer is sandwiched in between thin SiGeSn cladding layers. The other type applies a multi quantum wells (MQW) design, with a total number of ten wells. Of both designs, a number of structures was grown to scrutinize the effect of different barrier material and well thicknesses. Overviews on the most important layer parameters of all grown layers are given in tables 5.2 and 5.3.

Double heterostructures (DHS)

The design approach of the grown DHS closely resembles the one from the previously grown LEDs. In contrast to those, however, these structures are formed without in-situ doping, to solely probe the structural and optical properties of those direct bandgap layers.

Table 5.2 – Overview on the main structural properties of grown direct gap double heterostructures.

Name	Sn in active region (nm)	strain in act. region (%)	act. region thickn. (nm)	Si/Sn in top cladding (at.%)	Si/Sn in bottom clad. (at.%)
DHS1	14.5	-0.56	377	4.5/14	5.5/11.5
DHS2	14.0	-0.70	342	5.0/13.5	5.5/13

Table 5.3 – Overview on the main structural properties of grown direct gap multi quantum wells.

Name	Sn in well (nm)	strain in well (%)	active region thickness (nm)	Si/Sn in barrier (at.%)	barrier thickness (nm)
MQW1	13.3	-0.68	22	4.8/13	22
MQW2	13.5	-0.81	12	5.2/13.4	16

The approach relies on the use of a roughly 200 nm thick GeSn (about 10 at.% Sn) buffer layer, which fulfills several purposes. First, it minimizes lattice mismatch between substrate and subsequently grown layers, allowing a homogeneous Sn incorporation in the active region. Supplying a larger-lattice growth template, it also reduces the amount of residual compressive strain in the active region, which is further beneficial in terms of bandgap directness. On top of the partially relaxed buffer, the actual SiGeSn/GeSn/SiGeSn DHS was grown. A TEM micrograph of a complete grown structure (DHS1) is shown in **Figure 5.9**a.

As discussed in chapter 3, a straight-forward way to increase Sn content for the active region is lowering of growth temperature. On the other hand, as demonstrated in chapter 4, this leads to a diminishing of Si incorporation into SiGeSn, thus reducing carrier confinement by the cladding. Two different strategies are pursued to find the optimal growth strategy. For the first sample, later referred to as DHS1, epitaxy of buffer and bottom SiGeSn cladding was performed at a temperature of 360 °C, before cooling down and subsequent growth of active region and top cladding at 350 °C. In the second case, only the buffer was grown at elevated temperatures before the reactor was cooled down. In that case, labeled DHS2, the complete DHS

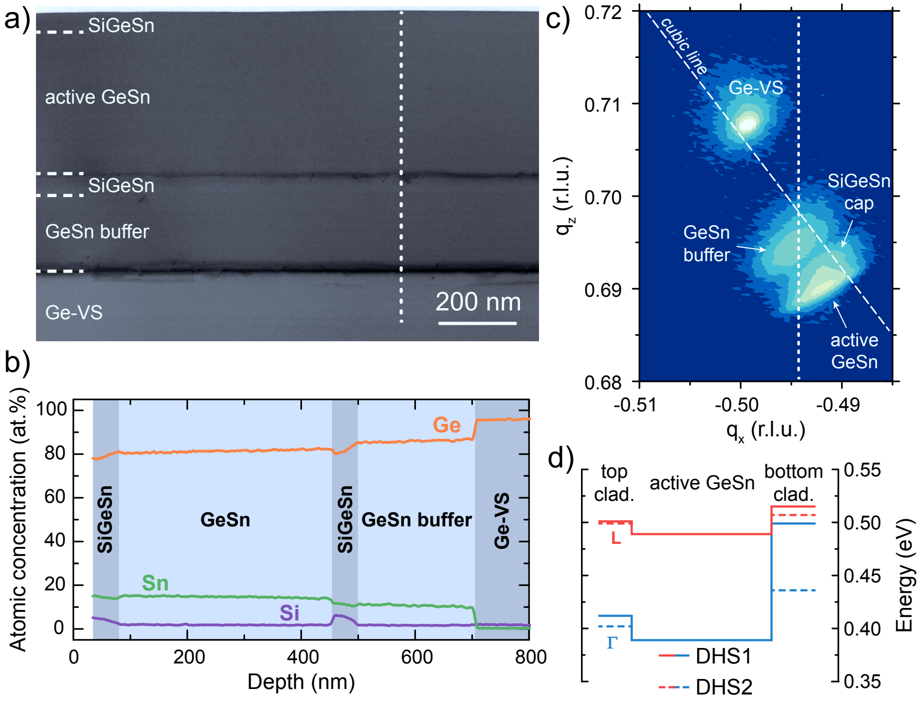

Figure 5.9 – a) TEM micrograph of the complete direct bandgap heterostructure DHS1. b) EDX linescan along the dotted line in a) enables separation of all layers. c) RSM suggests a partially relaxed active region on top of the GeSn buffer, which is source of additional misfit defects. d) Comparison of band alignments of both grown DHS.

was grown without any interruptions, which likely prevents the occurrence of thin Ge-rich interlayers in the structure. It may exhibit slightly higher roughnesses compared to DHS1, though, as epitaxy of SiGeSn at lower temperatures is always linked to smaller growth rates.

Interfaces between the different regions are marked by dashed white lines in Fig. 5.9a, since different layers cannot be distinguished from image contrast due to their similar compositions. They are, however, clearly separable from *energy dispersive X-ray spectroscopy* (EDX) in Fig. 5.9b, performed at IHP in Frankfurt/Oder. An EDX line scan, which was recorded in-situ during microscopy along the dotted line, shows the distinct regions of the grown layer stack of DHS1. On top of the GeSn buffer, the bottom cladding layer incorporates Si/Sn contents of 5.5/11.5 at.%. The Si atoms do not segregate into the active region, but are well confined within the cladding region.

The following 377 nm thick active $Ge_{0.855}Sn_{0.145}$ region shows very homogeneous Sn incorporation, while the top cladding layer with 4.5/14 at.% Si/Sn incorporation ensures confinement of carriers away from the surface and its non-radiative surface states.

Strain in all regions can be determined from the RSM in Fig. 5.9c, acquired likewise at IHP. The partially relaxed GeSn buffer is clearly visible and features residual compressive strain of $-0.40\,\%$. Both cladding layers are, if at all, only hardly visible in the RSM. The bottom cladding likely overlays the signal of the GeSn buffer, due to its Si but also slightly higher Sn incorporation. The active region itself relaxes further on top of the buffer layer, exhibiting smaller reciprocal lattice constants. Therefore, a second quality-deteriorating defective interface is expected at the SiGeSn/GeSn interface, as misfit dislocations are expected to accompany the additional strain relaxation. Indeed, a number of dislocations can already be seen in the TEM micrograph from 5.9a. No extra defects, however, are expected at the top cladding. Its signal can be seen in Fig. 5.9c coherently on top of the active GeSn region, sharing the same Q_x values.

From band structure calculations, a better carrier confinement is expected for DHS1, as shown in Fig. 5.9d. The smaller Sn incorporation in the bottom cladding produces larger band discontinuities to keep carriers in the active region. Confinement from the top cladding should be equal for DHS1 and DHS2, differences originate from slight variations in layer parameters, which are, however, within the error of measurements.

Investigations on lasing performance from both layers result in slightly smaller lasing thresholds for DHS1.[242] Still no distinct advantages compared to bulk GeSn layers were observed, which is related to the mentioned further defects at the active region. One possible expedient is growth of a stronger-relaxed buffer to inhibit additional strain relaxation of the active GeSn. Another route, which manages epitaxy without accessory defects, is growth of a MQW scheme, as demonstrated in the following section.

Multi quantum wells (MQW)

Both MQW structures (overview on properties in table 5.3) make use of the GeSn buffer technology, as presented before for double heterostructures. In this case, ten alternating cycles of GeSn well and SiGeSn barrier were grown as region of carrier recombination. The first structure, labeled MQW1, incorporates rather thick wells of 22 nm. The second one, MQW2, has much thinner wells of 12 nm. Thus, quantization effects are strongly pronounced in the latter, which will be discussed below. To gain information on elemental distribution and interfaces on a microscopic scale and investigate possible ordering effects inside that complex structure, *atom probe tomography* (APT) was performed. Detailed information on sample preparation and data analysis of this sophisticated technique can be found in the appendix.

In literature, different techniques were employed to assess possible ordering effects in (Si)GeSn alloys. While *extended X-Ray absorption fine structure* (EXAFS) found homogeneously distributed Sn atoms in GeSn alloys up to 12.4 at.%,[243] signs of Sn clustering was found in partially relaxed $Ge_{0.93}Sn_{0.07}$ alloys.[244] Furthermore, certain ordering effects and formation of local structure arise in SiGeSn ternaries with high Sn contents.[220,245] In our experiments, such investigations were performed not in bulk layers, but rather in complex heterostructures, in which additional effects from alternating material and internal strains are present.

Figure 5.10 shows APT data of the middle part from the multi well region of MQW1. In 5.10a, the distribution of Si atoms within the investigated specimen is shown. They are mainly found confined within the barrier regions, their segregation into wells is in the order of ∼0.3 ‰.

Atomic concentrations can be precisely determined from reconstructed APT data, because of the high number ($>1 \times 10^5$) of ions in the analyzed subvolumes. A profile scan, appertaining to the elemental map in 5.10a, is depicted in Figure 5.10b. Here it is visible that Si is incorporated rather constantly, but only within in the barrier region. Sn atoms, on the other hand, are nearly homogeneously distributed through all regions. Optimization of growth parameters helped suppressing Sn elevation inside the barriers, previously visible inside the SiGeSn/GeSn MQW LEDs (c.f. figure 5.7b on page 80). From APT data, Sn content inside GeSn wells was determined to 13.3 at.%, while the Si/Sn composition inside the barrier yielded 4.8/13.0 at.%.

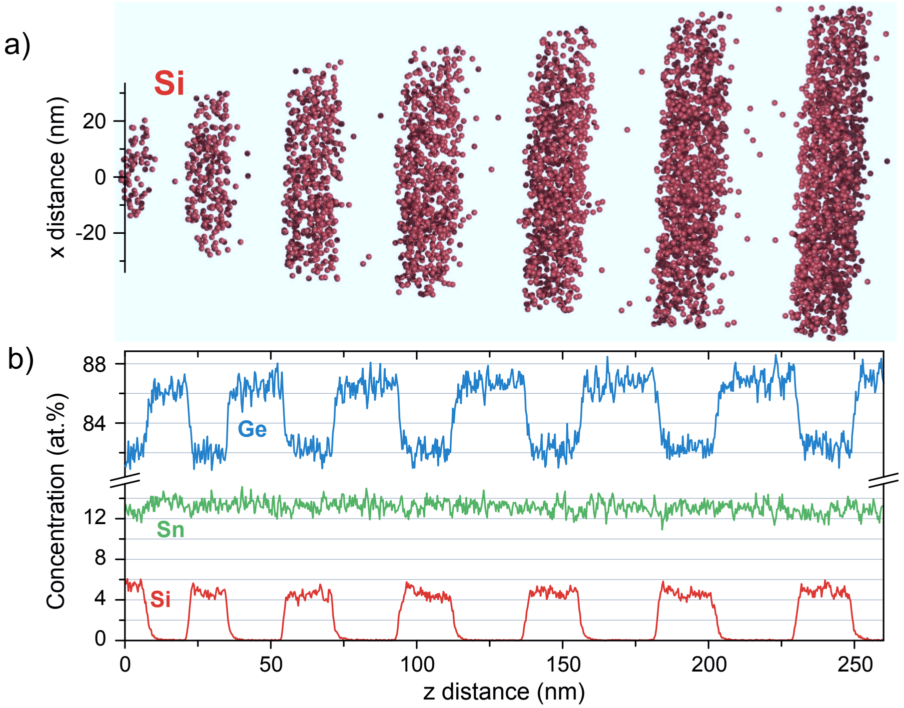

Figure 5.10 – a) APT elemental map of Si atoms enables identification of barrier and well regions. b) Line scans of elemental Si, Ge and Sn through the probed specimen proves sharp layers without strong compositional fluctuations.

The large number of detected ions, 31 millions in the investigated specimen in total, allows sophisticated statistical analysis of elemental incorporation and contingent clustering effects on a nm scale. Several statistical methods are shown for barriers and wells in **Fig. 5.11**.

Elemental frequency distribution analysis are plotted for well and barrier regions in Fig. 5.11a and b, respectively. Herein, the analyzed subvolumes (either well or barrier interior) are split into spatial blocks with 200 ions each and investigated for their composition. Values for all investigated blocks are histogrammed for Sn atoms inside wells in 5.11a and compared to a binomial distribution with bulk concentration as mean value. The latter distribution theoretically describes the dispersion of

Sn atoms (solute), randomly positioned inside a Ge matrix. In case of Sn atoms inside the wells, it perfectly matches the experimentally observed distribution. The same holds true for Sn atoms inside the SiGeSn barrier, as visible in Fig. 5.11b. For Si atoms, however, a small but definite deviation from the theoretically expected distribution is observed. The p-value, which is defined as the probability to find the experimentally observed distribution by randomizing atom positions, is calculated to be smaller than 0.1 ‰. Thus, only Sn atoms form a truly solid solution inside the Ge matrix of barrier or well, as previously also found in reference [220]. Nevertheless, only qualitative deviations from a solid solution can be stated for Si atoms from this elemental distribution analysis. To learn more about local variations, positions of nearest neighbors in the alloys was further analyzed in Fig. 5.11c and d for well and barrier, respectively.

In Fig. 5.11c, Sn-Sn *nearest-neighbor* (NN) analysis was performed on the dataset (open symbols) and compared to a randomized GeSn solution (solid line). No distinct deviation is visible between experiment and random solution, strongly underlining the random character of Sn incorporation in the GeSn alloy. Again, the same behavior is also visible for Sn-Sn NN within the SiGeSn barrier region. A (very) slight difference, however, can be seen for Si-Si NN. The average position of the first neighbored Si atom is minimally shifted to smaller values, compared to a random solution. There seems to be some kind of interaction, keeping Si atoms in a shorter distance in respect to other Si atoms on average. In literature, a repulsive interaction between Si and Sn atoms is discussed.[220] It originates in an energetically unfavorable configuration of Si-Sn, requiring additional energy compared to a third- or fourth NN configuration. Due to the rather small number of Si atoms in the investigated subvolume, the shift is not very distinct.

Therefore, another technique for detection of clustering or phase separation is investigation of *radial distribution functions* (RDF). In our case, we again concentrated on RDFs of Si-Si and Sn-Sn distribution. Then, the RDFs represent an averaged, distance-dependent Sn (Si) concentration profile, surrounding every single Sn (Si) atom. Figure 5.11e, showing the Sn-Sn RDF within the well region, reflects several distinct features. To begin with, the closest region below 0.2 nm can be excluded from the analysis, since no neighboring atoms can physically be found below a similar threshold in bulk Ge.[246] Data points, detected at smaller distance, are found

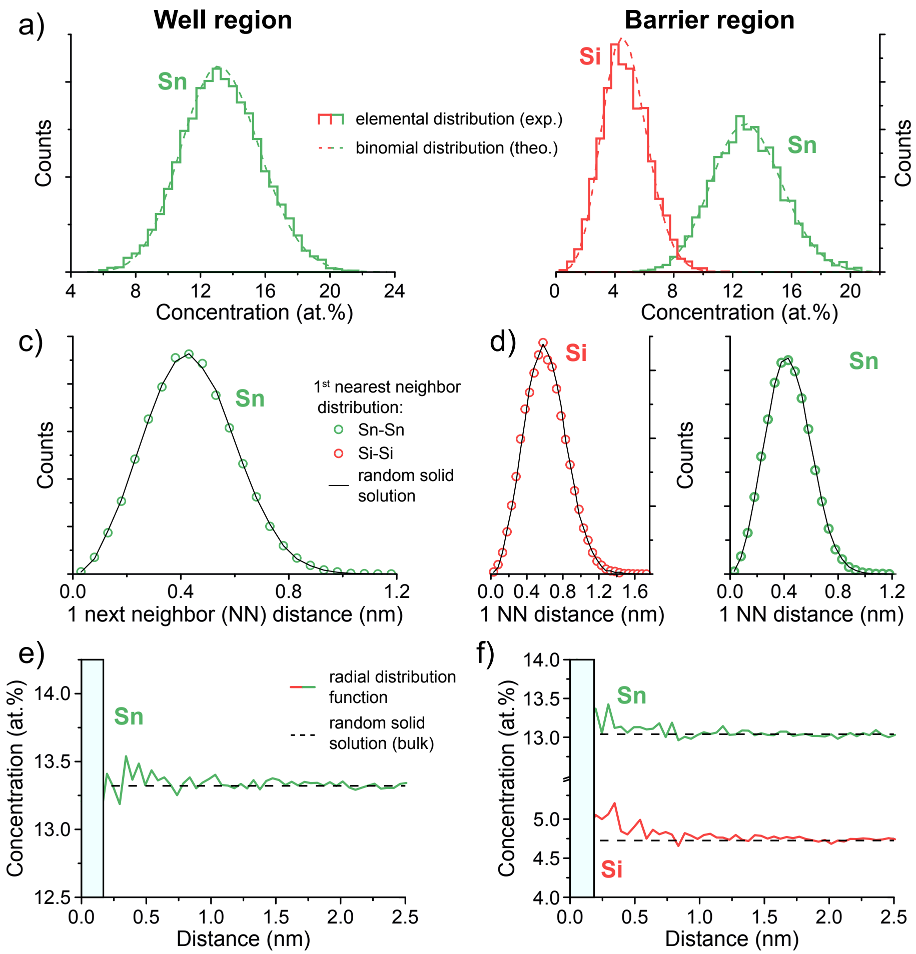

Figure 5.11 – Statistical analysis of reconstructed APT data for wells and barriers. a) and b) depict elemental frequency distribution of Sn and Si in wells and barriers, respectively. First nearest neighbor distribution of Sn-Sn & Si-Si in both regions are shown in c) and d). Radial distribution function for Si-Si and Sn-Sn in well e) and barrier f). All analyses yield randomly distributed Sn atoms inside wells and barriers, while an attractive interaction keeps Si atoms in closer vicinity than theoretically expected for a solid solution.

because of a limited spatial resolution, leading to a lower atom positioning accuracy. Apart from that, the Sn-Sn RDF very quickly saturates at bulk compositions ($>$ 0.5 nm), which is another indication for the random spread of Sn atoms within GeSn wells.

In case of SiGeSn ternaries, the results are more ambiguous, which could be expected also from previous analysis. While the Sn-Sn RDF is nearly constant at the bulk concentration, Si atoms show a positive correlation with respect to themselves. A larger number of those can be found in close environment to other Si atoms, as indicated by elevated concentration values for distances smaller than $\sim$1 nm in Fig. 5.11f. During epitaxial growth, Si atoms tend to be built-in favorably at sites encompassing other Si atoms. On larger scales above $\sim$ 2 nm, however, the RDF-determined concentration saturates again at bulk composition, as indicated by the dotted line.

In conclusion, statistical analysis of reconstructed APT data substantiates certain ordering of Si atoms within the SiGeSn alloy. These findings, previously found also in high Sn-content bulk ternaries,[220] reveal an apparently intrinsic feature of SiGeSn ternaries, which is still present in heterostructure devices. Physically, it may be the origin of the unusually strong composition dependence of the optical SiSn bowing parameter b_{SiSn}, which was previously investigated in section 4.2.2. It shall be noted, however, that despite a certain kind of ordering, no strong segregation or even clustering of Si atoms was observed within the barrier layers.

Another highly desired parameter for band structure calculations, besides composition, is the exact strain in the grown structures. Since XRD measurements can only resolve an average strain of the complete super-lattice, another technique used for investigation is *dark-field electron holography* (DFEH). DFEH is carried out in a transmission electron microscope with the help of an electron biprism. It relies on interference of electron beams, one of which passes through a reference region (in our case the Ge-VS), the other one crossing the regions of interest (wells and barriers). The diffracted parts of both waves interfere, the resulting hologram contains information on the phase difference of both beams. From that, the lattice deformation in the region of interest can be calculated relative to the reference region with a spatial resolution of about 6 nm. Details on the methodology can be found in references.[247,248]

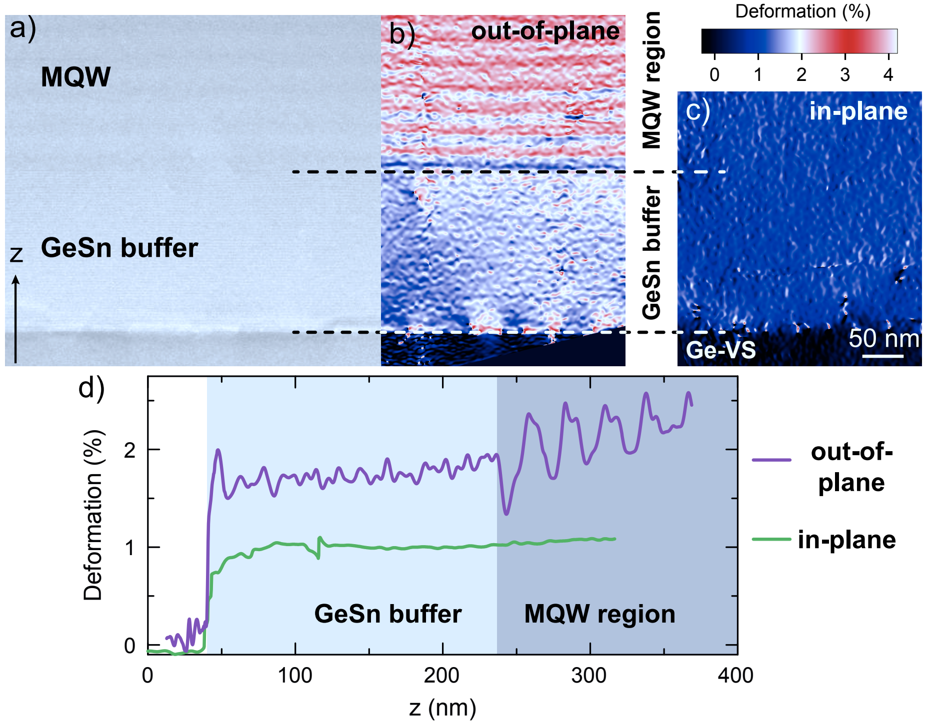

Figure 5.12 – a) HAADF micrograph of MQW2 and the respective out-of-plane b) and in-plane c) lattice deformation maps, relative to the Ge buffer. The scale bar is valid for a)-c). d): Line scans through both maps show coherently grown MQWs on top of the GeSn, with stronger compressive strain within the GeSn region.

DFEH measurements, performed on MQW2, can be found in **Fig. 5.12**. A *high-angle annular dark-field* (HAADF) image, taken by TEM, shows the region of interest in Fig. 5.12a, while the corresponding out-of-plane and in-plane lattice deformation maps are shown in b and c, respectively. The MQW region on top of the GeSn buffer can only hardly be distinguished from slight contrast oscillations in the micrograph. It can much better be resolved from trends in lattice deformation in Fig. 5.12b and c. As the Ge-VS is taken as reference, already the GeSn buffer shows a distinct lattice deformation, both in in- and out-of-plane direction. On top of the GeSn buffer, the MQW is visible from periodic oscillations of the out-of-plane

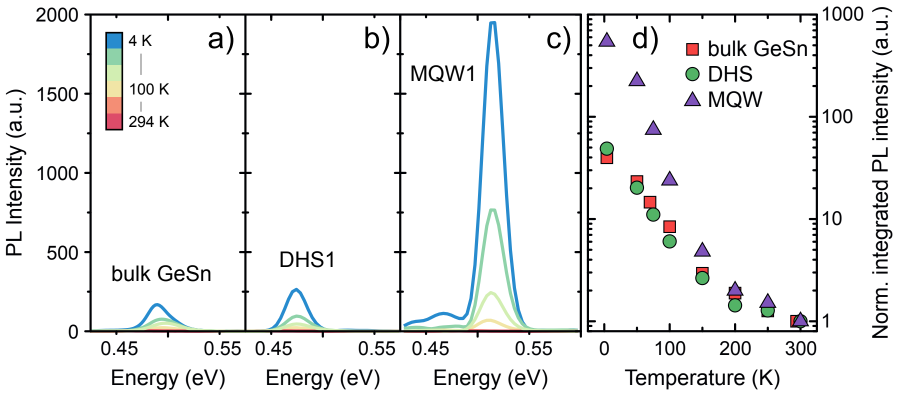

Figure 5.13 – Temperature dependent PL intensity for bulk $Ge_{0.875}Sn_{0.125}$ a), DHS1 b) and MQW 1 c). d) MQW1 shows strongly increased emission intensity at cryogenic temperatures, originated in an efficient carrier confinement and an absence of misfit defects close to the active region.

lattice deformation, while no real change of the in-plane lattice constant is detected between GeSn buffer and MQW in Fig. 5.12c. This is exemplified with the aid of two profile scans through both in- and out-of-plane deformation maps in Fig. 5.12d. The constant in-plane deformation of buffer and MQW indicates that the complete MQW stack is grown coherently on top of the GeSn buffer, without further lattice relaxation. Due to larger cubic (relaxed) lattice constant of the GeSn, compared to SiGeSn, the former is under higher compressive strain, which results in a larger out-of-plane lattice constant, visible also in Fig. 5.12d.

The most important finding is the prove of pseudomorphic growth and consequently the absence of additional misfit dislocations at the interface adjacent to the active region. This will greatly enhance light emission compared to the DHS structures by extending the non-radiative recombination time. To demonstrate this effect, temperature dependent photoluminescence spectra of bulk and heterostructure designs were recorded between room temperature and 4 K and discussed in the following.

A comparison of light emission between a bulk GeSn sample – with 12.5 at.% Sn and $-0.43\,\%$ strain – and both types of heterostructures (DHS1 and MQW1) is shown in **Figure 5.13**. Comparing bulk GeSn and DHS1 in a and b, photoluminescence with similar intensity is observed. Strongest light emission is obtained at cryogenic temperatures for both, related to a temperature-related increase of non-radiative recombination time. Emission is increased to such an extent that light emission above around 100 K cannot be displayed in the given scale anymore. The first important finding is that the introduction of SiGeSn alone does not worsen light emission in the heterostructure. The slightly higher radiative recombination efficiency may be explained by the slightly higher Sn content and thus directness, compared to the bulk GeSn sample.

A different behavior becomes apparent in case of MQW1. Despite having a smaller volume of active material (10×22 nm wells vs. 377 nm active region), light emission is strongly enhanced at 4 K. In contrast to both former samples, no additional misfit dislocations are present close to the active region in this sample, which seems to limit light emission in former samples. Therefore, SiGeSn barriers are able to efficiently screen carriers in the active region from unpreventable misfit defects.

A certain drawback, however, is currently still present and can be observed from a comparison of all samples in Fig. 5.13d. The described superiority of MQW devices – normalized PL intensity increases an order of magnitude stronger in MQWs at 4 K – appears only at cryogenic temperatures. When temperature is elevated above roughly 200 K, no distinct advantage of MQWs over DHSs is observed anymore. This finding indicates that confining of carriers far away from non-radiative recombination sinks, is not yet efficient at higher temperatures. The increased thermal energy of carriers is then sufficient to overcome the energetic barriers from the SiGeSn interlayers and reach the defective bottom interface. An obvious solution for future devices would be to further increase Si content of the ternary claddings, to allow even stronger confinement of carriers. In that case, the big advantage of MQWs – absence of defects at the active region – would manifest itself in strongly increased room temperature light emission and should be the path pursued for room temperature electrically-pumped group IV lasers. At this point it should be emphasized that despite current drawbacks, lasing from MQW structures was observed, yielding even reduced lasing thresholds compared to bulk layers.[242] Discussions on those properties, however, are not part of the current thesis.

As mentioned before, on one hand lasing would strongly benefit from size quantization effects due to the two-dimensional density of states. On the other hand, quantization in GeSn would impair the layer's directness and carrier confinement

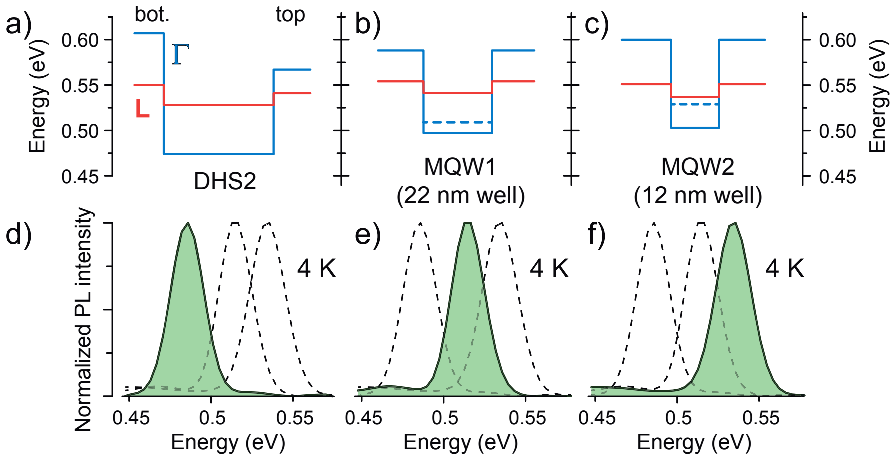

Figure 5.14 – Conduction band calculations for DHS2 a), MQW1 b) and MQW2 c), with their respective low temperature light emission d)-f). A good agreement between theory and experiment is observed, proving emission from quantized states in the MQW structures.

within the well. Yielding higher Si contents in the barrier could solve the latter restraints. However, already in present devices the effect of quantum confinement is visible from light emission, as shown in the following.

In **Fig. 5.14**, calculated conduction band positions are shown for different heterostructures, calculations for DHS2 are shown in a, for MQW1 and MQW2 in b and c. In both latter cases, the full lines represent bulk positions, while the first quantized Γ states are given as dotted lines. To allow an easy comparison of all structures, band structures are aligned at their top valence band, which correlates to the first quantized HH state in case of the MQW samples. Normalized PL spectra, recorded at 4 K of all structures are juxtaposed in 5.14d, e and f to illustrate quantum confinement in the well regions.

For the double heterostructure DHS2, light emission at 0.485 eV, shown in Fig. 5.14d, closely fits the theoretical prediction of 0.474 eV. For MQW1 in Fig. 5.14e, a definite emission blueshift is observed, which originates from two different reasons. First, Sn content in the wells is slightly reduced compared to DHS2 (13.3 at.% vs. 14 at.%). Further, quantum confinement in the well (dashed line) imposes an additional bandgap elevation.

Factoring in also MQW2, an additional emission blueshift of 20 meV is observed in Fig. 5.14f compared to MQW1. Since slight differences in Sn content and strain in both MQW structures cancel out each other, the observed emission shift can solely be attributed to stronger quantization effects, as indicated by the band structure calculations. Thus clear emission of quantized states is observed in the MQW samples, although their directness may not yet be sufficient for room temperature lasing applications.

5.4 Integration of Sn-based materials in photonic integrated circuits

One strong advantage of Sn-based group IV alloys over heterogeneous III-V integration on Si, is the possibility to use the same processing environment. As the former are chemically and structurally compatible to the mature Si CMOS technology, the danger of material contamination is strongly reduced.

In collaboration with the institute of Integrated Photonics (IPH) from the RWTH Aachen, who provided the design and circuit modeling,[249] a circuit is demonstrated, employing several key features for integrated devices.

The proposed structure was fabricated in the Forschungszentrum Jülich cleanroom on bulk GeSn alloys, incorporating 12.5 at.% Sn and a thickness of roughly 500 nm, using only Si-compatible processing technology. Similar as for the fabrication of light emitting diodes (c.f. previous sections) process modules, such as Cl_2/Ar or CHF_3-based reactive ion etching, optical and e-beam lithography were used to fabricate integrated photonic components in both positive and negative process flows. An overview on a full circuit is given in **Fig. 5.15**a. It consists of a central waveguide (WG) region, which will later be used as gain region for the integrated laser. Adjacent at both sides of the waveguide are multi mode interferometers (MMI), which allow splitting of the light into both arms of connected Sagnac loops. Those provide an efficient resonator for amplification of light. Light waves travel clockwise and counter-clockwise through the Sagnac loops, which allows much stronger reflection – $\sim 89\,\%$ for an optimized design in[249] – compared to plain facets ($\sim 38\,\%$ at GeSn/air interface, based on their refractive indizes). Laser light can be effectively coupled out from the resonator to an adjoined waveguide with grating coupler for

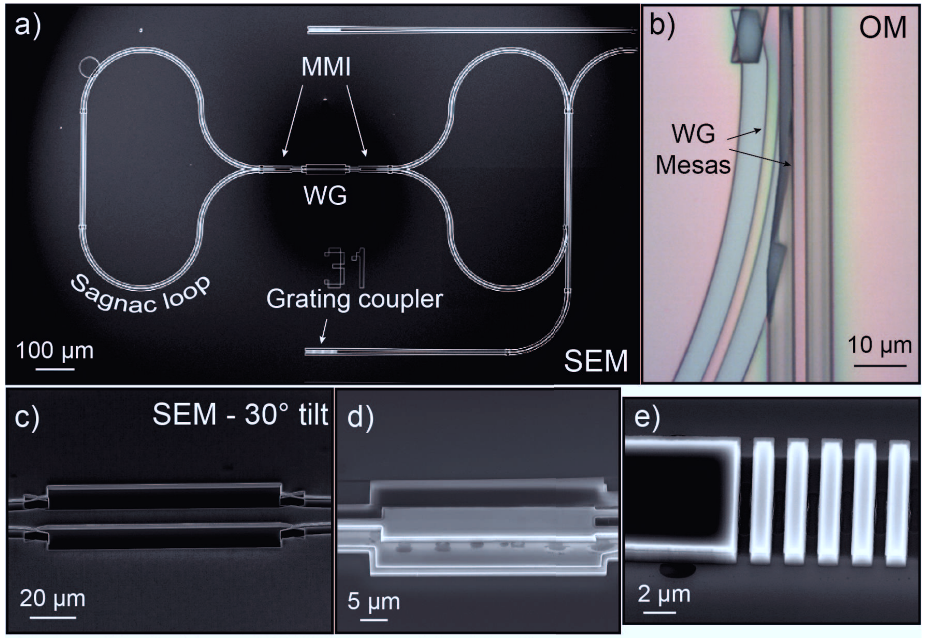

Design: Martin Adams (RWTH Aachen). Fabrication: Nils von den Driesch (FZ Jülich).

Figure 5.15 – a) SEM micrograph of an integrated light source, employing a central waveguide (WG), Sagnac loops as resonator, and an adjacently coupled waveguide with grating coupler for perpendicular light extraction. b) Optical micrograph of the adjoined WG region. Tilted SEM images for several circuit parts: wave guide c), multimode interferometer d) and grating coupler e).

perpendicular out-coupling. Part of the adjoined waveguide region is shown in an optical micrograph in Fig. 5.15b. A small part of the light is adjacently coupled into the second waveguide, which only slightly impacts the resonator's quality (Q) factor and could then be used for other on-chip optical circuits.

In Fig. 5.15c a 30° tilted SEM micrograph of the waveguide region is shown. Here, the waveguide was defined by etching surrounding trenches. A later underetching would further reduce the direct bandgap, as well as increase material's directness. Especially the former is uttermost important, to allow lasing at an energy below the bandgap of the *partially strained* material and, therefore, reduce absorption in the non-underetched resonator regions.

The fabricated MMI is depicted in Fig. 5.15d. As visible, several etch steps with varying etch depths are required to allow efficient functionality. Those different step heights in the order of µm are demonstrated to be reliably fabricated with good alignment.
A close-up of a grating coupler is presented in Fig. 5.15e. In here, etching of rather steep side walls is demonstrated, allowing an efficient out-coupling of light from the integrated emitter.
In conclusion, processing of Sn-based material is demonstrated for integrated light emitters. Integration of more complex heterostructures shall thus be feasible in future designs.

5.5 Summary

The final section of this thesis combined all the different components, investigated in previous chapters. Epitaxy of diverse structures for light emitters was shown and extensively inspected. Advanced characterization techniques, such as *atom probe tomography* (APT) or *dark-field electron holography* (DFEH) were employed to gain microscopic understanding of structural properties of the grown structures. Further, light emission from both LEDs and undoped heterostructures prove efficient device structures. In the following, the most vital findings are outlined.

- Epitaxial growth of homojunction LED layer stacks, incorporating 8–12.5 at.% Sn, was demonstrated. In-situ doping for electron and hole injection layers enabled fabrication of light emitting diodes, which show distinct regimes for emission and absorption devices, while their working wavelength range can be adjusted by the incorporated Sn content.

- For the first time, a heterostructure device was demonstrated incorporating both GeSn and SiGeSn, albeit so far only for fundamentally indirect GeSn material. Introducing also Ge, the epitaxy of two types of multi quantum well heterostructure LEDs was shown. While the structural quality of both devices, using either SiGeSn or Ge as barrier material, was excellent, a better carrier confinement in case of SiGeSn barriers was found, making those heterostructures most sought-after for future applications.

- Ultimately, heterostructures were grown fulfilling all requirements postulated in section 2.1. Direct bandgap GeSn was combined with SiGeSn ternaries to form different types of heterostructures, that are double heterostructures (DHS) and multi quantum wells (MQW). All layers show a high crystalline quality and their adaptability as light emitters.

- The necessity of a thick emission layer in the DHS design makes it difficult to avert the formation of additional defects at the active region. Therefore, the approach using GeSn/SiGeSn MQW structures is much more beneficial for future efficient group IV light emitters. Emission from quantized states was demonstrated, proving potential future benefits in lasers from the two-dimensional carrier density of states.

- Finally, the integratability of GeSn-based materials with other Si-based components was experimentally shown. Fully CMOS-compatible processing of an integrated light source was achieved, further amplifying the potential of Sn-based emitters in future *opto-electronic integrated circuits* (OEICs).

6 Conclusion & Outlook

Within the frame of this thesis, epitaxial growth of Sn-based group IV alloys was investigated, targeting for direct bandgap heterostructure light emitters. Lessons learned from the successful history of III-V emitters allowed identification of a number of necessary requirements:

- GeSn alloys require high Sn contents ($> 10\,$at.%), well above the solid solubility limit.
- Layers need to be free from internal strain from lattice mismatch to the substrate to sustain their fundamental direct bandgap.
- SiGeSn ternaries with Si concentrations in the order of several at.% are necessary to obtain confinement of carriers in GeSn/SiGeSn heterostructures.

Numerous GeSn samples were grown in a *chemical vapor deposition* (CVD) reactor on (Ge-buffered and blank) Si wafers at temperatures below 400 °C. Investigations towards direct bandgap GeSn alloys required studying the influence of several growth parameters, such as precursor flows and growth temperature, on the structural, morphological and optical properties of grown films. Two strategies for tuning of incorporated Sn contents were found. Reducing growth temperature allows strongly elevated Sn incorporation (up to 12 at.% at 340 °C for fully strained layers), as phase separation in these meta-stable alloys by Sn segregation can be kinetically suppressed. At a given temperature, composition can be adjusted within a certain range of a few at.% by simultaneous tuning of both, digermane and tin tetrachloride precursor flows.

Epitaxy of strain relaxed layers was demonstrated by layers grown well above the critical thickness for strain relaxation. Relaxation and the accompanied lattice dilation allowed even slightly higher concentrations of substitutional Sn of up to 14 at.%.

Alloys with thicknesses up to 1 µm relax plastically by formation of a dense misfit dislocation network at the GeSn/Ge interface. However, these defects are mainly confined at the interface and even penetrate into the Ge-VS, at least up to several hundred nm thickness. Optical characterization of strain-relaxed films reveal tunable direct bandgaps in the *short-wave infrared*. Overall, the material system offers a wavelength range between 2 µm (0.60 eV) and 3.4 µm (0.37 eV) for a multitude of photonic applications. In particular, strong photoluminescence at room temperature and down to 4 K have been observed and used for a better theoretical description of temperature dependent band positions.

Aiming for more complex heterostructures, epitaxy of SiGeSn ternaries was also investigated. Compositional tuning by growth temperature was accomplished, yielding Si and Sn concentrations of up to 14 at.%, respectively, in a range between 425 °C and 340 °C. The incorporation of such high Si concentrations in this low-temperature window enables even more degrees of freedom in design and epitaxy of heterostructures, as (Γ-) band positions even above bulk Ge (0.8 eV) can be reached.

An unusually large and composition dependent optical bandgap bowing parameter (b_{SiSn}) was found in high-Sn content ternaries and were linked to a non-homogeneous distribution of Si atoms within an otherwise (Ge & Sn atoms) perfectly random solid solution.

Including also in-situ doping, epitaxy of several GeSn-based light emitting diodes (LEDs) was proven possible. Starting from simple homojunction diodes, room temperature electroluminescence of light emitters (8.5–12.5 at.% Sn) between 2.25 µm and 2.63 µm was shown. Moving towards more complex heterostructures, multi quantum well (MQW) LEDs were formed from GeSn binaries with $\sim$ 8 at.% (thus slightly indirect), using Ge as well as SiGeSn barriers. Comparison of emission behavior found strongly enhanced efficiency for ternary barriers, originating in their improved carrier confinement.

Finally, complex heterostructures were grown, demonstrating the combination of direct bandgap GeSn alloys and SiGeSn ternaries in double heterostructures and MQWs. A high crystalline and structural quality as well as perfect Ge and Sn distributions in the MQW were demonstrated by *atom probe tomography* and *dark field electron holography*. Strongly enhanced light emission, especially from MQW structures, proved their superiority compared to bulk layers. This originates mainly from an improved confinement of carriers far away from defective interfaces, while emission from quantized states was identified as possible path towards advanced enhancements.

Processing of GeSn material offered realization of several integrated optical components, such as waveguides, grating couplers and multi mode interferometers.

These findings open several paths for future group IV-based *optoelectronic integrated circuits* (OEIC). In those, the most pressing issue would be the realization of an integrated light source. Incorporation of in-situ doped carrier injection layers into demonstrated direct bandgap heterostructures will surely be able to bring highly efficient room temperature light emitters. Aiming even further, it may also enable realization of electrically-pumped lasers, which have not yet been demonstrated from Sn-based group IV alloys even at cryogenic temperatures. However, there are several future optimizations possibly needed to reach this goal. They comprise the increase of Si in the barriers, since carrier leakage out of the active region and their non-radiative recombination at defective interfaces currently limits room temperature emission. Furthermore, the amount of Sn in the active GeSn shall be enhanced further to elevate the number of available carriers at the direct Γ valley.

The demonstrated heterostructure approach is, however, not limited to light emitters. All types of applications that profit from confined carriers will benefit from such structures, including photodetectors or electro-optical modulators. In the realm of nanoelectronics for example, low bandgap heterostructures may be used in *tunneling field effect transistors* (TFETs) to boost the tunneling current and suppress ambipolarity and leakage currents.

Therefore, future maturing of the (Si)Ge(Sn) system may one day allow seamless integration of opto- and nanoelectronics, upholding the successful history of Si-based integrated circuits.

A Appendix

XRD $\theta - 2\theta$ scan of pseudomorphic $Ge_{0.88}Sn_{0.12}$

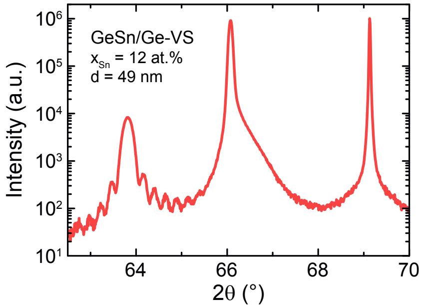

Figure A.1 – XRD $\theta - 2\theta$ scan of $Ge_{0.88}Sn_{0.12}$. Regular thickness fringes indicate a coherently grown layer with smooth interfaces. C.f. section 3.2.2 on page 29.

Growth kinetics of SiGeSn ternaries

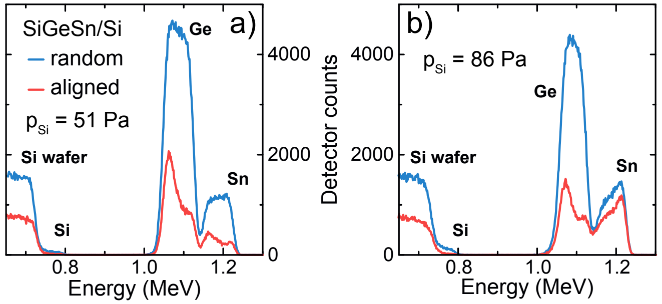

Figure A.2 – RBS spectra of two SiGeSn ternaries with fixed precursor partial pressures of $p_{Ge} = 55\,Pa$ & $p_{Sn} = 0.61\,Pa$. p_{Si} is chosen to 51 Pa a) or 86 Pa b). For highest Si flows, Sn atoms are not built-in homogeneously anymore and layer quality degrades. C.f. section 4.1.1 on page 53.

Optical characterization of SiGeSn ternaries

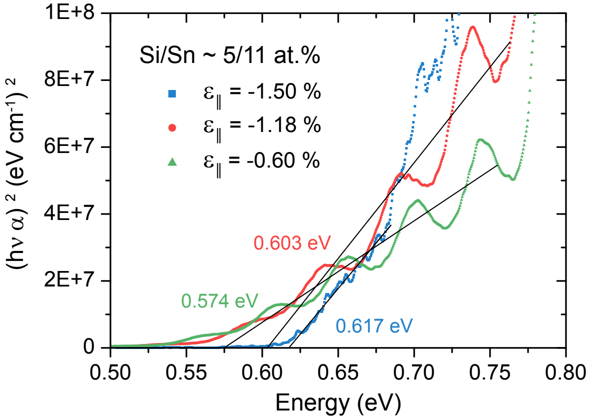

Figure A.3 – Determination of direct Γ valley position from a Tauc plot. Strain relaxation in samples with constant composition lead to a redshift of the direct bandgap. Exact determination is, however, impeded by thickness fringes in the region of interest. C.f. section 4.2.1 on page 61.

Atom probe tomography (APT) Methodology:

Atom probe tomography (APT) was employed for detailed compositional analysis of individual layers and their interfaces of GeSn/SiGeSn multi quantum well heterostructures. APT specimens were prepared using a dual-beam focused-ion-beam (FIB) system (FEI Helios Nanolab 600i) by the conventional lift-out technique.[250] APT analyses were performed using a reflectron-equipped local electrode atom probe tool (LEAP 4000X HR, Cameca Instruments) in laser mode with pulse frequency of 200 kHz, pulse energy of 20–30 pJ and detection rate of 0.01 ions per pulse, while the specimen base temperature was kept at 50–60 K. Data reconstruction and analysis was performed using the Cameca IVAS 3.6.8 software package. Reconstruction parameters (specimen shank angle, evaporation field and image compression factor) were adjusted to obtain flat layers with the correct thicknesses. Low mass spectrum background (5 ppm ns^{-1}), low fraction of multiple detector events (3 %) and absence of concentration changes with variation of analysis parameters ensured accurate compositional quantification.

Bibliography

[1] L. Vivien. "Computer technology: Silicon chips lighten up". In: *Nature* 528 (Dec. 2015), pp. 483–484. DOI: `10.1038/528483a`.

[2] D. A. Miller. "Rationale and challenges for optical interconnects to electronic chips". In: *Proceedings of the IEEE* 88.6 (June 2000), pp. 728–749. DOI: `10.1109/5.867687`.

[3] R. Kirchain and L. C. Kimerling. "A roadmap for nanophotonics". In: *Nature Photonics* 1.6 (June 2007), pp. 303–305. DOI: `10.1038/nphoton.2007.84`.

[4] Cisco. *Cisco Visual Networking Index: Forecast and Methodology, 2016-2021 (White Paper)*. 2017.

[5] Y. LeCun, Y. Bengio, and G. Hinton. "Deep learning". In: *Nature* 521.7553 (May 2015), pp. 436–444. DOI: `10.1038/nature14539`.

[6] J. J. Ackert, D. J. Thomson, L. Shen, A. C. Peacock, P. E. Jessop, G. T. Reed, G. Z. Mashanovich, and A. P. Knights. "High-speed detection at two micrometres with monolithic silicon photodiodes". In: *Nature Photonics* 9.6 (May 2015), pp. 393–396. DOI: `10.1038/nphoton.2015.81`.

[7] J. Michel, J. Liu, and L. C. Kimerling. "High-performance Ge-on-Si photodetectors". In: *Nature Photonics* 4.8 (Aug. 2010), pp. 527–534. DOI: `10.1038/nphoton.2010.157`.

[8] Q. Xu, B. Schmidt, S. Pradhan, and M. Lipson. "Micrometre-scale silicon electro-optic modulator". In: *Nature* 435.7040 (May 2005), pp. 325–327. DOI: `10.1038/nature03569`.

[9] C. Haffner, W. Heni, Y. Fedoryshyn, J. Niegemann, A. Melikyan, D. L. Elder, B. Baeuerle, Y. Salamin, A. Josten, U. Koch, C. Hoessbacher, F. Ducry, L. Juchli, A. Emboras, D. Hillerkuss, M. Kohl, L. R. Dalton, C. Hafner, and J. Leuthold. "All-plasmonic Mach-Zehnder modulator enabling optical high-speed communication at the microscale". In: *Nature Photonics* 9.8 (July 2015), pp. 525–528. DOI: `10.1038/nphoton.2015.127`.

[10] P. Chaisakul, D. Marris-Morini, J. Frigerio, D. Chrastina, M.-S. Rouifed, S. Cecchi, P. Crozat, G. Isella, and L. Vivien. "Integrated germanium optical interconnects on silicon substrates". In: *Nature Photonics* 8.6 (May 2014), pp. 482–488. DOI: `10.1038/nphoton.2014.73`.

[11] C. Sun, M. T. Wade, Y. Lee, J. S. Orcutt, L. Alloatti, M. S. Georgas, A. S. Waterman, J. M. Shainline, R. R. Avizienis, S. Lin, B. R. Moss, R. Kumar, F. Pavanello, A. H. Atabaki, H. M. Cook, A. J. Ou, J. C. Leu, Y.-H. Chen, K. Asanović, R. J. Ram, M. A. Popović, and V. M. Stojanović. "Single-chip microprocessor that communicates directly using light". In: *Nature* 528.7583 (Dec. 2015), pp. 534–538. DOI: `10.1038/nature16454`.

[12] A. W. Fang, H. Park, O. Cohen, R. Jones, M. J. Paniccia, and J. E. Bowers. "Electrically pumped hybrid AlGaInAs-silicon evanescent laser". In: *Optics Express* 14.20 (2006), p. 9203. DOI: `10.1364/OE.14.009203`.

[13] Z. Wang, B. Tian, M. Pantouvaki, W. Guo, P. Absil, J. Van Campenhout, C. Merckling, and D. Van Thourhout. "Room-temperature InP distributed feedback laser array directly grown on silicon". In: *Nature Photonics* 9.12 (Oct. 2015), pp. 837–842. DOI: `10.1038/nphoton.2015.199`. arXiv: `1501.03025`.

[14] B. Tian, Z. Wang, M. Pantouvaki, P. Absil, J. Van Campenhout, C. Merckling, and D. Van Thourhout. "Room Temperature O-band DFB Laser Array Directly Grown on (001) Silicon". In: *Nano Letters* 17.1 (Jan. 2017), pp. 559–564. DOI: `10.1021/acs.nanolett.6b04690`.

[15] S. Chen, W. Li, J. Wu, Q. Jiang, M. Tang, S. Shutts, S. N. Elliott, A. Sobiesierski, A. J. Seeds, I. Ross, P. M. Smowton, and H. Liu. "Electrically

pumped continuous-wave III-V quantum dot lasers on silicon". In: *Nature Photonics* 10.5 (Mar. 2016), pp. 307–311. DOI: `10.1038/nphoton.2016.21`.

[16] M. J. Süess, R. Geiger, R. A. Minamisawa, G. Schiefler, J. Frigerio, D. Chrastina, G. Isella, R. Spolenak, J. Faist, and H. Sigg. "Analysis of enhanced light emission from highly strained germanium microbridges". In: *Nature Photonics* 7.6 (Apr. 2013), pp. 466–472. DOI: `10.1038/nphoton.2013.67`.

[17] A. Gassenq, K. Guilloy, G. Osvaldo Dias, N. Pauc, D. Rouchon, J.-M. Hartmann, J. Widiez, S. Tardif, F. Rieutord, J. Escalante, I. Duchemin, Y.-M. Niquet, R. Geiger, T. Zabel, H. Sigg, J. Faist, A. Chelnokov, V. Reboud, and V. Calvo. "1.9% bi-axial tensile strain in thick germanium suspended membranes fabricated in optical germanium-on-insulator substrates for laser applications". In: *Applied Physics Letters* 107.19 (Nov. 2015), p. 191904. DOI: `10.1063/1.4935590`.

[18] S. Wirths, R. Geiger, N. von den Driesch, G. Mussler, T. Stoica, S. Mantl, Z. Ikonić, M. Luysberg, S. Chiussi, J.-M. Hartmann, H. Sigg, J. Faist, D. Buca, and D. Grützmacher. "Lasing in direct-bandgap GeSn alloy grown on Si". In: *Nature Photonics* 9.2 (Jan. 2015), pp. 88–92. DOI: `10.1038/nphoton.2014.321`.

[19] D. Stange, S. Wirths, R. Geiger, C. Schulte-Braucks, B. Marzban, N. von den Driesch, G. Mussler, T. Zabel, T. Stoica, J.-M. Hartmann, S. Mantl, Z. Ikonić, D. Grützmacher, H. Sigg, J. Witzens, and D. Buca. "Optically Pumped GeSn Microdisk Lasers on Si". In: *ACS Photonics* 3.7 (July 2016), pp. 1279–1285. DOI: `10.1021/acsphotonics.6b00258`.

[20] V. Reboud, A. Gassenq, N. Pauc, J. Aubin, L. Milord, Q. M. Thai, M. Bertrand, K. Guilloy, D. Rouchon, J. Rothman, T. Zabel, F. Armand Pilon, H. Sigg, A. Chelnokov, J. M. Hartmann, and V. Calvo. "Optically pumped GeSn micro-disks with 16% Sn lasing at 3.1 μm up to 180 K". In: *Applied Physics Letters* 111.9 (Aug. 2017), p. 092101. DOI: `10.1063/1.5000353`. arXiv: `1704.06436`.

[21] S. Al-Kabi, S. A. Ghetmiri, J. Margetis, T. Pham, Y. Zhou, W. Dou, B. Collier, R. Quinde, W. Du, A. Mosleh, J. Liu, G. Sun, R. A. Soref, J. Tolle,

B. Li, M. Mortazavi, H. A. Naseem, and S.-Q. Yu. “An optically pumped 2.5 μm GeSn laser on Si operating at 110 K”. In: *Applied Physics Letters* 109.17 (Oct. 2016), p. 171105. DOI: `10.1063/1.4966141`.

[22] J. D. Sau and M. L. Cohen. “Possibility of increased mobility in Ge-Sn alloy system”. In: *Physical Review B* 75.4 (Jan. 2007), p. 045208. DOI: `10.1103/PhysRevB.75.045208`.

[23] R. Pandey, C. Schulte-Braucks, R. N. Sajjad, M. Barth, R. K. Ghosh, B. Grisafe, P. Sharma, N. von den Driesch, A. Vohra, B. Rayner, R. Loo, S. Mantl, D. Buca, C. C. Yeh, C. H. Wu, W. Tsai, D. Antoniadis, and S. Datta. “Performance Benchmarking of p-type $In_{0.65}Ga_{0.35}As/GaAs_{0.4}Sb_{0.6}$ and $Ge/Ge_{0.93}Sn_{0.07}$ Hetero-junction Tunnel FETs”. In: *Technical Digest - International Electron Devices Meeting, IEDM* (2017), pp. 19.6.1–19.6.4. DOI: `10.1109/IEDM.2016.7838455`.

[24] A. M. Ionescu and H. Riel. “Tunnel field-effect transistors as energy-efficient electronic switches”. In: *Nature* 479.7373 (Nov. 2011), pp. 329–337. DOI: `10.1038/nature10679`.

[25] J. Juan-Colás, A. Parkin, K. E. Dunn, M. G. Scullion, T. F. Krauss, and S. D. Johnson. “The electrophotonic silicon biosensor”. In: *Nature Communications* 7 (2016), p. 12769. DOI: `10.1038/ncomms12769`.

[26] M. Sieger and B. Mizaikoff. “Toward On-Chip Mid-Infrared Sensors”. In: *Analytical Chemistry* 88.11 (June 2016), pp. 5562–5573. DOI: `10.1021/acs.analchem.5b04143`.

[27] R. Soref. “Group IV photonics: Enabling 2 μm communications”. In: *Nature Photonics* 9.6 (May 2015), pp. 358–359. DOI: `10.1038/nphoton.2015.87`.

[28] R. Soref, D. Buca, and S.-Q. Yu. “Group IV Photonics - Driving Integrated Optoelectronics”. In: *Optics & Photonics News* 27.1 (2016), pp. 32–39. DOI: `10.1364/OPN.27.1.000032`.

[29] S. Wirths. “Group IV Epitaxy for Advanced Nano- and Optoelectronic Applications”. Doctoral Thesis. RWTH Aachen, 2015.

[30] C. Goodman. “Direct-gap group IV semiconductors based on tin”. In: *IEE Proceedings I Solid State and Electron Devices* 129.5 (1982), p. 189. DOI: `10.1049/ip-i-1.1982.0043`.

[31] S. Oguz, W. Paul, T. F. Deutsch, B.-Y. Tsaur, and D. Murphy. “Synthesis of metastable, semiconducting Ge-Sn alloys by pulsed UV laser crystallization”. In: *Applied Physics Letters* 43.9 (Nov. 1983), pp. 848–850. DOI: `10.1063/1.94524`.

[32] P. Moontragoon, Z. Ikonić, and P. Harrison. “Band structure calculations of Si-Ge-Sn alloys: achieving direct band gap materials”. In: *Semiconductor Science and Technology* 22.7 (July 2007), pp. 742–748. DOI: `10.1088/0268-1242/22/7/012`.

[33] R. W. Olesinski and G. J. Abbaschian. “The Ge–Sn (Germanium–Tin) system”. In: *Bulletin of Alloy Phase Diagrams* 5.3 (June 1984), pp. 265–271. DOI: `10.1007/BF02868550`.

[34] S. Groves and W. Paul. “Band Structure of Gray Tin”. In: *Physical Review Letters* 11.5 (Sept. 1963), pp. 194–196. DOI: `10.1103/PhysRevLett.11.194`.

[35] P. R. Wallace. “The Band Theory of Graphite”. In: *Physical Review* 71.9 (May 1947), pp. 622–634. DOI: `10.1103/PhysRev.71.622`.

[36] S. Golin. “Band Structure of Bismuth: Pseudopotential Approach”. In: *Physical Review* 166.3 (Feb. 1968), pp. 643–651. DOI: `10.1103/PhysRev.166.643`.

[37] K. Lu Low, Y. Yang, G. Han, W. Fan, and Y.-C. Yeo. “Electronic band structure and effective mass parameters of $\mathrm{Ge}_{1-x}\mathrm{Sn}_x$ alloys”. In: *Journal of Applied Physics* 112.10 (2012), p. 103715. DOI: `10.1063/1.4767381`.

[38] S. Gupta, R. Chen, B. Vincent, D. Lin, B. Magyari-köpe, M. Caymax, J. Dekoster, J. S. Harris, Y. Nishi, and K. C. Saraswat. “GeSn Channel n and p MOSFETs”. In: *ECS Transactions* 50.9 (2012), pp. 937–941. DOI: `10.1149/05009.0937ecst`.

[39] M. P. Polak, P. Scharoch, and R. Kudrawiec. “The electronic band structure of $Ge_{1-x}Sn_x$ in the full composition range: indirect, direct, and inverted gaps regimes, band offsets, and the Burstein-Moss effect”. In: *Journal of Physics D: Applied Physics* 50.19 (May 2017), p. 195103. DOI: `10.1088/1361-6463/aa67bf`.

[40] H.-S. Lan, S. T. Chang, and C. W. Liu. “Semiconductor, topological semimetal, indirect semimetal, and topological Dirac semimetal phases of $Ge_{1-x}Sn_x$ alloys”. In: *Physical Review B* 95.20 (May 2017), p. 201201. DOI: `10.1103/PhysRevB.95.201201`.

[41] X. Chen, L. Li, and M. Zhao. “Hydrogenation-induced large-gap quantum-spin-Hall insulator states in a germanium–tin dumbbell structure”. In: *RSC Advances* 5.89 (2015), pp. 72462–72468. DOI: `10.1039/C5RA10712A`.

[42] P. Moontragoon, R. A. Soref, and Z. Ikonić. “The direct and indirect bandgaps of unstrained $Si_xGe_{1-x-y}Sn_y$ and their photonic device applications”. In: *Journal of Applied Physics* 112.7 (2012), p. 073106. DOI: `10.1063/1.4757414`.

[43] G. Sun, R. A. Soref, and H. H. Cheng. “Design of a Si-based lattice-matched room-temperature GeSn/GeSiSn multi-quantum-well mid-infrared laser diode.” In: *Optics express* 18.19 (2010), pp. 19957–19965. DOI: `10.1364/OE.18.019957`.

[44] G.-E. Chang, S.-W. Chang, and S. L. Chuang. “Strain-Balanced Ge_zSn_{1-z}/$Si_xGe_ySn_{1-x-y}$ Multiple-Quantum-Well Lasers”. In: *IEEE Journal of Quantum Electronics* 46.12 (Dec. 2010), pp. 1813–1820. DOI: `10.1109/JQE.2010.2059000`.

[45] J. R. Chelikowsky and M. L. Cohen. “Nonlocal pseudopotential calculations for the electronic structure of eleven diamond and zinc-blende semiconductors”. In: *Physical Review B* 14.2 (1976), pp. 556–582. DOI: `10.1103/PhysRevB.14.556`.

[46] W. L. Bond. “Precision lattice constant determination”. In: *Acta Crystallographica* 13.10 (1960), pp. 814–818. DOI: `10.1107/S0365110X60001941`.

[47] T. Hom, W. Kiszenik, and B. Post. “Accurate lattice constants from multiple reflection measurements. II. Lattice constants of germanium silicon, and diamond”. In: *Journal of Applied Crystallography* 8.4 (Aug. 1975), pp. 457–458. DOI: `10.1107/S0021889875010965`.

[48] J. Thewlis and A. R. Davey. “Thermal Expansion of Grey Tin”. In: *Nature* 174.4439 (Nov. 1954), pp. 1011–1011. DOI: `10.1038/1741011a0`.

[49] M. Jaros. “Electronic properties of semiconductor alloy systems”. In: *Reports on Progress in Physics* 48.8 (Aug. 1985), pp. 1091–1154. DOI: `10.1088/0034-4885/48/8/001`.

[50] V. R. D’Costa, C. S. Cook, J. Menéndez, J. Tolle, J. Kouvetakis, and S. Zollner. “Transferability of optical bowing parameters between binary and ternary group-IV alloys”. In: *Solid State Communications* 138.6 (May 2006), pp. 309–313. DOI: `10.1016/j.ssc.2006.02.023`.

[51] C. Eckhardt, K. Hummer, and G. Kresse. “Indirect-to-direct gap transition in strained and unstrained $\mathrm{Sn}_x\mathrm{Ge}_{1-x}$ alloys”. In: *Physical Review B* 89.16 (Apr. 2014), p. 165201. DOI: `10.1103/PhysRevB.89.165201`.

[52] W.-J. Yin, X.-G. Gong, and S.-H. Wei. “Origin of the unusually large band-gap bowing and the breakdown of the band-edge distribution rule in the $\mathrm{Sn}_x\mathrm{Ge}_{1-x}$ alloys”. In: *Physical Review B* 78.16 (Oct. 2008), p. 161203. DOI: `10.1103/PhysRevB.78.161203`.

[53] S. Gupta, B. Magyari-Köpe, Y. Nishi, and K. C. Saraswat. “Achieving direct band gap in germanium through integration of Sn alloying and external strain”. In: *Journal of Applied Physics* 113.7 (2013), p. 073707. DOI: `10.1063/1.4792649`.

[54] T. B. Bahder. “Eight-band kp model of strained zinc-blende crystals”. In: *Physical Review B* 41.17 (1990), pp. 11992–12001.

[55] T. B. Bahder. “Erratum: Eight-band kp model of strained zinc-blende crystals”. In: *Physical Review B* 46.15 (1992), p. 9913.

[56] P. Moontragoon, V. Nenad, Z. Ikonić, and P. Harrison. “Electronic structure and optical properties of Sn and SnGe quantum dots”. In: *Journal of Applied Physics* 103.10 (2008), p. 103712. DOI: `10.1063/1.2932169`.

[57] M. El Kurdi, G. Fishman, S. Sauvage, and P. Boucaud. “Band structure and optical gain of tensile-strained germanium based on a 30 band k·p formalism”. In: *Journal of Applied Physics* 107.1 (2010), p. 013710. DOI: `10.1063/1.3279307`.

[58] M. Virgilio, C. L. Manganelli, G. Grosso, G. Pizzi, and G. Capellini. “Radiative recombination and optical gain spectra in biaxially strained n-type germanium”. In: *Physical Review B* 87.23 (June 2013), p. 235313. DOI: `10.1103/PhysRevB.87.235313`.

[59] A. Attiaoui and O. Moutanabbir. “Indirect-to-direct band gap transition in relaxed and strained $\mathrm{Ge}_{1-x-y}\mathrm{Si}_x\mathrm{Sn}_y$ ternary alloys”. In: *Journal of Applied Physics* 116.6 (Aug. 2014), p. 063712. DOI: `10.1063/1.4889926`.

[60] M. T. Asom, E. A. Fitzgerald, A. R. Kortan, B. Spear, and L. C. Kimerling. “Epitaxial growth of metastable SnGe alloys”. In: *Applied Physics Letters* 55.6 (Aug. 1989), pp. 578–579. DOI: `10.1063/1.101838`. arXiv: `arXiv:1011.1669v3`.

[61] G. He and H. A. Atwater. “Interband Transitions in $\mathrm{Sn}_x\mathrm{Ge}_{1-x}$ Alloys”. In: *Physical Review Letters* 79.10 (1997), pp. 1937–1940. DOI: `10.1063/1.4829697`.

[62] M. Oehme, K. Kostecki, M. Schmid, F. Oliveira, E. Kasper, and J. Schulze. “Epitaxial growth of strained and unstrained GeSn alloys up to 25% Sn”. In: *Thin Solid Films* 557 (Apr. 2014), pp. 169–172. DOI: `10.1016/j.tsf.2013.10.064`.

[63] R. Chen, H. Lin, Y. Huo, C. Hitzman, T. I. Kamins, and J. S. Harris. “Increased photoluminescence of strain-reduced, high-Sn composition $\mathrm{Ge}_{1-x}\mathrm{Sn}_x$ alloys grown by molecular beam epitaxy”. In: *Applied Physics Letters* 99.18 (2011), p. 181125. DOI: `10.1063/1.3658632`.

[64] T. Asano, S. Kidowaki, M. Kurosawa, N. Taoka, O. Nakatsuka, and S. Zaima. "Influence of Ge substrate orientation on crystalline structures of $Ge_{1-x}Sn_x$ epitaxial layers". In: *Thin Solid Films* 557 (Apr. 2014), pp. 159–163. DOI: `10.1016/j.tsf.2013.10.087`.

[65] V. Schlykow, W. M. Klesse, G. Niu, N. Taoka, Y. Yamamoto, O. Skibitzki, M. R. Barget, P. Zaumseil, H. von Känel, M. A. Schubert, G. Capellini, and T. Schroeder. "Selective growth of fully relaxed GeSn nano-islands by nanoheteroepitaxy on patterned Si(001)". In: *Applied Physics Letters* 109.20 (Nov. 2016), p. 202102. DOI: `10.1063/1.4967500`.

[66] J. P. Gupta, N. Bhargava, S. Kim, T. Adam, and J. Kolodzey. "Infrared electroluminescence from GeSn heterojunction diodes grown by molecular beam epitaxy". In: *Applied Physics Letters* 102.25 (2013), p. 251117. DOI: `10.1063/1.4812747`.

[67] W. Wang, Q. Zhou, Y. Dong, E. S. Tok, and Y.-C. Yeo. "Critical thickness for strain relaxation of $Ge_{1-x}Sn_x$ (x $<$ 0.17) grown by molecular beam epitaxy on Ge(001)". In: *Applied Physics Letters* 106.23 (June 2015), p. 232106. DOI: `10.1063/1.4922529`.

[68] Y. Sadofyev, V. Martovitsky, A. Klekovkin, V. Saraikin, and I. Vasil'evskii. "Thermal Stability of Ge/GeSn Nanostructures Grown by MBE on (001) Si/Ge Virtual Wafers". In: *Physics Procedia* 72.February (2015), pp. 411–418. DOI: `10.1016/j.phpro.2015.09.078`.

[69] S. I. Shah, J. E. Greene, L. L. Abels, Q. Yao, and P. M. Raccah. "Growth of single-crystal metastable $Ge_{1-x}Sn_x$ alloys on Ge(100) and GaAs(100) substrates". In: *Journal of Crystal Growth* 83.1 (1987), pp. 3–10. DOI: `10.1016/0022-0248(87)90495-7`.

[70] J. Zheng, L. Li, T. Zhou, Y. Zuo, C. Li, B. Cheng, and Q. Wang. "Growth of Crystalline $Ge_{1-x}Sn_x$ Films on Si (100) by Magnetron Sputtering". In: *ECS Solid State Letters* 3.9 (July 2014), P111–P113. DOI: `10.1149/2.0081409ssl`.

[71] R. R. Lieten, J. W. Seo, S. Decoster, A. Vantomme, S. Peters, K. C. Bustillo, E. E. Haller, M. Menghini, and J.-P. Locquet. "Tensile strained GeSn on Si by

solid phase epitaxy”. In: *Applied Physics Letters* 102.5 (Feb. 2013), p. 052106. DOI: `10.1063/1.4790302`.

[72] C.-W. Lee, Y.-H. Wu, C.-H. Hsieh, and C.-C. Lin. “Epitaxial GeSn film formed by solid phase epitaxy and its application to Yb_2O_3-gated GeSn metal-oxide-semiconductor capacitors with sub-nm equivalent oxide thickness”. In: *Applied Physics Letters* 105.20 (Nov. 2014), p. 203508. DOI: `10.1063/1.4902119`.

[73] S. Stefanov, J. C. Conde, A. Benedetti, C. Serra, J. Werner, M. Oehme, J. Schulze, D. Buca, B. Holländer, S. Mantl, and S. Chiussi. “Silicon germanium tin alloys formed by pulsed laser induced epitaxy”. In: *Applied Physics Letters* 100.20 (May 2012), p. 204102. DOI: `10.1063/1.4714768`.

[74] H. Li, J. Brouillet, A. Salas, X. Wang, and J. Liu. “Low temperature growth of high crystallinity GeSn on amorphous layers for advanced optoelectronics”. In: *Optical Materials Express* 3.9 (Sept. 2013), p. 1385. DOI: `10.1364/OME.3.001385`.

[75] L. Jin, D. Zhang, H. Zhang, J. Fang, Y. Liao, T. Zhou, C. Liu, Z. Zhong, and V. G. Harris. “Large area Germanium Tin nanometer optical film coatings on highly flexible aluminum substrates”. In: *Scientific Reports* 6.1 (Dec. 2016), p. 34030. DOI: `10.1038/srep34030`.

[76] K. Toko, N. Oya, N. Saitoh, N. Yoshizawa, and T. Suemasu. “70°C synthesis of high-Sn content (25%) GeSn on insulator by Sn-induced crystallization of amorphous Ge”. In: *Applied Physics Letters* 106.8 (Feb. 2015), p. 082109. DOI: `10.1063/1.4913744`.

[77] K. Bratland, Y. Foo, P. Desjardins, and J. E. Greene. “Sn-enhanced epitaxial thickness during low-temperature Ge(001) molecular-beam epitaxy”. In: *Applied Physics Letters* 82.24 (2003), p. 4247. DOI: `10.1063/1.1578712`.

[78] K. Ramasamy, P. G. Kotula, A. F. Fidler, M. T. Brumbach, J. M. Pietryga, and S. A. Ivanov. “Sn_xGe_{1-x} Alloy Nanocrystals: A First Step toward Solution-Processed Group IV Photovoltaics”. In: *Chemistry of Materials* 27.13 (July 2015), pp. 4640–4649. DOI: `10.1021/acs.chemmater.5b01041`.

[79] K. Tamaru. “The Thermal Decomposition of Tin Hydride”. In: *The Journal of Physical Chemistry* 60.5 (May 1956), pp. 610–612. DOI: `10.1021/j150539a024`.

[80] J. Taraci, J. Tolle, J. Kouvetakis, M. R. McCartney, D. J. Smith, J. Menendez, and M. A. Santana. “Simple chemical routes to diamond-cubic germanium-tin alloys”. In: *Applied Physics Letters* 78.23 (June 2001), pp. 3607–3609. DOI: `10.1063/1.1376156`.

[81] M. Bauer, J. Taraci, J. Tolle, A. V. G. Chizmeshya, S. Zollner, D. J. Smith, J. Menendez, C. Hu, and J. Kouvetakis. “Ge-Sn semiconductors for band-gap and lattice engineering”. In: *Applied Physics Letters* 81.16 (Oct. 2002), pp. 2992–2994. DOI: `10.1063/1.1515133`.

[82] K. Suda, T. Uno, T. Miyakawa, H. Machida, M. Ishikawa, H. Sudo, Y. Ohshita, and A. Ogura. “GeSn Film Deposition Using Metal Organic Chemical Vapor Deposition”. In: *ECS Transactions* 53.1 (May 2013), pp. 245–250. DOI: `10.1149/05301.0245ecst`.

[83] Y. Inuzuka, S. Ike, T. Asano, W. Takeuchi, N. Taoka, O. Nakatsuka, and S. Zaima. “Epitaxial $\mathrm{Ge}_{1-x}\mathrm{Sn}_x$ Layers Grown by Metal-Organic Chemical Vapor Deposition Using Tertiary-butyl-germane and Tri-butyl-vinyl-tin”. In: *ECS Solid State Letters* 4.8 (June 2015), P59–P61. DOI: `10.1149/2.0041508ssl`.

[84] V. R. D’Costa, Y. Fang, J. Mathews, R. Roucka, J. Tolle, J. Menéndez, and J. Kouvetakis. “Sn-alloying as a means of increasing the optical absorption of Ge at the C- and L-telecommunication bands”. In: *Semiconductor Science and Technology* 24.11 (Nov. 2009), p. 115006. DOI: `10.1088/0268-1242/24/11/115006`.

[85] A. Mosleh, M. a. Alher, L. C. Cousar, W. Du, S. A. Ghetmiri, T. Pham, J. M. Grant, G. Sun, R. a. Soref, B. Li, H. a. Naseem, and S.-Q. Yu. “Direct Growth of $\mathrm{Ge}_{1-x}\mathrm{Sn}_x$ Films on Si Using a Cold-Wall Ultra-High Vacuum Chemical-Vapor-Deposition System”. In: *Frontiers in Materials* 2.April (Apr. 2015), pp. 1–7. DOI: `10.3389/fmats.2015.00030`.

[86] C. L. Senaratne, J. D. Gallagher, L. Jiang, T. Aoki, D. J. Smith, J. Menéndez, and J. Kouvetakis. “$Ge_{1-y}Sn_y$ (y = 0.01-0.10) alloys on Ge-buffered Si: Synthesis, microstructure, and optical properties”. In: *Journal of Applied Physics* 116.13 (2014), p. 133509. DOI: `10.1063/1.4896788`.

[87] B. Vincent, F. Gencarelli, H. Bender, C. Merckling, B. Douhard, D. H. Petersen, O. Hansen, H. H. Henrichsen, J. Meersschaut, W. Vandervorst, M. Heyns, R. Loo, and M. Caymax. “Undoped and in-situ B doped GeSn epitaxial growth on Ge by atmospheric pressure-chemical vapor deposition”. In: *Applied Physics Letters* 99.15 (2011), p. 152103. DOI: `10.1063/1.3645620`.

[88] H. H. Radamson, M. Noroozi, A. Jamshidi, P. E. Thompson, and M. Ostling. “Strain Engineering in GeSnSi Materials”. In: *ECS Transactions* 50.9 (Mar. 2013), pp. 527–531. DOI: `10.1149/05009.0527ecst`.

[89] F. Gencarelli, B. Vincent, L. Souriau, O. Richard, W. Vandervorst, R. Loo, M. Caymax, and M. Heyns. “Low-temperature Ge and GeSn Chemical Vapor Deposition using Ge_2H_6”. In: *Thin Solid Films* 520.8 (Feb. 2012), pp. 3211–3215. DOI: `10.1016/j.tsf.2011.10.119`.

[90] S. Wirths, D. Buca, G. Mussler, A. T. Tiedemann, B. Holländer, P. Bernardy, T. Stoica, D. Grutzmacher, and S. Mantl. “Reduced Pressure CVD Growth of Ge and $Ge_{1-x}Sn_x$ Alloys”. In: *ECS Journal of Solid State Science and Technology* 2.5 (Mar. 2013), N99–N102. DOI: `10.1149/2.006305jss`.

[91] R. Chen, Y.-C. Huang, S. Gupta, A. C. Lin, E. Sanchez, Y. Kim, K. C. Saraswat, T. I. Kamins, and J. S. Harris. “Material characterization of high Sn-content, compressively-strained GeSn epitaxial films after rapid thermal processing”. In: *Journal of Crystal Growth* 365 (Feb. 2013), pp. 29–34. DOI: `10.1016/j.jcrysgro.2012.12.014`.

[92] N. von den Driesch, D. Stange, S. Wirths, G. Mussler, B. Holländer, Z. Ikonić, J. M. Hartmann, T. Stoica, S. Mantl, D. Grützmacher, and D. Buca. “Direct bandgap group IV epitaxy on Si for laser applications”. In: *Chemistry of Materials* 27.13 (June 2015), pp. 4693–4702. DOI: `10.1021/acs.chemmater.5b01327`.

[93] J. Aubin, J. M. Hartmann, J. P. Barnes, J. B. Pin, and M. Bauer. "Very Low Temperature Epitaxy of Heavily In Situ Phosphorous Doped Ge Layers and High Sn Content GeSn Layers". In: *ECS Journal of Solid State Science and Technology* 6.1 (Dec. 2017), P21–P26. DOI: `10.1149/2.0091701jss`.

[94] J. Margetis, A. Mosleh, S. Al-Kabi, S. Ghetmiri, W. Du, W. Dou, M. Benamara, B. Li, M. Mortazavi, H. Naseem, S.-Q. Yu, and J. Tolle. "Study of low-defect and strain-relaxed GeSn growth via reduced pressure CVD in H_2 and N_2 carrier gas". In: *Journal of Crystal Growth* 463 (Apr. 2017), pp. 128–133. DOI: `10.1016/j.jcrysgro.2017.01.041`.

[95] S. Biswas, J. Doherty, D. Saladukha, Q. Ramasse, D. Majumdar, M. Upmanyu, A. Singha, T. Ochalski, M. A. Morris, and J. D. Holmes. "Non-equilibrium induction of tin in germanium: towards direct bandgap $Ge_{1-x}Sn_x$ nanowires". In: *Nature Communications* 7 (Apr. 2016), p. 11405. DOI: `10.1038/ncomms11405`.

[96] A. C. Meng, C. S. Fenrich, M. R. Braun, J. P. McVittie, A. F. Marshall, J. S. Harris, and P. C. McIntyre. "Core-Shell Germanium/Germanium-Tin Nanowires Exhibiting Room-Temperature Direct- and Indirect-Gap Photoluminescence". In: *Nano Letters* 16.12 (Dec. 2016), pp. 7521–7529. DOI: `10.1021/acs.nanolett.6b03316`.

[97] S. Assali, A. Dijkstra, A. Li, S. Koelling, M. A. Verheijen, L. Gagliano, N. von den Driesch, D. Buca, P. M. Koenraad, J. E. M. Haverkort, and E. P. A. M. Bakkers. "Growth and Optical Properties of Direct Band Gap $Ge/Ge_{0.87}Sn_{0.13}$ Core/Shell Nanowire Arrays". In: *Nano Letters* 17.3 (Feb. 2017), pp. 1538–1544. DOI: `10.1021/acs.nanolett.6b04627`.

[98] I. Fischer, T. Wendav, L. Augel, S. Jitpakdeebodin, F. Oliveira, A. Benedetti, S. Stefanov, S. Chiussi, G. Capellini, K. Busch, and J. Schulze. "Growth and characterization of SiGeSn quantum well photodiodes". In: *Optics Express* 23.19 (Sept. 2015), p. 25048. DOI: `10.1364/OE.23.025048`.

[99] S. Wirths, A. T. Tiedemann, Z. Ikonić, P. Harrison, B. Holländer, T. Stoica, G. Mussler, M. Myronov, J.-M. Hartmann, D. Grützmacher, D. Buca, and S. Mantl. "Band engineering and growth of tensile strained Ge/(Si)GeSn

heterostructures for tunnel field effect transistors". In: *Applied Physics Letters* 102.19 (2013), p. 192103. DOI: `10.1063/1.4805034`.

[100] R. T. Beeler, D. J. Smith, J. Kouvetakis, and J. Menendez. "GeSiSn Photodiodes With 1 eV Optical Gaps Grown on Si(100) and Ge(100) Platforms". In: *IEEE Journal of Photovoltaics* 2.4 (Oct. 2012), pp. 434–440. DOI: `10.1109/JPHOTOV.2012.2206568`.

[101] R. W. Olesinski and G. J. Abbaschian. "The Ge–Si (Germanium-Silicon) system". In: *Bulletin of Alloy Phase Diagrams* 5.2 (Apr. 1984), pp. 180–183. DOI: `10.1007/BF02868957`.

[102] J. P. Fleurial and A. Borshchevsky. "Si-Ge-Metal Ternary Phase Diagram Calculations". In: *Journal of The Electrochemical Society* 137 (1990), p. 2928. DOI: `10.1149/1.2087101`.

[103] T. F. Kuech, L. J. Mawst, and A. S. Brown. "Mixed Semiconductor Alloys for Optical Devices". In: *Annual Review of Chemical and Biomolecular Engineering* 4.1 (June 2013), pp. 187–209. DOI: `10.1146/annurev-chembioeng-061312-103359`.

[104] C. D. Thurmond, F. A. Trumbore, and M. Kowalchik. "Germanium Solidus Curves". In: *The Journal of Chemical Physics* 25.4 (1956), p. 799. DOI: `10.1063/1.1743083`.

[105] T. Tsukamoto, N. Hirose, A. Kasamatsu, T. Mimura, T. Matsui, and Y. Suda. "Investigation of Sn surface segregation during GeSn epitaxial growth by Auger electron spectroscopy and energy dispersive x-ray spectroscopy". In: *Applied Physics Letters* 106 (2015), p. 052103. DOI: `10.1063/1.4907863`.

[106] N. Taoka, T. Asano, T. Yamaha, T. Terashima, O. Nakatsuka, I. Costina, P. Zaumseil, G. Capellini, S. Zaima, and T. Schroeder. "Non-uniform depth distributions of Sn concentration induced by Sn migration and desorption during GeSnSi layer formation". In: *Applied Physics Letters* 106 (2015), p. 061107. DOI: `10.1063/1.4908121`.

[107] N. Taoka, G. Capellini, N. von den Driesch, D. Buca, P. Zaumseil, M. A. Schubert, W. M. Klesse, M. Montanari, and T. Schroeder. “Sn migration control at high temperature due to high deposition speed for forming high-quality GeSn layer”. In: *Applied Physics Express* 9.3 (Mar. 2016), p. 031201. DOI: `10.7567/APEX.9.031201`.

[108] H. Li, C. Chang, T. P. Chen, H. H. Cheng, Z. W. Shi, and H. Chen. “Characteristics of Sn segregation in Ge/GeSn heterostructures”. In: *Applied Physics Letters* 105.15 (Oct. 2014), p. 151906. DOI: `10.1063/1.4898583`.

[109] W. Dondl, G. Lütjering, W. Wegscheider, J. Wilhelm, R. Schorer, and G. Abstreiter. “Sn and Sb segregation and their possible use as surfactant for short-period Si/Ge superlattices”. In: *Journal of Crystal Growth* 127.1-4 (Feb. 1993), pp. 440–442. DOI: `10.1016/0022-0248(93)90656-H`.

[110] J. F. Nützel and G. Abstreiter. “Segregation and diffusion on semiconductor surfaces”. In: *Physical Review B* 53.20 (May 1996), pp. 13551–13558. DOI: `10.1103/PhysRevB.53.13551`.

[111] E. Kasper, J. Werner, M. Oehme, S. Escoubas, N. Burle, and J. Schulze. “Growth of silicon based germanium tin alloys”. In: *Thin Solid Films* 520.8 (Feb. 2012), pp. 3195–3200. DOI: `10.1016/j.tsf.2011.10.114`.

[112] S. Takeuchi, A. Sakai, O. Nakatsuka, M. Ogawa, and S. Zaima. “Tensile strained Ge layers on strain-relaxed $Ge_{1-x}Sn_x$/virtual Ge substrates”. In: *Thin Solid Films* 517.1 (Nov. 2008), pp. 159–162. DOI: `10.1016/j.tsf.2008.08.068`.

[113] K. Kato, T. Asano, N. Taoka, M. Sakashita, W. Takeuchi, O. Nakatsuka, and S. Zaima. “Robustness of Sn precipitation during thermal oxidation of $Ge_{1-x}Sn_x$ on Ge (001)”. In: *Japanese Journal of Applied Physics* 53 (2014), p. 08LD04.

[114] C. Fleischmann, R. R. Lieten, P. Hermann, P. Hönicke, B. Beckhoff, F. Seidel, O. Richard, H. Bender, Y. Shimura, S. Zaima, N. Uchida, K. Temst, W. Vandervorst, and A. Vantomme. “Thermal stability and relaxation mechanisms in compressively strained $Ge_{0.94}Sn_{0.06}$ thin films grown by molecular

beam epitaxy". In: *Journal of Applied Physics* 120.8 (Aug. 2016), p. 085309. DOI: `10.1063/1.4961396`.

[115] A. A. Tonkikh, N. D. Zakharov, A. A. Suvorova, C. Eisenschmidt, J. Schilling, and P. Werner. "Cubic phase Sn-rich GeSn nanocrystals in a Ge matrix". In: *Crystal Growth and Design* 14.4 (2014), pp. 1617–1622. DOI: `10.1021/cg401652f`.

[116] S. Roesgaard, J. Chevallier, P. I. Gaiduk, J. L. Hansen, P. B. Jensen, A. N. Larsen, A. Svane, P. Balling, and B. Julsgaard. "Light emission from silicon with tin-containing nanocrystals". In: *AIP Advances* 5.7 (2015), pp. 1–8. DOI: `10.1063/1.4926596`.

[117] D. Rainko, D. Stange, N. von den Driesch, C. Schulte-Braucks, G. Mussler, Z. Ikonić, J.-M. Hartmann, M. Luysberg, S. Mantl, D. Grützmacher, and D. Buca. "(Si)GeSn nanostructures for light emitters". In: *Silicon Photonics and Photonic Integrated Circuits V*. Ed. by L. Vivien, L. Pavesi, and S. Pelli. Vol. 9891. May 2016, 98910W. DOI: `10.1117/12.2227573`.

[118] P. I. Gaiduk, J. Lundsgaard Hansen, A. Nylandsted Larsen, F. L. Bregolin, and W. Skorupa. "Suppression of tin precipitation in SiSn alloy layers by implanted carbon". In: *Applied Physics Letters* 104.23 (June 2014), p. 231903. DOI: `10.1063/1.4882175`.

[119] Q. Liu, W. Geilei, Y. Guo, X. Ke, H. Radamson, H. Liu, C. Zhao, and J. Luo. "Improvement of the Thermal Stability of Nickel Stanogermanide by Carbon Pre-Stanogermanidation Implant into GeSn Substrate". In: *ECS Journal of Solid State Science and Technology* 4.3 (2014), P67–P70. DOI: `10.1149/2.0041503jss`.

[120] A. A. Williams, J. M. C. Thornton, J. E. Macdonald, R. G. van Silfhout, J. F. van der Veen, M. S. Finney, A. D. Johnson, and C. Norris. "Strain relaxation during the initial stages of growth in Ge/Si(001)". In: *Physical Review B* 43.6 (Feb. 1991), pp. 5001–5011. DOI: `10.1103/PhysRevB.43.5001`.

[121] J. Hartmann, A. Abbadie, N. Cherkashin, H. Grampeix, and L. Clavelier. "Epitaxial growth of Ge thick layers on nominal and 6° off Si(001); Ge surface

passivation by Si". In: *Semiconductor Science and Technology* 24.5 (May 2009), p. 055002. DOI: `10.1088/0268-1242/24/5/055002`.

[122] J. D. Cressler, ed. *Silicon Heterostructure Handbook: Materials, Fabrication, Devices, Circuits and Applications of SiGe and Si Strained-Layer Epitaxy.* CRC Press Inc., 2005.

[123] M. H. J. M. de Croon and L. Giling. "Chemical Boundary Layers in CVD I. Irreversible Reactions". In: *Journal of The Electrochemical Society* 137.9 (1990), pp. 2867–2876. DOI: `10.1149/1.2087090`.

[124] O. P. Karpenko and D. J. Eaglesham. "Surface roughening during low temperature Si(100) epitaxy". In: *Journal of Applied Physics* 82.3 (1997), pp. 1157–1165. DOI: `10.1063/1.365883`.

[125] K. Bratland, Y. Foo, J. Soares, T. Spila, P. Desjardins, and J. Greene. "Mechanism for epitaxial breakdown during low-temperature Ge(001) molecular beam epitaxy". In: *Physical Review B* 67.12 (2003), pp. 11–13. DOI: `10.1103/PhysRevB.67.125322`.

[126] T. R. Bramblett, Q. Lu, N.-E. Lee, N. Taylor, M.-A. Hasan, and J. E. Greene. "Ge(001) gas-source molecular beam epitaxy on Ge(001)2×1 and Si(001)2×1 from Ge_2H_6: Growth kinetics and surface roughening". In: *Journal of Applied Physics* 77.4 (Feb. 1995), pp. 1504–1513. DOI: `10.1063/1.358901`.

[127] J. Aubin, J. Hartmann, M. Bauer, and S. Moffatt. "Very low temperature epitaxy of Ge and Ge rich SiGe alloys with Ge_2H_6 in a Reduced Pressure-Chemical Vapour Deposition tool". In: *Journal of Crystal Growth* 445 (July 2016), pp. 65–72. DOI: `10.1016/j.jcrysgro.2016.04.018`.

[128] M. J. Almond, A. M. Doncaster, P. N. Noble, and R. Walsh. "Ge-H Bond Strengths in Germanes". In: *Journal of the American Chemical Society* 104 (1982), pp. 4717–4718. DOI: `10.1021/ja00381a054`.

[129] C. L. Senaratne, P. M. Wallace, J. D. Gallagher, P. E. Sims, J. Kouvetakis, and J. Menéndez. "Direct gap $Ge_{1-y}Sn_y$ alloys: Fabrication and design of mid-IR photodiodes". In: *Journal of Applied Physics* 120.2 (July 2016), p. 025701. DOI: `10.1063/1.4956439`.

[130] S. Wirths, D. Buca, Z. Ikonić, P. Harrison, A. T. Tiedemann, B. Holländer, T. Stoica, G. Mussler, U. Breuer, J.-M. Hartmann, D. Grützmacher, and S. Mantl. “SiGeSn growth studies using reduced pressure chemical vapor deposition towards optoelectronic applications”. In: *Thin Solid Films* 557 (Apr. 2014), pp. 183–187. DOI: `10.1016/j.tsf.2013.10.078`.

[131] K. Takahashi, A. Kunz, D. Woiki, and P. Roth. “Thermal Decomposition of Tin Tetrachloride Based on Cl- and Sn-Concentration Measurements”. In: *The Journal of Physical Chemistry A* 104.22 (June 2000), pp. 5246–5253. DOI: `10.1021/jp993985j`.

[132] W.-P. Huang, H. H. Cheng, G. Sun, R.-F. Lou, J. H. Yeh, and T.-M. Shen. “The characteristic of strain relaxation on SiGe virtual substrate with thermal annealing”. In: *Applied Physics Letters* 91.14 (Oct. 2007), p. 142102. DOI: `10.1063/1.2794016`.

[133] B. Holländer, S. Lenk, S. Mantl, H. Trinkaus, D. Kirch, M. Luysberg, T. Hackbarth, H.-J. Herzog, and P. Fichtner. “Strain relaxation of pseudomorphic $Si_{1-x}Ge_x$/Si(100) heterostructures after hydrogen or helium ion implantation for virtual substrate fabrication”. In: *Nuclear Instruments and Methods in Physics Research Section B: Beam Interactions with Materials and Atoms* 175-177 (Apr. 2001), pp. 357–367. DOI: `10.1016/S0168-583X(01)00559-6`.

[134] P. M. Petroff, R. A. Logan, and A. Savage. “Nonradiative recombination at dislocations in III-V compound semiconductors”. In: *Journal of Microscopy* 118.3 (Mar. 1980), pp. 255–261. DOI: `10.1111/j.1365-2818.1980.tb00272.x`.

[135] V. Higgs, F. Chin, X. Wang, J. Mosalski, and R. Beanland. “Photoluminescence characterization of defects in Si and SiGe structures”. In: *Journal of Physics: Condensed Matter* 12.49 (Dec. 2000), pp. 10105–10121. DOI: `10.1088/0953-8984/12/49/310`.

[136] T. Trupke, R. A. Bardos, M. C. Schubert, and W. Warta. “Photoluminescence imaging of silicon wafers”. In: *Applied Physics Letters* 89.4 (July 2006), p. 044107. DOI: `10.1063/1.2234747`.

[137] F. Gencarelli, B. Vincent, J. Demeulemeester, A. Vantomme, A. Moussa, A. Franquet, A. Kumar, H. Bender, J. Meersschaut, W. Vandervorst, R. Loo, M. Caymax, K. Temst, and M. Heyns. “Crystalline Properties and Strain Relaxation Mechanism of CVD Grown GeSn”. In: *ECS Journal of Solid State Science and Technology* 2.4 (Jan. 2013), P134–P137. DOI: `10.1149/2.011304jss`.

[138] J.-H. Fournier-Lupien, S. Mukherjee, S. Wirths, E. Pippel, N. Hayazawa, G. Mussler, J.-M. Hartmann, P. Desjardins, D. Buca, and O. Moutanabbir. “Strain and composition effects on Raman vibrational modes of silicon-germanium-tin ternary alloys”. In: *Applied Physics Letters* 103 (Dec. 2013), p. 263103. DOI: `10.1063/1.4855436`.

[139] C. Chang, H. Li, T.-P. Chen, W.-K. Tseng, H. Cheng, C.-T. Ko, C.-Y. Hsieh, M.-J. Chen, and G. Sun. “The strain dependence of $\text{Ge}_{1-x}\text{Sn}_x$ (x=0.083) Raman shift”. In: *Thin Solid Films* 593 (Oct. 2015), pp. 40–43. DOI: `10.1016/j.tsf.2015.09.040`.

[140] A. Gassenq, L. Milord, J. Aubin, N. Pauc, K. Guilloy, J. Rothman, D. Rouchon, A. Chelnokov, J. M. Hartmann, V. Reboud, and V. Calvo. “Raman spectral shift versus strain and composition in GeSn layers with 6%-15% Sn content”. In: *Applied Physics Letters* 110.11 (Mar. 2017), p. 112101. DOI: `10.1063/1.4978512`.

[141] J. M. Hinckley and J. Singh. “Influence of substrate composition and crystallographic orientation on the band structure of pseudomorphic Si-Ge alloy films”. In: *Physical Review B* 42.6 (Aug. 1990), pp. 3546–3566. DOI: `10.1103/PhysRevB.42.3546`.

[142] J. Kouvetakis, J. Menendez, and A. V. Chizmeshya. “TIN-BASED GROUP IV SEMICONDUCTORS: New Platforms for Opto- and Microelectronics on Silicon”. In: *Annual Review of Materials Research* 36.1 (Aug. 2006), pp. 497–554. DOI: `10.1146/annurev.matsci.36.090804.095159`.

[143] D. Stange, S. Wirths, N. von den Driesch, G. Mussler, T. Stoica, Z. Ikonić, J. M. Hartmann, S. Mantl, D. Grützmacher, and D. Buca. “Optical tran-

sitions in direct-bandgap $Ge_{1-x}Sn_x$ alloys". In: *ACS Photonics* 2.11 (Nov. 2015), pp. 1539–1545. DOI: `10.1021/acsphotonics.5b00372`.

[144] R. People and J. C. Bean. "Calculation of critical layer thickness versus lattice mismatch for Ge_xSi_{1-x}/Si strained layer heterostructures". In: *Applied Physics Letters* 47.3 (Aug. 1985), pp. 322–324. DOI: `10.1063/1.96206`.

[145] E. A. Fitzgerald, Y.-H. Xie, M. L. Green, D. Brasen, A. R. Kortan, J. Michel, Y.-J. Mii, and B. E. Weir. "Totally relaxed Ge_xSi_{1-x} layers with low threading dislocation densities grown on Si substrates". In: *Applied Physics Letters* 59.7 (Aug. 1991), pp. 811–813. DOI: `10.1063/1.105351`.

[146] Y. Bogumilowicz, J. M. Hartmann, F. Laugier, G. Rolland, T. Billon, N. Cherkashin, and A. Claverie. "High germanium content SiGe virtual substrates grown at high temperatures". In: *Journal of Crystal Growth* 283.3-4 (2005), pp. 346–355. DOI: `10.1016/j.jcrysgro.2005.06.036`.

[147] H. Trinkaus, D. Buca, B. Holländer, R. A. Minamisawa, S. Mantl, and J.-M. Hartmann. "Strain tensors in layer systems by precision ion channeling measurements". In: *Journal of Applied Physics* 107.12 (2010), pp. 1–8. DOI: `10.1063/1.3415530`.

[148] S. Hashimoto, J. L. Peng, W. M. Gibson, L. J. Schowalter, and R. W. Fathauer. "Strain measurement of epitaxial CaF_2 on Si (111) by MeV ion channeling". In: *Applied Physics Letters* 47.10 (Nov. 1985), pp. 1071–1073. DOI: `10.1063/1.96383`.

[149] A. Pidduck, D. Robbins, A. Cullis, W. Leong, and A. Pitt. "Evolution of surface morphology and strain during SiGe epitaxy". In: *Thin Solid Films* 222 (1992), pp. 78–84. DOI: `10.1016/0040-6090(92)90042-A`.

[150] E. A. Fitzgerald, Y.-H. Xie, D. Monroe, P. J. Silverman, J. M. Kuo, A. R. Kortan, F. A. Thiel, and B. E. Weir. "Relaxed Ge_xSi_{1-x} structures for III-V integration with Si and high mobility two-dimensional electron gases in Si". In: *Journal of Vacuum Science & Technology B: Microelectronics and Nanometer Structures & Technology B: Microelectronics and Nanometer Structures* 10.4 (July 1992), p. 1807. DOI: `10.1116/1.586204`.

[151] J. L. Liu, C. D. Moore, G. D. U'Ren, Y. H. Luo, Y. Lu, G. Jin, S. G. Thomas, M. S. Goorsky, and K. L. Wang. "A surfactant-mediated relaxed $Si_{0.5}Ge_{0.5}$ graded layer with a very low threading dislocation density and smooth surface". In: *Applied Physics Letters* 75.11 (1999), p. 1586. DOI: `10.1063/1.124762`.

[152] G. Ehrlich and F. G. Hudda. "Atomic View of Surface Self-Diffusion: Tungsten on Tungsten". In: *The Journal of Chemical Physics* 44.3 (Feb. 1966), pp. 1039–1049. DOI: `10.1063/1.1726787`.

[153] R. L. Schwoebel and E. J. Shipsey. "Step Motion on Crystal Surfaces". In: *Journal of Applied Physics* 37.10 (Sept. 1966), pp. 3682–3686. DOI: `10.1063/1.1707904`.

[154] S. Gupta, E. Simoen, H. Vrielinck, C. Merckling, B. Vincent, F. Gencarelli, R. Loo, and M. Heyns. "Identification of Deep Levels Associated with Extended and Point Defects in GeSn Epitaxial Layers Using DLTS". In: *ECS Transactions* 53.1 (May 2013), pp. 251–258. DOI: `10.1149/05301.0251ecst`.

[155] J. E. Ayers, T. Kujofsa, P. B. Rago, and J. E. Raphael. *Heteroepitaxy of Semiconductors: Theory, Growth, and Characterization*. CRC Press Inc., 2016, p. 643.

[156] F. LeGoues, B. Meyerson, and J. Morar. "Anomalous strain relaxation in SiGe thin films and superlattices." In: *Physical Review Letters* 66.22 (June 1991), pp. 2903–2906. DOI: `10.1103/PhysRevLett.66.2903`.

[157] F. K. LeGoues, B. S. Meyerson, J. F. Morar, and P. D. Kirchner. "Mechanism and conditions for anomalous strain relaxation in graded thin films and superlattices". In: *Journal of Applied Physics* 71.9 (1992), pp. 4230–4243. DOI: `10.1063/1.350803`.

[158] M. S. Abrahams, C. J. Buiocchi, and G. H. Olsen. "Dislocations in vaporgrown compositionally graded (In,Ga)P". In: *Journal of Applied Physics* 46.10 (Oct. 1975), pp. 4259–4270. DOI: `10.1063/1.321409`.

[159] J. P. Hirth and J. Lothe. *Theory of Dislocations*. Krieger Publishing Company, 1982, p. 872.

[160] R. Hull, J. C. Bean, and C. Buescher. “A phenomenological description of strain relaxation in Ge_xSi_{1-x}/Si(100) heterostructures”. In: *Journal of Applied Physics* 66.12 (Dec. 1989), pp. 5837–5843. DOI: `10.1063/1.343604`.

[161] J. Aubin, J. M. Hartmann, A. Gassenq, J. L. Rouviere, E. Robin, V. Delaye, D. Cooper, N. Mollard, V. Reboud, and V. Calvo. “Growth and structural properties of step-graded, high Sn content GeSn layers on Ge”. In: *Semiconductor Science and Technology* 32.9 (Sept. 2017), p. 094006. DOI: `10.1088/1361-6641/aa8084`.

[162] J. D. Fuhr, C. I. Ventura, and R. A. Barrio. “Formation of non-substitutional β-Sn defects in $Ge_{1-x}Sn_x$ alloys”. In: *Journal of Applied Physics* 114.19 (Nov. 2013), p. 193508. DOI: `10.1063/1.4829697`.

[163] C. I. Ventura, J. D. Fuhr, and R. A. Barrio. “Nonsubstitutional single-atom defects in the $Ge_{1-x}Sn_x$ alloy”. In: *Physical Review B* 79.15 (Apr. 2009), p. 155202. DOI: `10.1103/PhysRevB.79.155202`.

[164] A. Chroneos, C. Jiang, U. Schwingenschlögl, and H. Bracht. “Defect interactions in $Sn_{1-x}Ge_x$ random alloys”. In: *Applied Physics Letters* 94 (2009), p. 252104. DOI: `252104\r10.1063/1.3159468`.

[165] S. Decoster, S. Cottenier, U. Wahl, J. G. Correia, and a. Vantomme. “Lattice location study of ion implanted Sn and Sn-related defects in Ge”. In: *Physical Review B* 81.15 (Apr. 2010), p. 155204. DOI: `10.1103/PhysRevB.81.155204`.

[166] V. P. Markevich, A. R. Peaker, B. Hamilton, V. V. Litvinov, Y. M. Pokotilo, S. B. Lastovskii, J. Coutinho, A. Carvalho, M. J. Rayson, and P. R. Briddon. “Tin-vacancy complex in germanium”. In: *Journal of Applied Physics* 109.8 (2011), p. 083705. DOI: `10.1063/1.3574405`.

[167] W. Takeuchi, T. Asano, Y. Inuzuka, M. Sakashita, O. Nakatsuka, and S. Zaima. “Characterization of Shallow- and Deep-Level Defects in Undoped $Ge_{1-x}Sn_x$ Epitaxial Layers by Electrical Measurements”. In: *ECS Journal of Solid State Science and Technology* 5.4 (Dec. 2016), P3082–P3086. DOI: `10.1149/2.0151604jss`.

[168] J. Slotte, S. Kilpeläinen, F. Tuomisto, J. Räisänen, and A. N. Larsen. “Direct observations of the vacancy and its annealing in germanium”. In: *Physical Review B* 83.23 (June 2011), p. 235212. DOI: `10.1103/PhysRevB.83.235212`.

[169] T. Ambridge and M. M. Faktor. “An automatic carrier concentration profile plotter using an electrochemical technique”. In: *Journal of Applied Electrochemistry* 5.4 (Nov. 1975), pp. 319–328. DOI: `10.1007/BF00608796`.

[170] P. Blood. “Capacitance-voltage profiling and the characterisation of III-V semiconductors using electrolyte barriers”. In: *Semiconductor Science and Technology* 1.1 (July 1986), pp. 7–27. DOI: `10.1088/0268-1242/1/1/002`.

[171] C. Schulte-Braucks, K. Narimani, S. Glass, N. von den Driesch, J.-M. Hartmann, Z. Ikonić, V. V. Afanas’ev, Q.-T. Zhao, S. Mantl, and D. Buca. “Correlation of Bandgap Reduction with Inversion Response in (Si)GeSn/High-k/Metal Stacks”. In: *ACS Applied Materials & Interfaces* (Mar. 2017), acsami.6b15279. DOI: `10.1021/acsami.6b15279`.

[172] P. Guo, R. Cheng, W. Wang, Z. Zhang, J. Pan, E. S. Tok, and Y.-C. Yeo. “Silicon Surface Passivation Technology for Germanium-Tin P-Channel MOSFETs: Suppression of Germanium and Tin Segregation for Mobility Enhancement”. In: *ECS Journal of Solid State Science and Technology* 3.8 (July 2014), Q162–Q168. DOI: `10.1149/2.0111408jss`.

[173] G. Han, Y. Wang, Y. Liu, H. Wang, M. Liu, C. Zhang, J. Zhang, B. Cheng, and Y. Hao. “Relaxed germanium-tin P-channel tunneling field-effect transistors fabricated on Si: impacts of Sn composition and uniaxial tensile strain”. In: *AIP Advances* 5.5 (May 2015), p. 057145. DOI: `10.1063/1.4921572`.

[174] C. Schulte-Braucks, N. von den Driesch, S. Glass, A. T. Tiedemann, U. Breuer, A. Besmehn, J.-M. Hartmann, Z. Ikonić, Q.-T. Zhao, S. Mantl, and D. Buca. “Low Temperature Deposition of High-k/Metal Gate Stacks on High-Sn Content (Si)GeSn-Alloys”. In: *ACS Applied Materials & Interfaces* 8.20 (May 2016), pp. 13133–13139. DOI: `10.1021/acsami.6b02425`.

[175] P. Asoka-Kumar, H.-J. Gossmann, F. C. Unterwald, L. C. Feldman, T. C. Leung, H. L. Au, V. Talyanski, B. Nielsen, and K. G. Lynn. “Distribution of point defects in Si(100)/Si grown by low-temperature molecular-beam

epitaxy and solid-phase epitaxy". In: *Physical Review B* 48.8 (Aug. 1993), pp. 5345–5353. DOI: `10.1103/PhysRevB.48.5345`.

[176] S. Gupta, M. Y. Frankel, J. A. Valdmanis, J. F. Whitaker, G. A. Mourou, F. W. Smith, and A. R. Calawa. "Subpicosecond carrier lifetime in GaAs grown by molecular beam epitaxy at low temperatures". In: *Applied Physics Letters* 59.25 (Dec. 1991), pp. 3276–3278. DOI: `10.1063/1.105729`.

[177] X. Liu, A. Prasad, J. Nishio, E. R. Weber, Z. Liliental-Weber, and W. Walukiewicz. "Native point defects in low-temperature-grown GaAs". In: *Applied Physics Letters* 67.2 (July 1995), pp. 279–281. DOI: `10.1063/1.114782`.

[178] C. Schulte-Braucks. "Investigation of GeSn as novel group IV semiconductor for electronic applications". PhD thesis. RWTH Aachen University, 2017.

[179] H. Tran, W. Du, S. A. Ghetmiri, A. Mosleh, G. Sun, R. A. Soref, J. Margetis, J. Tolle, B. Li, H. A. Naseem, and S.-Q. Yu. "Systematic study of $\mathrm{Ge}_{1-x}\mathrm{Sn}_x$ absorption coefficient and refractive index for the device applications of Si-based optoelectronics". In: *Journal of Applied Physics* 119.10 (Mar. 2016), p. 103106. DOI: `10.1063/1.4943652`.

[180] L. Jiang, J. D. Gallagher, C. L. Senaratne, T. Aoki, J. Mathews, J. Kouvetakis, and J. Menéndez. "Compositional dependence of the direct and indirect band gaps in $\mathrm{Ge}_{1-y}\mathrm{Sn}_y$ alloys from room temperature photoluminescence: implications for the indirect to direct gap crossover in intrinsic and n-type materials". In: *Semiconductor Science and Technology* 29.11 (Nov. 2014), p. 115028. DOI: `10.1088/0268-1242/29/11/115028`.

[181] M. Oehme, K. Kostecki, K. Ye, S. Bechler, K. Ulbricht, M. Schmid, M. Kaschel, M. Gollhofer, R. Körner, W. Zhang, E. Kasper, and J. Schulze. "GeSn-on-Si normal incidence photodetectors with bandwidths more than 40 GHz." In: *Optics express* 22.1 (Jan. 2014), pp. 839–46. DOI: `10.1364/OE.22.000839`.

[182] Y.-H. Peng, H. H. Cheng, V. I. Mashanov, and G.-E. Chang. "GeSn p-i-n waveguide photodetectors on silicon substrates". In: *Applied Physics Letters* 105 (2014), p. 231109. DOI: `10.1063/1.4903881`.

[183] H. H. Tseng, H. Li, V. Mashanov, Y. J. Yang, H. H. Cheng, G. E. Chang, R. A. Soref, and G. Sun. “GeSn-based p-i-n photodiodes with strained active layer on a Si wafer”. In: *Applied Physics Letters* 103.23 (Dec. 2013), p. 231907. DOI: `10.1063/1.4840135`.

[184] R. Roucka, J. Mathews, C. Weng, R. Beeler, J. Tolle, J. Menendez, and J. Kouvetakis. “High-Performance Near-IR Photodiodes: A Novel Chemistry-Based Approach to Ge and Ge-Sn Devices Integrated on Silicon”. In: *IEEE Journal of Quantum Electronics* 47.2 (Feb. 2011), pp. 213–222. DOI: `10.1109/JQE.2010.2077273`.

[185] Yuan Dong, Wei Wang, Xin Xu, Xiao Gong, Dian Lei, Qian Zhou, Zhe Xu, Wan Khai Loke, Soon-Fatt Yoon, Gengchiau Liang, and Yee-Chia Yeo. “Germanium-Tin on Si Avalanche Photodiode: Device Design and Technology Demonstration”. In: *IEEE Transactions on Electron Devices* 62.1 (Jan. 2015), pp. 128–135. DOI: `10.1109/TED.2014.2366205`.

[186] R. Soref. “Silicon-based silicon-germanium-tin heterostructure photonics”. In: *Philosophical Transactions of the Royal Society A: Mathematical, Physical and Engineering Sciences* 372.2012 (Feb. 2014), p. 20130113. DOI: `10.1098/rsta.2013.0113`.

[187] Y. Varshni. “Temperature dependence of the energy gap in semiconductors”. In: *Physica* 34.1 (1967), pp. 149–154. DOI: `10.1016/0031-8914(67)90062-6`.

[188] R. Pässler. “Parameter Sets Due to Fittings of the Temperature Dependencies of Fundamental Bandgaps in Semiconductors”. In: *physica status solidi (b)* 216.2 (Dec. 1999), pp. 975–1007. DOI: `10.1002/(SICI)1521-3951(199912)216:2<975::AID-PSSB975>3.0.CO;2-N`.

[189] L. Vina, H. Höchst, and M. Cardona. “Dielectric function of *alpha*-Sn and its temperature dependence”. In: *Physical Review B* 31.2 (Jan. 1985), pp. 958–967. DOI: `10.1103/PhysRevB.31.958`.

[190] S. M. Sze and K. K. Ng. *Physics of Semiconductor Devices*. 3rd ed. Wiley, 2006, p. 832.

[191] S. Wirths, R. Geiger, N. von den Driesch, G. Mussler, T. Stoica, S. Mantl, Z. Ikonić, M. Luysberg, S. Chiussi, J.-M. Hartmann, H. Sigg, J. Faist, D. Buca, and D. Grützmacher. "Lasing in direct-bandgap GeSn alloy grown on Si (Supplementary Informations)". In: *Nature Photonics* (2015), pp. 1–14. DOI: `10.1038/nphoton.2014.321`.

[192] T. Adam, S. Bedell, A. Reznicek, D. Sadana, A. Venkateshan, T. Tsunoda, T. Seino, J. Nakatsuru, and S. Shinde. "Low-temperature growth of epitaxial (100) silicon based on silane and disilane in a 300 mm UHV/CVD cold-wall reactor". In: *Journal of Crystal Growth* 312.23 (Nov. 2010), pp. 3473–3478. DOI: `10.1016/j.jcrysgro.2010.09.012`.

[193] N. von den Driesch, D. Stange, S. Wirths, D. Rainko, I. Povstugar, A. Savenko, U. Breuer, R. Geiger, H. Sigg, Z. Ikonić, J.-M. Hartmann, D. Grützmacher, S. Mantl, and D. Buca. "SiGeSn Ternaries for Efficient Group IV Heterostructure Light Emitters". In: *Small* (Feb. 2017), p. 1603321. DOI: `10.1002/smll.201603321`.

[194] B. Alharthi, A. Mosleh, J. Margetis, S. Al-Kabi, S. A. Ghetmiri, H. Tran, W. Du, M. Benamara, M. Mortazavi, J. Tolle, H. A. Naseem, and S.-Q. Yu. "CVD growth and characterization of $\mathrm{Si}_x\mathrm{Ge}_{1-x-y}\mathrm{Sn}_y$ alloys for high efficiency multi-junction solar cells". In: *2016 IEEE 43rd Photovoltaic Specialists Conference (PVSC)*. IEEE, June 2016, pp. 2817–2821. DOI: `10.1109/PVSC.2016.7750166`.

[195] A. Mosleh, M. Alher, W. Du, L. C. Cousar, S. A. Ghetmiri, S. Al-Kabi, W. Dou, P. C. Grant, G. Sun, R. A. Soref, B. Li, H. A. Naseem, and S.-Q. Yu. "$\mathrm{Si}_y\mathrm{Ge}_{1-x-y}\mathrm{Sn}_x$ films grown on Si using a cold-wall ultrahigh-vacuum chemical vapor deposition system". In: *Journal of Vacuum Science & Technology B, Nanotechnology and Microelectronics: Materials, Processing, Measurement, and Phenomena* 34.1 (Jan. 2016), p. 011201. DOI: `10.1116/1.4936892`.

[196] J. D. Gallagher, C. Xu, L. Jiang, J. Kouvetakis, and J. Menendez. "Fundamental band gap and direct-indirect crossover in $\mathrm{Ge}_{1-x-y}\mathrm{Si}_x\mathrm{Sn}_y$ alloys". In: *Applied Physics Letters* 103.20 (2013), p. 202104. DOI: `10.1063/1.4829621`.

[197] C. Xu, R. T. Beeler, L. Jiang, J. D. Gallagher, R. Favaro, J. Menéndez, and J. Kouvetakis. “Synthesis and optical properties of Sn-rich $\mathrm{Ge}_{1-x-y}\mathrm{Si}_x\mathrm{Sn}_y$ materials and devices”. In: *Thin Solid Films* 557 (Apr. 2014), pp. 177–182. DOI: `10.1016/j.tsf.2013.08.043`.

[198] T. Yamaha, O. Nakatsuka, S. Takeuchi, W. Takeuchi, N. Taoka, K. Araki, K. Izunome, and S. Zaima. “Growth and Characterization of Heteroepitaxial Layers of GeSiSn Ternary Alloy”. In: *ECS Transactions* 50.9 (Mar. 2013), pp. 907–913. DOI: `10.1149/05009.0907ecst`.

[199] D. Stange, N. von den Driesch, D. Rainko, S. Roesgaard, I. Povstugar, J.-M. Hartmann, T. Stoica, Z. Ikonić, S. Mantl, D. Grützmacher, and D. Buca. “Short-wave infrared LEDs from GeSn/SiGeSn multiple quantum wells”. In: *Optica* 4.2 (Feb. 2017), p. 185. DOI: `10.1364/OPTICA.4.000185`.

[200] A. C. Jones and M. L. Hitchman, eds. *Chemical Vapour Deposition*. The Royal Society of Chemistry, 2009. DOI: `10.1039/9781847558794`.

[201] Y. Xu and X.-T. Yan. *Chemical Vapour Deposition - An Integrated Engineering Design for Advanced Materials*. Engineering Materials and Processes. London: Springer London, 2010, p. 342. DOI: `10.1007/978-1-84882-894-0`.

[202] J. Xie, A. V. G. Chizmeshya, J. Tolle, V. R. D’Costa, J. Menendez, and J. Kouvetakis. “Synthesis, Stability Range, and Fundamental Properties of Si-Ge-Sn Semiconductors Grown Directly on Si(100) and Ge(100) Platforms”. In: *Chemistry of Materials* 22.12 (June 2010), pp. 3779–3789. DOI: `10.1021/cm100915q`.

[203] Y.-C. Yeo and J. Sun. “Finite-element study of strain distribution in transistor with silicon-germanium source and drain regions”. In: *Applied Physics Letters* 86.2 (Jan. 2005), p. 023103. DOI: `10.1063/1.1846152`.

[204] S. Wirths, R. Troitsch, G. Mussler, J.-M. Hartmann, P. Zaumseil, T. Schroeder, S. Mantl, and D. Buca. “Ternary and quaternary Ni(Si)Ge(Sn) contact formation for highly strained Ge p- and n-MOSFETs”. In: *Semiconductor Science and Technology* 30.5 (2015), p. 055003. DOI: `10.1088/0268-1242/30/5/055003`.

[205] B. Vincent, Y. Shimura, S. Takeuchi, T. Nishimura, G. Eneman, A. Firrincieli, J. Demeulemeester, A. Vantomme, T. Clarysse, O. Nakatsuka, S. Zaima, J. Dekoster, M. Caymax, and R. Loo. "Characterization of GeSn materials for future Ge pMOSFETs source/drain stressors". In: *Microelectronic Engineering* 88.4 (Apr. 2011), pp. 342–346. DOI: `10.1016/j.mee.2010.10.025`.

[206] J. Weber and M. I. Alonso. "Near-band-gap photoluminescence of Si-Ge alloys". In: *Physical Review B* 40.8 (1989), pp. 5683–5693. DOI: `10.1103/PhysRevB.40.5683`.

[207] V. R. D'Costa, C. S. Cook, A. G. Birdwell, C. L. Littler, M. Canonico, S. Zollner, J. Kouvetakis, and J. Menéndez. "Optical critical points of thin-film $\mathrm{Ge}_{1-y}\mathrm{Sn}_y$ alloys: A comparative $\mathrm{Ge}_{1-y}\mathrm{Sn}_y/\mathrm{Ge}_{1-x}\mathrm{Si}_x$ study". In: *Physical Review B* 73.12 (Mar. 2006), p. 125207. DOI: `10.1103/PhysRevB.73.125207`.

[208] H. Lin, R. Chen, W. Lu, Y. Huo, T. I. Kamins, and J. S. Harris. "Investigation of the direct band gaps in $\mathrm{Ge}_{1-x}\mathrm{Sn}_x$ alloys with strain control by photoreflectance spectroscopy". In: *Applied Physics Letters* 100.10 (Mar. 2012), p. 102109. DOI: `10.1063/1.3692735`.

[209] A. Gassenq, L. Milord, J. Aubin, K. Guilloy, S. Tardif, N. Pauc, J. Rothman, A. Chelnokov, J. M. Hartmann, V. Reboud, and V. Calvo. "Gamma bandgap determination in pseudomorphic GeSn layers grown on Ge with up to 15% Sn content". In: *Applied Physics Letters* 109.24 (Dec. 2016), p. 242107. DOI: `10.1063/1.4971397`.

[210] J. E. Bernard and A. Zunger. "Electronic structure of ZnS, ZnSe, ZnTe, and their pseudobinary alloys". In: *Physical Review B* 36.6 (Aug. 1987), pp. 3199–3228. DOI: `10.1103/PhysRevB.36.3199`.

[211] T. Nagai, T. Kaneko, Z. Liu, I. Turkevych, and M. Kondo. "Improvement of photoconductivity in Silicon Tin (SiSn) thin films". In: *Journal of Non-Crystalline Solids* 358.17 (Sept. 2012), pp. 2281–2284. DOI: `10.1016/j.jnoncrysol.2011.12.096`.

[212] M. Kurosawa, M. Kato, T. Yamaha, N. Taoka, O. Nakatsuka, and S. Zaima. "Near-infrared light absorption by polycrystalline SiSn alloys grown on in-

sulating layers". In: *Applied Physics Letters* 106.17 (Apr. 2015), p. 171908. DOI: `10.1063/1.4919451`.

[213] A. Tonkikh, N. Zakharov, C. Eisenschmidt, H. Leipner, and P. Werner. "Aperiodic SiSn/Si multilayers for thermoelectric applications". In: *Journal of Crystal Growth* 392 (Apr. 2014), pp. 49–51. DOI: `10.1016/j.jcrysgro.2014.01.047`.

[214] A. M. Hussain, N. Singh, H. Fahad, K. Rader, U. Schwingenschlögl, and M. Hussain. "Exploring SiSn as a performance enhancing semiconductor: A theoretical and experimental approach". In: *Journal of Applied Physics* 116 (2014), p. 224506. DOI: `10.1063/1.4904056`.

[215] T. Wendav, I. Fischer, M. Montanari, M. H. Zoellner, W. M. Klesse, G. Capellini, N. von den Driesch, M. Oehme, D. Buca, K. Busch, and J. Schulze. "Compositional dependence of the band-gap of $Ge_{1-x-y}Si_xSn_y$ alloys". In: *Applied Physics Letters* 108.24 (June 2016), p. 242104. DOI: `10.1063/1.4953784`.

[216] V. R. D'Costa, Y. Y. Fang, J. Tolle, J. Kouvetakis, and J. Menéndez. "Tunable optical gap at a fixed lattice constant in group-IV semiconductor alloys". In: *Physical Review Letters* 102.10 (2009), pp. 1–4. DOI: `10.1103/PhysRevLett.102.107403`.

[217] H. Lin, R. Chen, W. Lu, Y. Huo, T. I. Kamins, and J. S. Harris. "Structural and optical characterization of $Si_xGe_{1-x-y}Sn_y$ alloys grown by molecular beam epitaxy". In: *Applied Physics Letters* 100.14 (Apr. 2012), p. 141908. DOI: `10.1063/1.3701732`.

[218] P. G. Moses and C. G. Van de Walle. "Band bowing and band alignment in InGaN alloys". In: *Applied Physics Letters* 96.2 (2010), p. 021908. DOI: `10.1063/1.3291055`. arXiv: `/dx.doi.org/10.1063/1.3291055 [http:]`.

[219] A. Belabbes, M. Ferhat, and A. Zaoui. "Giant and composition-dependent optical band gap bowing in dilute $GaSb_{1-x}N_x$ alloys". In: *Applied Physics Letters* 88 (Apr. 2006), p. 152109. DOI: `10.1063/1.2196049`.

[220] S. Mukherjee, N. Kodali, D. Isheim, S. Wirths, J.-M. Hartmann, D. Buca, D. N. Seidman, and O. Moutanabbir. "Short-range atomic ordering in non-equilibrium silicon-germanium-tin semiconductors". In: *Physical Review B* 95.16 (Apr. 2017), p. 161402. DOI: `10.1103/PhysRevB.95.161402`.

[221] L. Jiang, C. Xu, J. D. Gallagher, R. Favaro, T. Aoki, J. Menéndez, and J. Kouvetakis. "Development of Light Emitting Group IV Ternary Alloys on Si Platforms for Long Wavelength Optoelectronic Applications". In: *Chemistry of Materials* 26.8 (Apr. 2014), pp. 2522–2531. DOI: `10.1021/cm403801b`.

[222] K. P. Homewood and M. A. Lourenço. "The rise of the GeSn laser". In: *Nature Photonics* 9.2 (Feb. 2015), pp. 78–79. DOI: `10.1038/nphoton.2015.1`.

[223] M. Oehme, J. Werner, M. Gollhofer, M. Schmid, M. Kaschel, E. Kasper, and J. Schulze. "Room-Temperature Electroluminescence From GeSn Light-Emitting Pin Diodes on Si". In: *IEEE Photonics Technology Letters* 23.23 (Dec. 2011), pp. 1751–1753. DOI: `10.1109/LPT.2011.2169052`.

[224] J. D. Gallagher, C. L. Senaratne, P. M. Wallace, J. Menéndez, and J. Kouvetakis. "Electroluminescence from $Ge_{1-y}Sn_y$ diodes with degenerate pn junctions". In: *Applied Physics Letters* 107.12 (Sept. 2015), p. 123507. DOI: `10.1063/1.4931707`.

[225] D. Stange, N. von den Driesch, D. Rainko, C. Schulte-Braucks, S. Wirths, G. Mussler, A. T. Tiedemann, T. Stoica, J.-M. Hartmann, Z. Ikonić, S. Mantl, D. Grützmacher, and D. Buca. "Study of GeSn based heterostructures: towards optimized group IV MQW LEDs". In: *Optics Express* 24.2 (Jan. 2016), p. 1358. DOI: `10.1364/OE.24.001358`.

[226] Y. Zhou, W. Dou, W. Du, T. Pham, S. A. Ghetmiri, S. Al-Kabi, A. Mosleh, M. Alher, J. Margetis, J. Tolle, G. Sun, R. Soref, B. Li, M. Mortazavi, H. Naseem, and S.-Q. Yu. "Systematic study of GeSn heterostructure-based light-emitting diodes towards mid-infrared applications". In: *Journal of Applied Physics* 120.2 (July 2016), p. 023102. DOI: `10.1063/1.4958337`.

[227] J. D. Gallagher, C. L. Senaratne, P. Sims, T. Aoki, J. Menéndez, and J. Kouvetakis. "Electroluminescence from GeSn heterostructure pin diodes at

the indirect to direct transition". In: *Applied Physics Letters* 106.9 (Mar. 2015), p. 091103. DOI: `10.1063/1.4913688`.

[228] H. H. Tseng, K. Y. Wu, H. Li, V. Mashanov, H. H. Cheng, G. Sun, and R. a. Soref. "Mid-infrared electroluminescence from a Ge/$Ge_{0.922}Sn_{0.078}$/Ge double heterostructure p-i-n diode on a Si substrate". In: *Applied Physics Letters* 102.18 (May 2013), p. 182106. DOI: `10.1063/1.4804675`.

[229] B. Schwartz, M. Oehme, K. Kostecki, D. Widmann, M. Gollhofer, R. Koerner, S. Bechler, I. A. Fischer, T. Wendav, E. Kasper, J. Schulze, and M. Kittler. "Electroluminescence of GeSn/Ge MQW LEDs on Si substrate". In: *Optics Letters* 40.13 (July 2015), p. 3209. DOI: `10.1364/OL.40.003209`.

[230] N. von den Driesch, D. Stange, S. Wirths, D. Rainko, G. Mussler, T. Stoica, Z. Ikonić, J.-M. Hartmann, D. Grützmacher, S. Mantl, and D. Buca. "Direct bandgap GeSn light-emitting diodes for short-wave infrared applications grown on Si". In: *SPIE Photonics West*. Ed. by G. T. Reed and A. P. Knights. Vol. 9752. Mar. 2016, p. 97520C. DOI: `10.1117/12.2211641`.

[231] E. F. Schubert. *Light-Emitting Diodes*. 2nd. Cambridge University Press, 2006, p. 434.

[232] W. Shockley and W. T. Read. "Statistics of the Recombination of Holes and Electrons". In: *Physical Review* 87.46 (1952), pp. 835–842. DOI: `dx.doi.org/10.1103/PhysRev.87.835`.

[233] Z. Alferov. "Double heterostructure lasers: Early days and future perspectives". In: *IEEE Journal on Selected Topics in Quantum Electronics* 6.6 (Nov. 2000), pp. 832–840. DOI: `10.1109/2944.902131`.

[234] A. R. Adams. "Strained-Layer Quantum-Well Lasers". In: *IEEE Journal of Selected Topics in Quantum Electronics* 17.5 (Sept. 2011), pp. 1364–1373. DOI: `10.1109/JSTQE.2011.2108995`.

[235] V. S. S. Srinivasan, I. A. Fischer, L. Augel, A. Hornung, R. Koerner, K. Kostecki, M. Oehme, E. Rolseth, and J. Schulze. "Contact resistivities of antimony-doped n-type $Ge_{1-x}Sn_x$". In: *Semiconductor Science and Technology* 31.8 (Aug. 2016), 08LT01. DOI: `10.1088/0268-1242/31/8/08LT01`.

[236] C. L. Senaratne, J. D. Gallagher, T. Aoki, J. Kouvetakis, and J. Menéndez. “Advances in light emission from group-IV alloys via lattice engineering and n-type doping based on custom-designed chemistries”. In: *Chemistry of Materials* 26.20 (Oct. 2014), pp. 6033–6041. DOI: `10.1021/cm502988y`.

[237] A. Mosleh, S. A. Ghetmiri, B. R. Conley, M. Hawkridge, M. Benamara, A. Nazzal, J. Tolle, S.-Q. Yu, and H. A. Naseem. “Material Characterization of Ge1-x Snx Alloys Grown by a Commercial CVD System for Optoelectronic Device Applications”. In: *Journal of Electronic Materials* 43.4 (Mar. 2014), pp. 938–946. DOI: `10.1007/s11664-014-3089-2`.

[238] C. Schulte-Braucks, D. Stange, N. von den Driesch, S. Blaeser, Z. Ikonić, J. M. Hartmann, S. Mantl, and D. Buca. “Negative differential resistance in direct bandgap GeSn p-i-n structures”. In: *Applied Physics Letters* 107.4 (July 2015), p. 042101. DOI: `10.1063/1.4927622`.

[239] J. Margetis, A. Mosleh, S. A. Ghetmiri, S. Al-Kabi, W. Dou, W. Du, N. Bhargava, S.-Q. Yu, H. Profijt, D. Kohen, R. Loo, A. Vohra, and J. Tolle. “Fundamentals of $\mathrm{Ge}_{1-x}\mathrm{Sn}_x$ and $\mathrm{Si}_y\mathrm{Ge}_{1-x-y}\mathrm{Sn}_x$ RPCVD epitaxy”. In: *Materials Science in Semiconductor Processing* 70 (Nov. 2017), pp. 38–43. DOI: `10.1016/j.mssp.2016.12.024`.

[240] W. Albrecht, J. Moers, and B. Hermanns. “HNF - Helmholtz Nano Facility”. In: *Journal of large-scale research facilities JLSRF* 3 (May 2017), A112. DOI: `10.17815/jlsrf-3-158`.

[241] C. Schulte-Braucks, E. Hofmann, S. Glass, N. von den Driesch, G. Mussler, U. Breuer, J.-M. Hartmann, P. Zaumseil, T. Schroeder, Q.-T. Zhao, S. Mantl, and D. Buca. “Schottky barrier tuning via dopant segregation in NiGeSn-GeSn contacts”. In: *Journal of Applied Physics* 121.20 (May 2017), p. 205705. DOI: `10.1063/1.4984117`.

[242] D. Stange, N. von den Driesch, D. Rainko, T. Zabel, B. Marzban, Z. Ikonić, P. Zaumseil, G. Capellini, S. Mantl, J. Witzens, H. Sigg, D. Grützmacher, and D. Buca. “Quantum Confinement Effects in GeSn/SiGeSn Heterostructure Lasers (Invited)”. In: *IEEE International Electron Device Meeting (IEDM) 2017*. 2017.

[243] F. Gencarelli, D. Grandjean, Y. Shimura, B. Vincent, D. Banerjee, A. Vantomme, W. Vandervorst, R. Loo, M. Heyns, and K. Temst. "Extended X-ray absorption fine structure investigation of Sn local environment in strained and relaxed epitaxial $Ge_{1-x}Sn_x$ films". In: *Journal of Applied Physics* 117.9 (2015), p. 095702. DOI: `10.1063/1.4913856`.

[244] A. Kumar, M. P. Komalan, H. Lenka, A. K. Kambham, M. Gilbert, F. Gencarelli, B. Vincent, and W. Vandervorst. "Atomic insight into $Ge_{1-x}Sn_x$ using atom probe tomography". In: *Ultramicroscopy* 132 (2013), pp. 171–178. DOI: `10.1016/j.ultramic.2013.02.009`.

[245] Y. Shimura, T. Asano, T. Yamaha, M. Fukuda, W. Takeuchi, O. Nakatsuka, and S. Zaima. "EXAFS study of local structure contributing to Sn stability in $Si_yGe_{1-y-z}Sn_z$". In: *Materials Science in Semiconductor Processing* (Nov. 2016). DOI: `10.1016/j.mssp.2016.11.013`.

[246] A. Sanson. "Local dynamical properties of crystalline germanium and their effects in extended x-ray absorption fine structure". In: *Physical Review B* 81.1 (Jan. 2010), p. 012304. DOI: `10.1103/PhysRevB.81.012304`.

[247] M. J. Hÿtch, F. Houdellier, F. Hüe, and E. Snoeck. "Dark-field electron holography for the measurement of geometric phase". In: *Ultramicroscopy* 111.8 (2011), pp. 1328–1337. DOI: `10.1016/j.ultramic.2011.04.008`.

[248] A. Béché, J. L. Rouvière, J. P. Barnes, and D. Cooper. "Dark field electron holography for strain measurement". In: *Ultramicroscopy* 111.3 (2011), pp. 227–238. DOI: `10.1016/j.ultramic.2010.11.030`.

[249] M. Adams. "Design eines optisch gepumpten, wellenleiter-gekoppelten Germanium-Zinn Lasers und Aufbau eines optischen Messplatzes für 2,5 μm Wellenlänge". PhD thesis. RWTH Aachen University, 2016, p. 66.

[250] K. Thompson, D. Lawrence, D. J. Larson, J. D. Olson, T. F. Kelly, and B. Gorman. "In situ site-specific specimen preparation for atom probe tomography". In: *Ultramicroscopy* 107.2-3 (Feb. 2007), pp. 131–139. DOI: `10.1016/j.ultramic.2006.06.008`.

Acknowledgements

Walking the long and winding road over the course of the past years was a demanding, yet highly rewarding experience. The possibility to learn something new, to find something exciting after every turn, made every day a unique experience. I am grateful to all the people, who accompanied me during that time, who offered help, support and wisdom.

First of all, I'd like to thank my doctoral supervisor Prof. Siegfried Mantl, who enabled me to work in his group in such a scientifically interesting field and always gave me the freedom to pursue my goals. Further, I also want to thank Prof. Christoph Stampfer, who immediately agreed to act as second supervisor for this thesis.

I feel huge gratitude to Dr. Dan Buca, who, as my daily supervisor, always pushed me beyond the state-of-the-art. Daily discussions, help in writing the first papers and introduction to his scientific networks; all these were invaluable lessons along the way. Further, I also want to thank Prof. Detlev Grützmacher, not only for having the opportunity to work in his institute in a fascinating field, but also his constant interest, which lead to numerous scientific discussions.

A big thanks to our present and previous GeSn-Team members, first of all Daniela Stange, with whom I not only shared an office for several years, but also probably more discussions during coffee than can be considered healthy. Her support was not only limited to all kind of optical sample characterizations, but fortunately also in non-work related biking and boxing events. Further thanks also to my predecessor Dr. Stephan Wirths, who introduced me to all important experiments and was always open to discussions, to Denis Rainko, who could always help with epitaxy and calculations. Thanks also to our electronics guys, Christian Schulte-Braucks, who laid the foundation for all GeSn clean room processing, and Konstantin Mertens, with whom also the art of espresso finally found its entry into our institute.

Of course I want to mention our 'Waldschlösschen'-Team, Andreas Tiedemann, Karl-

Heinz Deussen and Patric Bernardy, who kept our epitaxy tools and all the surrounding infrastructure running. I am grateful for the big group of people keeping the RBS equipment running, namely Dr. Jürgen Schubert, Dr. Bernd Holländer, Christian Scholtysik, André Dahmen and Katja Palmen. Thankfully, a lot of people inside the Forschungszentrum were also supporting my research by employing different characterization techniques and helping in data analysis. Especially I want to thank Dr. Gregor Mussler for XRD techniques, Steffi Lenk and Lidia Kipkalo for TEM sample preparation & analysis and Uwe Breuer for countless SIMS data acquisitions. Further I want to thank Ivan Povstugar, who did impressive Atom Probe Tomography measurements, including specimen preparation and data renormalization. I also want to mention Toma Stoica, who helped with several optical characterization techniques and was kind enough to share his impressive insights on optical measurements.

We are lucky for also having a large group of external collaborators, who supported us with all kinds of experiments and methods. Especially I want to mention Dr. Jean-Michel Hartmann from *CEA-Leti*, who always provided us with high quality Ge substrates and further offered lots of help during paper preparation. I'm also thankful to Dr. Zoran Ikonić from the *University of Leeds*, who supplied the codes for band structure calculations and helped with all questions regarding theory. Furthermore, I want to mention our collaborators from *IHP*, namely Prof. Thomas Schroeder, Prof. Giovanni Capellini and Dr. Peter Zaumseil, who performed X-Ray diffraction techniques, STEM and EDX measurements. Further thanks to Prof. Jeremy Witzens, Bahareh Marzban and Martin Adams from the *RWTH Aachen*, who performed simulations, designed integrated photonic circuits and were always available for scientific discussions. I also want to thank Dr. Thibaud Denneulin from *CEMES-CNRS*, who carried out electron holography experiments of our samples.

Particular thanks to Christian Schulte-Braucks, Stefan Glass and Vinh Luong, whom I could always bother regarding clean room processing and who were never short of smart solutions. In this regard, I additionally thank the HNF staff for their assistance.

I would like to express my thanks to all remaining institute members I haven't mentioned by name, but who had a stake in the pleasant working atmosphere in this institute, including all current and former PhD candidates, students, the scientific

and non-scientific staff.
In the end, I owe my friends, family and particulary my parents a debt of gratitude. Without their support and believe in me, I wouldn't have become the person I am today.

List of Publications

Primary Author

- N. von den Driesch, D. Stange, S. Wirths, D. Rainko, I. Povstugar, A. Savenko, U. Breuer, R. Geiger, H. Sigg, Z. Ikonić, J.-M. Hartmann, D. Grützmacher, S. Mantl, and D. Buca. "SiGeSn Ternaries for Efficient Group IV Heterostructure Light Emitters". In: *Small* (Feb. 2017), p. 1603321. DOI: `10.1002/smll.201603321`.
- N. von den Driesch, D. Stange, S. Wirths, D. Rainko, G. Mussler, T. Stoica, Z. Ikonić, J.-M. Hartmann, D. Grützmacher, S. Mantl, and D. Buca. "Direct bandgap GeSn light-emitting diodes for short-wave infrared applications grown on Si". In: *SPIE Photonics West*. Ed. by G. T. Reed and A. P. Knights. Vol. 9752. Mar. 2016, p. 97520C. DOI: `10.1117/12.2211641`.
- N. von den Driesch, D. Stange, S. Wirths, G. Mussler, B. Holländer, Z. Ikonić, J. M. Hartmann, T. Stoica, S. Mantl, D. Grützmacher, and D. Buca. "Direct bandgap group IV epitaxy on Si for laser applications". In: *Chemistry of Materials* 27.13 (June 2015), pp. 4693–4702. DOI: `10.1021/acs.chemmater.5b01327`.

Contributing Author

- S. Glass, N. von den Driesch, S. Strangio, C. Schulte-Braucks, T. Rieger, K. Narimani, D. Buca, S. Mantl, and Q.-T. Zhao. "Experimental examination of tunneling paths in SiGe/Si gate-normal tunneling field-effect transistors". In: *Applied Physics Letters* 111.26 (Dec. 2017), p. 263504. DOI: `10.1063/1.4996109`.

- I. A. Fischer, A. Berrier, F. Hornung, M. Oehme, P. Zaumseil, G. Capellini, N. von den Driesch, D. Buca, and J. Schulze. “Optical critical points of $Si_xGe_{1-x-y}Sn_y$ alloys with high Si content”. In: *Semiconductor Science and Technology* 32.12 (Nov. 2017), p. 124004.

- F. Lüpke, M. Eschbach, T. Heider, M. Lanius, P. Schüffelgen, D. Rosenbach, N. von den Driesch, V. Cherepanov, G. Mussler, L. Plucinski, D. Grützmacher, C. M. Schneider, and B. Voigtländer. “Electrical resistance of individual defects at a topological insulator surface”. In: *Nature Communications* 8 (June 2017), p. 15704. DOI: `10.1038/ncomms15704`.

- C. Schulte-Braucks, K. Narimani, S. Glass, N. von den Driesch, J.-M. Hartmann, Z. Ikonić, V. V. Afanas’ev, Q.-T. Zhao, S. Mantl, and D. Buca. “Correlation of Bandgap Reduction with Inversion Response in (Si)GeSn/High-k/Metal Stacks”. In: *ACS Applied Materials & Interfaces* (Mar. 2017), acsami.6b15279. DOI: `10.1021/acsami.6b15279`.

- S. Assali, A. Dijkstra, A. Li, S. Koelling, M. A. Verheijen, L. Gagliano, N. von den Driesch, D. Buca, P. M. Koenraad, J. E. M. Haverkort, and E. P. A. M. Bakkers. “Growth and Optical Properties of Direct Band Gap Ge/$Ge_{0.87}Sn_{0.13}$ Core/Shell Nanowire Arrays”. In: *Nano Letters* 17.3 (Feb. 2017), pp. 1538–1544. DOI: `10.1021/acs.nanolett.6b04627`.

- C. Schulte-Braucks, S. Glass, E. Hofmann, D. Stange, N. von den Driesch, J.-M. Hartmann, Z. Ikonić, Q.-T. Zhao, D. Buca, and S. Mantl. “Process modules for GeSn nanoelectronics with high Sn-contents”. In: *Solid-State Electronics* 128 (Feb. 2017), pp. 54–59. DOI: `10.1016/j.sse.2016.10.024`.

- D. Stange, N. von den Driesch, D. Rainko, S. Roesgaard, I. Povstugar, J.-M. Hartmann, T. Stoica, Z. Ikonić, S. Mantl, D. Grützmacher, and D. Buca. “Short-wave infrared LEDs from GeSn/SiGeSn multiple quantum wells”. In: *Optica* 4.2 (Feb. 2017), p. 185. DOI: `10.1364/OPTICA.4.000185`.

- S. Blaeser, S. Glass, C. Schulte-Braucks, K. Narimani, N. von den Driesch, S. Wirths, A. T. Tiedemann, S. Trellenkamp, D. Buca, S. Mantl, and Q.-T. Zhao. “Line Tunneling Dominating Charge Transport in SiGe/Si Heterostructure TFETs”. In: *IEEE Transactions on Electron Devices* 63.11 (Nov. 2016), pp. 4173–4178. DOI: `10.1109/TED.2016.2608383`.

- O. Madia, V. V. Afanas’ev, D. Cott, H. Arimura, C. Schulte-Braucks, H. C. Lin, D. Buca, N. von den Driesch, L. Nyns, T. Ivanov, D. Cuypers, and A. Stesmans. “Saturation Photo-Voltage Methodology for Semiconductor/Insulator Interface Trap Spectroscopy”. In: *ECS Journal of Solid State Science and Technology* 5.4 (Nov. 2016), P3031–P3036. DOI: `10.1149/2.0061604jss`.

- G. J. Verbiest, D. Xu, M. Goldsche, T. Khodkov, S. Barzanjeh, N. von den Driesch, D. Buca, and C. Stampfer. “Tunable mechanical coupling between driven microelectromechanical resonators”. In: *Applied Physics Letters* 109.14 (Oct. 2016), p. 143507. DOI: `10.1063/1.4964122`.

- D. Stange, S. Wirths, R. Geiger, C. Schulte-Braucks, B. Marzban, N. von den Driesch, G. Mussler, T. Zabel, T. Stoica, J.-M. Hartmann, S. Mantl, Z. Ikonić, D. Grützmacher, H. Sigg, J. Witzens, and D. Buca. “Optically Pumped GeSn Microdisk Lasers on Si”. In: *ACS Photonics* 3.7 (July 2016), pp. 1279–1285. DOI: `10.1021/acsphotonics.6b00258`.

- T. Wendav, I. Fischer, M. Montanari, M. H. Zoellner, W. M. Klesse, G. Capellini, N. von den Driesch, M. Oehme, D. Buca, K. Busch, and J. Schulze. “Compositional dependence of the band-gap of $\mathrm{Ge}_{1-x-y}\mathrm{Si}_x\mathrm{Sn}_y$ alloys”. In: *Applied Physics Letters* 108.24 (June 2016), p. 242104. DOI: `10.1063/1.4953784`.

- C. Schulte-Braucks, N. von den Driesch, S. Glass, A. T. Tiedemann, U. Breuer, A. Besmehn, J.-M. Hartmann, Z. Ikonić, Q.-T. Zhao, S. Mantl, and D. Buca. “Low Temperature Deposition of High-k/Metal Gate Stacks on High-Sn Content (Si)GeSn-Alloys”. In: *ACS Applied Materials & Interfaces* 8.20 (May 2016), pp. 13133–13139. DOI: `10.1021/acsami.6b02425`.

- N. Taoka, G. Capellini, N. von den Driesch, D. Buca, P. Zaumseil, M. A. Schubert, W. M. Klesse, M. Montanari, and T. Schroeder. “Sn migration control at high temperature due to high deposition speed for forming high-quality GeSn layer”. In: *Applied Physics Express* 9.3 (Mar. 2016), p. 031201. doi: 10.7567/APEX.9.031201.
- D. Stange, N. von den Driesch, D. Rainko, C. Schulte-Braucks, S. Wirths, G. Mussler, A. T. Tiedemann, T. Stoica, J.-M. Hartmann, Z. Ikonić, S. Mantl, D. Grützmacher, and D. Buca. “Study of GeSn based heterostructures: towards optimized group IV MQW LEDs”. In: *Optics Express* 24.2 (Jan. 2016), p. 1358. doi: 10.1364/OE.24.001358.
- S. S. Azadeh, F. Merget, S. Romero-Garcia, A. Moscoso-Martir, N. von den Driesch, J. Müller, S. Mantl, D. Buca, and J. Witzens. “Low V_π Silicon photonics modulators with highly linear epitaxially grown phase shifters”. In: *Optics Express* 23.18 (Aug. 2015), pp. 23526–23550. doi: 10.1364/OE.23.023526.
- C. Schulte-Braucks, D. Stange, N. von den Driesch, S. Blaeser, Z. Ikonić, J. M. Hartmann, S. Mantl, and D. Buca. “Negative differential resistance in direct bandgap GeSn p-i-n structures”. In: *Applied Physics Letters* 107.4 (July 2015), p. 042101. doi: 10.1063/1.4927622.
- S. Wirths, R. Geiger, N. von den Driesch, G. Mussler, T. Stoica, S. Mantl, Z. Ikonić, M. Luysberg, S. Chiussi, J.-M. Hartmann, H. Sigg, J. Faist, D. Buca, and D. Grützmacher. “Lasing in direct-bandgap GeSn alloy grown on Si”. In: *Nature Photonics* 9.2 (Jan. 2015), pp. 88–92. doi: 10.1038/nphoton.2014.321.
- S. Wirths, Z. Ikonić, N. von den Driesch, G. Mussler, U. Breuer, A. Tiedemann, P. Bernardy, B. Holländer, T. Stoica, J.-M. Hartmann, D. Grutzmacher, S. Mantl, and D. Buca. “Growth Studies of Doped SiGeSn/Strained Ge(Sn) Heterostructures”. In: *ECS Transactions* 64.6 (Aug. 2014), pp. 689–696. doi: 10.1149/06406.0689ecst.

Conference Contributions

- N. von den Driesch, D. Stange, D. Rainko, P. Zaumseil, G. Capellini, J.-M. Hartmann, T. Schroeder, S. Mantl, D. Grützmacher, and D. Buca. “Epitaxy of direct bandgap group IV heterostructure lasers”. In: *IEEE 14th International Conference on Group IV Photonics (GFP)*. Berlin (Germany), Aug. 2017.
- N. von den Driesch, D. Stange, D. Rainko, S. Wirths, G. Mussler, I. Povstugar, Z. Ikonić, J.-M. Hartmann, D. Grützmacher, S. Mantl, and D. Buca. “Epitaxy of group IV SiGeSn alloys towards efficient light emitters”. In: *JSPS Workshop on "Atomically Controlled Processing for Ultra-large Scale Integration"*. Jülich (Germany), Nov. 2016.
- N. von den Driesch, D. Stange, D. Rainko, S. Wirths, G. Mussler, Z. Ikonić, J.-M. Hartmann, D. Grützmacher, S. Mantl, and D. Buca. “Epitaxy of SiGeSn ternaries for group IV light emitting diodes”. In: *European Material Research Society (E-MRS) Spring Meeting 2016*. Lille (France), May 2016, K.14.2.
- N. von den Driesch, D. Stange, S. Wirths, D. Rainko, G. Mussler, Z. Ikonić, J.-M. Hartmann, D. Grützmacher, S. Mantl, and D. Buca. “Tailoring group IV (Si)GeSn alloys for photonic applications (Invited)”. In: *imec Academy*. Leuven (Belgium), Mar. 2016.
- N. von den Driesch, S. Wirths, D. Stange, T. Stoica, A. T. Tiedemann, Z. Ikonić, J.-M. Hartmann, G. Mussler, D. Grützmacher, S. Mantl, and D. Buca. “Thick GeSn alloys for mid IR lasing applications”. In: *9th International Conference on Silicon Epitaxy and Heterostructures (ICSI)*. Montréal (Canada), May 2015.
- N. von den Driesch, S. Wirths, D. Stange, A. T. Tiedemann, G. Mussler, T. Stoica, S. Lenk, U. Breuer, D. Grützmacher, S. Mantl, and D. Buca. “Growth studies of strain relaxed and high Sn content GeSn layers for optoelectronic applications”. In: *European Material Research Society (E-MRS) Fall Meeting 2014*. Warsaw (Poland), Sept. 2014, J.15.3.

Band / Volume 150
Spectroscopic characterization of local valence change processes in resistively switching complex oxides
C. Bäumer (2017), x, 206 pp
ISBN: 978-3-95806-246-7

Band / Volume 151
Magnetic structure in relation to the magnetic field induced ferroelectricity in Y-type hexaferrite $Ba_{2-x}Sr_xZn_2Fe_{12}O_{22}$
P. Thakuria (2017), 17, 180 pp
ISBN: 978-3-95806-250-4

Band / Volume 152
Statistical analysis tools for assessing the functional relevance of higher-order correlations in massively parallel spike trains
V. Rostami (2017), x, 176 pp
ISBN: 978-3-95806-251-1

Band / Volume 153
The influence of the substrate on the structure and electronic properties of carbon-based 2D materials
J. Sforzini (2017), XIII, 145 pp
ISBN: 978-3-95806-255-9

Band / Volume 154
Gate-All-Around Silicon Nanowire Tunnel FETs for Low Power Applications
G. V. Luong (2017), ii, 136 pp
ISBN: 978-3-95806-259-7

Band / Volume 155
Graphene Devices for Extracellular Measurements
D. Kireev (2017), ix, 169 pp
ISBN: 978-3-95806-265-8

Band / Volume 156
Nanoscale 3D structures towards improved cell-chip coupling on microelectrode arrays
S. D. Weidlich (2017), II, 154 pp
ISBN: 978-3-95806-278-8

Band / Volume 157
Interface phenomena in $La_{1/3}Sr_{2/3}FeO_3$ / $La_{2/3}Sr_{1/3}MnO_3$ heterostructures and a quest for p-electron magnetism
M. Waschk (2017), ix, 205 pp
ISBN: 978-3-95806-281-8

Schriften des Forschungszentrums Jülich
Reihe Schlüsseltechnologien / Key Technologies

Band / Volume 158
Physics of Life
Lecture Notes of the 49th IFF Spring School 2018
26 February – 09 March 2018, Jülich, Germany
ed. by G. Gompper, J. Dhont, J. Elgeti, C. Fahlke, D. Fedosov,
S. Förster, P. Lettinga, A. Offenhäusser (2018), ca 1000 pp
ISBN: 978-3-95806-286-3

Band / Volume 159
Identifizierung von Bindungsdeterminanten von Tat-Vorläuferproteinen an den TatBCRezeptorkomplex während der Tat-abhängigen Proteintranslokation in *Escherichia coli*
A. Ulfig (2018), 186 pp
ISBN: 978-3-95806-290-0

Band / Volume 160
***Corynebacterium glutamicum* – a novel platform for the production of plant polyphenols**
N. Kallscheuer (2018), XIII, 98 pp
ISBN: 978-3-95806-291-7

Band / Volume 161
Neurons on 3D polymer nanostructures
A. Belu (2018), vii, 135 pp
ISBN: 978-3-95806-296-2

Band / Volume 162
Tailoring and Characterisation of Bioelectronic Interfaces
A. Markov (2018), 75 pp
ISBN: 978-3-95806-298-6

Band / Volume 163
Epitaxy of group IV Si-Ge-Sn alloys for advanced heterostructure light emitters
N. von den Driesch (2018), viii, 149 pp
ISBN: 978-3-95806-300-6

Weitere ***Schriften des Verlags im Forschungszentrum Jülich*** unter
http://wwwzb1.fz-juelich.de/verlagextern1/index.asp

Schlüsseltechnologien / Key Technologies
Band / Volume 163
ISBN 978-3-95806-300-6

Mitglied der Helmholtz-Gemeinschaft

JÜLICH
Forschungszentrum

Schlüsseltechnologien
Key Technologies

Epitaxy of Si-Ge-Sn for heterostructure emitters

163

Nils von den Driesch

JÜLICH
Forschungszentrum

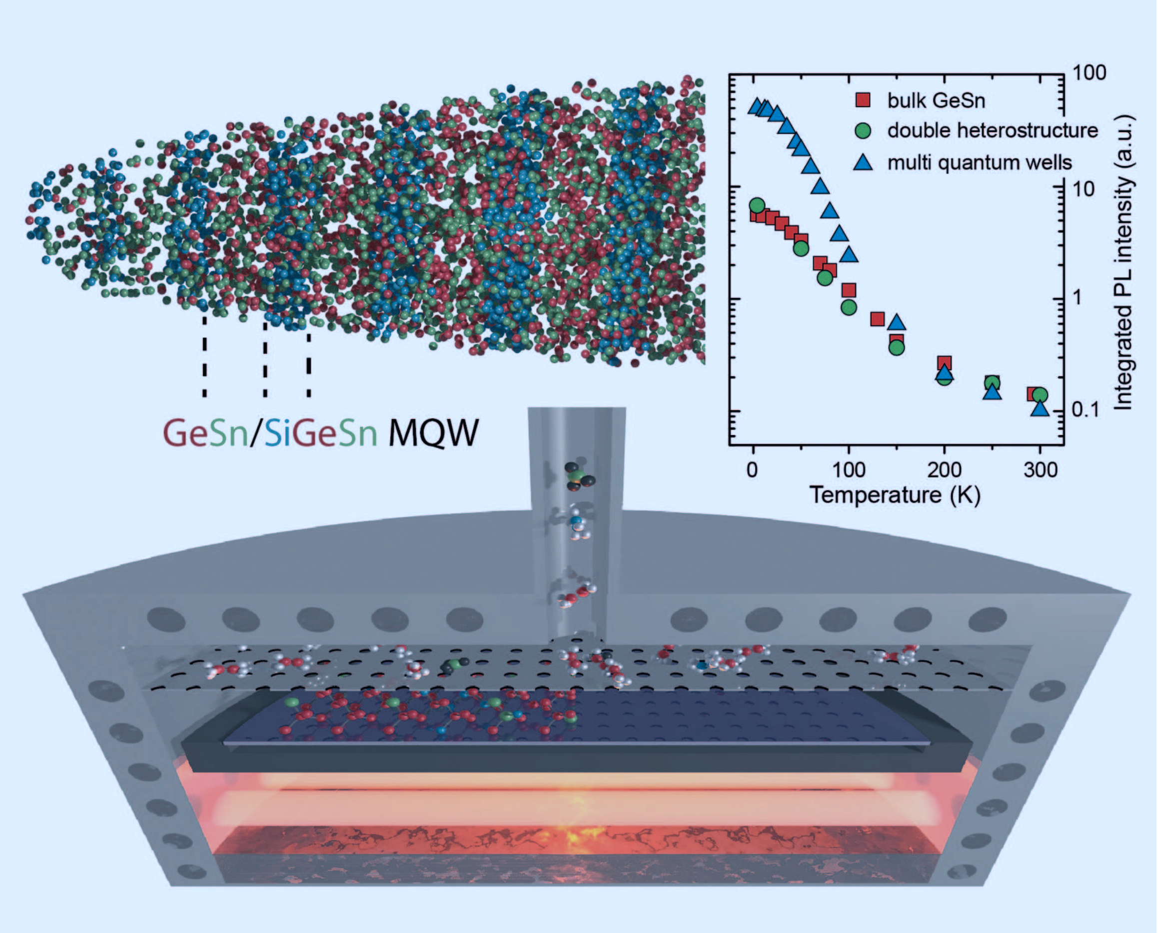

Epitaxy of group IV Si-Ge-Sn alloys for advanced heterostructure light emitters

Nils von den Driesch

Schlüsseltechnologien / Key Technologies
Band / Volume 163
ISBN 978-3-95806-300-6

Mitglied der Helmholtz-Gemeinschaft

JÜLICH
Forschungszentrum